Stellingen

behorende bij het proefschrift van Bas Bakker

1. Selectief gedeponeerd wolfraam is een interessante supergeleider voor supergeleidende devices, zowel vanuit het oogpunt van fabricage als vanwege de supergeleidende eigenschappen.

2. De fabricage van gecompliceerde sub-micron devices kan vereenvoudigd worden door het vervangen van elektronenlithografie door optische lithografie bij produktiestappen die een minder hoge resolutie behoeven.

3. In tegenstelling tot verwacht treedt "encroachment" ook op bij lage temperatuur W-CVD processen die gebruik maken van GeH_4.

   *C.A. van der Jeugd, G.J. Leusink, T.G.M. Oosterlaken, P.F.A. Alkemade, L.K. Nanver, E.J.G. Goudena, G.C.A.M. Janssen, and S. Radelaar, J. Electrochem. Soc. **139**, 3615 (1992).*

4. Elastische verstrooiing draagt bij tot de onderdrukking van "excess current" in supergeleidende juncties die gekoppeld zijn door een halfgeleidende verbinding.

5. Het gebruik van de inelastische verstrooiingstijd bepaald uit lokalisatie-experimenten als maat voor tijd van energierelaxatie in supergeleidende juncties is niet gerechtvaardigd. Het process van lokalisatie speelt zich af op een totaal andere energieschaal dan energierelaxatie in een supergeleidende junctie.

   *D.R. Heslinga, W.M. van Huffelen, T.M. Klapwijk, IEEE Trans. Magn. **Mag-27**, 3264 (1991).*

6. Wanneer een zweefvlieger op "final glide" erg laag zit en het zweet hem uitbreekt kan hij het raampje van de cockpit beter dicht laten.

7. In tegenstelling tot wat men zou verwachten gebeuren de meeste ongelukken met zweefvliegtuigen op de grond.

8. De conclusie dat de klant geen behoefte heeft aan een ruimere openstelling van winkels is waarschijnlijk gebaseerd op onderzoek dat overdag is gehouden.

9. De zogenoemde "Wet van Moore" betreffende het aantal componenten op een geïntegreerde schakeling is een self-fulfilling prophecy.

10. Het voorstel om de sleutel tot het decoderen van computergegevens verplicht te laten registreren bij de overheid, dit om toegang tot de versleutelde gegevens door justitie mogelijk te maken, is niet controleerbaar en werkt niet. Versleutelde gegevens zijn als zodanig niet te herkennen en het verplicht registreren van de sleutel maakt het breken van de code door onbevoegden eenvoudiger.

11. Afschaffing van fiscale aftrekbaarheid van rente op consumptief krediet levert een grotere bijdrage aan het milieu dan een carpool strook.

Delft, 14 oktober 1994

Planar Semiconductor Coupled

Superconducting Devices

PROEFSCHRIFT

ter verkrijging van de graad van doctor

aan de Technische Universiteit Delft,

op gezag van de Rector Magnificus Prof. ir. K.F. Wakker,

in het openbaar te verdedigen ten overstaan van een commissie,

door het College van Dekanen aangewezen,

op maandag 7 november 1994 te 16.00 uur

door

Sebastianus Johannes Maria BAKKER

natuurkundig ingenieur

geboren te Purmerend

Dit proefschrift is goedgekeurd door de promotoren:

Prof. dr. ir. S. Radelaar

Prof. dr. ir. T.M. Klapwijk

Table of Contents

CHAPTER I

INTRODUCTION

In the past decades the fabrication of small structures has made great progress[1]. Because of developments in electron beam lithography, reactive ion etching, and resist systems, dimensions far below 100 nm can be made nowadays. This is mainly due to the driving force of the semiconductor industry. This industry wants to get as many electronic basic elements as possible on one integrated circuit to make complicated functions possible and to improve speed. Research tools can reach dimensions more than one order of magnitude smaller than used in production. This process of reaching smaller and smaller dimensions has now reached a regime where new physical effects[2] are observed and exploited.

The proximity effect, the diffusion of Cooper pairs from a superconductor into an adjacent normal material, is well known in thin metal layers. At low temperatures this effect has a range of a few μm in well conducting metals to near a few tens of nm in heavily doped semiconductors. Since fabrication of devices with dimensions of 100 nm and smaller can be made, the proximity effect can be used to fabricate a Superconducting Field Effect Transistor; a SFET. Originally this research started as a co-operation with Dr. U. Kawabe of Hitachi Central Research Laboratory in Japan. He was interested in the use of advanced microfabrication tools to make a SFET. Inside a SFET two superconductors are coupled by the proximity effect, the strength of this coupling is influenced by the voltage on the a gate electrode. In this thesis we study different structures of this kind, all using silicon as semiconducting coupling. Two types are treated using different superconductors: $CoSi_2$ and amorphous tungsten. These superconductors are used because of the possibility of self-aligned deposition which simplifies the fabrication procedure. The purpose of this study is to gain insight in current transport in this kind of devices and in the possibilities of fabrication.

1 Coherence

Of particular importance in small structures are the elastic and inelastic scattering lengths. These are the mean distances an electron travels between corresponding scattering events. When one or more dimensions of the system are smaller than one of these lengths, the device operates in the mesoscopic regime. For instance the system dealt with in this thesis consists of semiconductor-coupled superconductors in the mesoscopic regime; the distance electrons travel between two superconductors is shorter than the inelastic and longer than the elastic scattering length. For a review see Klapwijk.[3]

Effects connected with these small dimensions can be divided into coherent and incoherent effects. Coherent effects are caused by quantum-interference processes and are mainly of importance at small voltages. Examples of coherent effects are the supercurrent, in which case the proximity effect connects the two superconductors, and reflectionless tunneling; i.e. quantum-coherent-enhanced Andreev scattering.

Incoherent effects are effects where the wave character of the electrons has to be not explicitly taken into account. They dominate at somewhat higher voltages. Now the system can be approximated by two independent sequential transmission processes through the two interfaces. The incoherent effects that can be described in this approach are multiple Andreev reflection and effects due to a non equilibrium energy distribution of the electrons in the normal part. Andreev reflection is a special kind of reflection that occurs at a normal-superconductor (NS) interface. In this process an electron coming from the normal side reflects as a hole, accompanied by the injection of a Cooper pair with charge 2e into the superconductor. Multiple Andreev reflections are visible as structure in the I-V curves. Other special features, caused by the non equilibrium distribution in the normal part that results from the energy dependent transmission and reflection coefficients of the NS interfaces, are also observed in the I-V measurements.

2 Device

In the work described in this thesis advanced microfabrication technology is used to realise semiconductor coupled superconducting devices in the mesoscopic regime with a controllable barrier. An independently variable barrier using a 2 dimensional electron gas gives direct control of a number of physical properties of the barrier. Through the carrier concentration,

controlled by the voltage on the gate, a number of physical properties can be modified like conductivity and Fermi level. This leads to a device with a FET structure, as proposed by Gray[4] and independently by Clark *et al.*.[5] This kind of structures has been made using III-IV semiconductors by Millea *et al.*[6], Ivanov *et al.*[7] and Takayanagi and Kawakami[8] and recently by Lenssen *et al.*.[9] In Si Superconducting FET (SFET) structures have been made by Nishino *et al.*[10,11]. In this thesis silicon is used as semiconductor, fabrication technology is very advanced for this semiconductor and future applications will be more easy to implement if based on silicon.

3 Possible applications

It has been claimed that the SFET has potential applications as switching element in logical integrated circuits. The ability to carry supercurrent in the on state promises shorter RC times, faster operation and lower power consumption. Another possibility would be to use SFET devices as interface elements between ordinary, Si based logic and Josephson junction circuits. These applications have still to be proven and are not expected in the near future. A reproducible fabrication process has still to be developed, the switching time of these devices has to be measured.

4 Scope of this thesis

In this thesis carrier transport in planar, semiconductor-coupled superconducting devices is studied. The design and fabrication of the devices will be presented in chapter II. In chapter III existing theory on superconductor-normal-superconductor (SNS) devices will be summarised and new extensions which include scattering and adapt the theory to the geometry of the device will be presented. Measurements and interpretations on devices without a gate using $CoSi_2$ as a superconductor will be presented in chapter IV and on devices with a gate using amorphous W as the superconductor in chapter V. In chapter VI we present results on the zero bias conductivity in amorphous W devices. In chapter VII localisation and superconductivity in ß-W are studied using magnetoresistance measurements. Chapter VI and VII are, in a slightly modified version, published in Physical Review B.[12, 13]

References

1 IBM J. Res. Devel. **32,** no. 4 (1988).

2 see for example C.W.J. Beenakker and H. van Houten, Solid State Physics, ed. H. Ehrenreich and D. Turnbull (Academic Press, New York, 1991) Vol. 44, p.1.

3 T.M. Klapwijk, Physica **B197,** 481 (1994).

4 K.E. Gray, Appl. Phys. Lett. **32,** 392 (1978).

5 T.D. Clark, R.J. Prance, and A.D.C. Grassie, J. Appl. Phys. **51,** 2736 (1980).

6 M.F. Millea, A.H. Silver, and L.D. Flesner, IEEE Trans. Magn. **MAG-15,** 435 (1979).

7 Z. Ivanov, T. Claeson, and T. Andersson, Proc. 18th Int. Conf. on low Temp. Phys., Kyoto,vol. 2, 1617 (1987).

8 H. Takayanagi and T. Kawakami, Phys. Rev. Lett. **54,** 2449 (1985).

9 K.-M.H. Lenssen, L.A. Westerling, C.J.P.M. Harmans, J.E. Mooij, M.R. Leys, W. van der Vleuten, and J.H. Wolters, to be published in Surf. Sci.

10 T. Nishino, M. Miyake, Y. Harada, U. Kawabe, IEEE Elec. Dev. Lett. **EDL-6,** 297 (1985).

11 T. Nishino, M. Hatano, H. Hasegawa, F. Murai, T. Kure, A. Hiraiwa, K. Yagi, and U. Kawabe, IEEE Elec. Dev. Lett. **10,** 61 (1989), M. Hatano, F. Murai, T. Nishino, H. Hasegawa, T. Kure, and U. Kawabe, J. Vac. Sci. Technol. **B7,** 1333 (1989).

12 S.J.M. Bakker, H.M. Jaeger, T.M. Klapwijk, E. van der Drift, and S. Radelaar, Phys. Rev. **B48,** 4168 (1993).

13 S.J.M. Bakker, E. van der Drift, T.M. Klapwijk, H.M. Jaeger, and S. Radelaar, Phys. Rev. **B49,** 13275 (1994).

CHAPTER II

DESIGN AND FABRICATION

1 Design

In this chapter we describe the fabrication of a device in which the barrier between two superconductors can be controlled by a gate electrode. The device is structured as an ordinary MOSFET with an exceptionally short distance between the source and drain electrodes with a gate electrode in between. Another special feature is that we use superconducting source and drain contacts. A schematic view of the device is shown in Fig. 2.1. Ordinary MOSFETs with the necessary short gate length are already known from the literature.[1] A Superconducting FET (SFET) device in Si has been made before by Nishino *et al.*.[2] In their device nano-scale insulation between the different electrodes has been obtained by using a polycrystalline silicon gate with oxidised sidewalls, configured with an overhanging gate that gives a shadow during evaporation of the superconductor. This overhanging gate insulates the gate from source and drain. This is a complicated structure to fabricate and requires many fabrication steps.

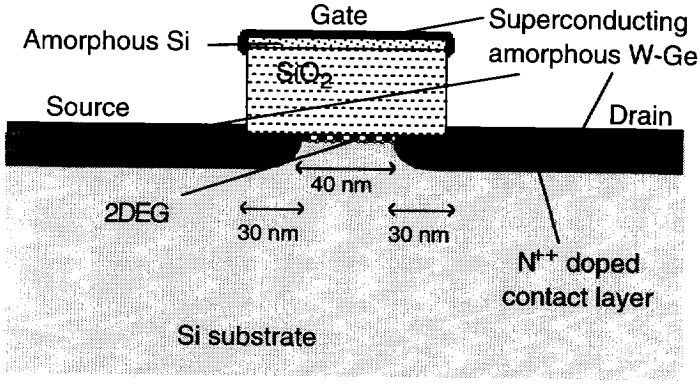

Fig. 2.1 Cross section of the device with gate and amorphous tungsten superconducting source and drain metallisation (schematic).

In our design we aimed at a fabrication process with a minimal number of fabrication steps. To study current transport between Si and superconductor also devices without a gate where fabricated.

1.1 Requirements and solutions

The requirement of supercurrent through the device and the integration in integrated circuit technology leads to the following demands on design and fabrication process.

Resolution and alignment

For a working SFET a very short gate length is needed. To observe a supercurrent the length has to be smaller than a few times the proximity length (the distance Cooper pairs diffuse into a normal material). As will be shown in chapter IV, the proximity length is expected to be on the order of 10 nm. This means a gate length on the order of or less than 100 nm to make the current path through non-superconducting material short enough. The resolution needed to fabricate a device with these dimensions makes e-beam lithography the obvious choice. In Fig. 2.1 dimensions of the device are shown. Obviously, fabrication of the gate, metallisation of source, drain, and gate, and implantation all require high resolution and mutual alignment. Alignment between different sub-100nm steps is very difficult, even using e-beam. So we employ a self-aligning process with only one high resolution lithography step needed. The deposition of the superconductor and the contact implantation are both self-aligning.

Possible superconductors

The choice of the superconductor is limited by the necessity of a self-aligned deposition process. The self-aligned Co silicidation process is one of the prime candidates. $CoSi_2$ has a T_c (superconducting transition temperature) of about 1.4 K. A second candidate is Chemical Vapour Deposition (CVD) of W. Ordinary α-W has a T_c of 15 mK, much too low for useful measurements. However, different process conditions, using GeH_4 for the reduction of WF_6 make the deposition of W-Ge films with an amorphous or ß-W structure possible. These films have a T_c of about 4 K and can be deposited selectively on Si, being essential for a self-aligned process. With commonly used superconductors as Nb and Al, self-aligned deposition is difficult to realise because it is only possible by directional evaporation using a gate with overhang[2]. This requires additional processing steps. Another silicide, V_3Si, promises a higher T_c (17 K), but fabrication is very difficult because the reaction between V and Si does not stop with V_3Si but proceeds to form silicides with a higher Si-concentration. The solution is to co-deposit V and Si in the right proportion, which makes a self-aligning process impossible.

In the remaining part of this paragraph we will mainly concentrate on the fabrication using amorphous tungsten, the fabrication using $CoSi_2$ will be treated in paragraph 2.3.2.

Contact

The contact between the superconductor and the semiconductor, in our case to the channel or 2-Dimensional Electron Gas or 2DEG, is of major importance. A high contact resistance means a low probability for Andreev reflection or Cooper pair transmission and suppresses the supercurrent through the device. A high contact resistance can be caused by contamination of the interface between the superconductor and the semiconductor and by a Schottky barrier. A solution to the contamination problem is the use of cleaning procedures including an HF-dip that passivates the surface and prevents oxidation. The contact resistance caused by the Schottky barrier can be minimised by using the right metallisation and a heavily doped contact layer. $CoSi_2$ and W deposition by CVD with GeH_4 are known for their low contact resistance.[3,4] To make this contact layer we use an implantation of As with low energy (10 keV) and a short anneal to suppress lateral transport of doping. The lateral doping must extend over a distance of a few tens of nm's under the gate (see Fig. 2.1) to contact the channel and to bridge the metal that creeps under the gate oxide. This consumption of Si at the Si-SiO_2 interface during metallisation is called encroachment (see paragraph 2.3.1.2) and can reach up to about 10 nm under the gate. The lateral doping may extend however not too far under the gate to prevent direct contact between source and drain. Final form of the device (Fig. 2.1):

The substrate is made of silicon, doped with boron (10-30 Ωcm). Source and drain metallisation are both made of superconducting material that contacts the 2DEG through the n^+ doped areas. This 2DEG is influenced by the voltage on the gate above, insulation is provided by a thin gate oxide (60 nm). Superconducting W is selectively deposited on the silicon; this process prevents contact between gate, source and drain without additional etching steps.

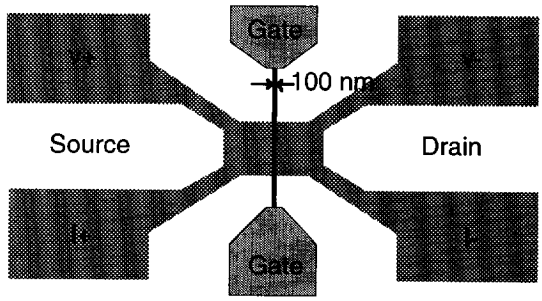

Fig. 2.2 Top view of the device (schematic).

In Fig 2.2 it is shown that the source and drain areas are contacted on two places to enable 4 point measurements. The gate can be contacted on both sides to make it possible to check whether the metallisation of the gate is continuous.

2 Process flow

2.1 Low resolution processing

The low resolution part of the process flow is schematically shown in Fig. 2.3. The field oxide is patterned twice, first to be used as a mask for marker fabrication, secondly to define source and drain areas. Thereafter a gate oxide is grown in the field oxide windows and a layer of Si is evaporated on top.

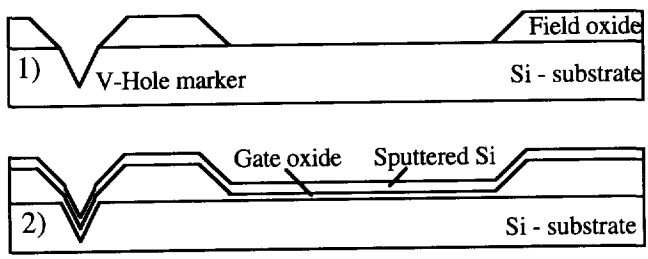

Fig. 2.3 Low resolution processing flowchart. 1) V-hole markers and patterning of the field oxide, 2) Gate oxide growth and Si deposition.

Markers

Markers are needed to align different patterns realised in separate process steps. The source and drain areas are made by optical lithography. The fabrication of the gate is done using high resolution e-beam lithography. The markers must be visible both optically and by e-beam. They must also be compatible with the fabrication steps following marker fabrication. We use V-hole markers, pyramid shaped holes in the silicon made by etching with KOH. KOH etches silicon anisotropically, providing pyramid-shaped holes in a (100) wafer. These markers can easily be seen by e-beam because they reflect electrons different compared to a flat surface. Furthermore they are compatible with all process steps afterwards, opposite to heavy metal markers.

The fabrication is done in the following way (detailed information about the recipes is available in the Appendix):

After the RCA clean (recipe WE4) a field oxide (recipe A3) is grown. Optical lithography is used to define the markers (recipe L1), followed by the HF etch (recipe WE5) to etch holes in

the oxide. After resist removal in acetone the oxide is used as a mask to etch the pyramid shaped holes in the Si by KOH (recipe WE6).

Source and drain definition

The source and drain areas and their contact windows are made in the field oxide. They are defined by optical lithography (recipe L1). This is followed by the HF etch (recipe WE5) which etches the SiO_2. (Fig. 2.3 step 1)

After the RCA clean (recipe WE4) the gate oxide is grown (recipe A2) in the windows and a silicon layer is evaporated on top. This silicon makes the self-aligned growth of the superconductor gate possible. (Fig. 2.3 step 2)

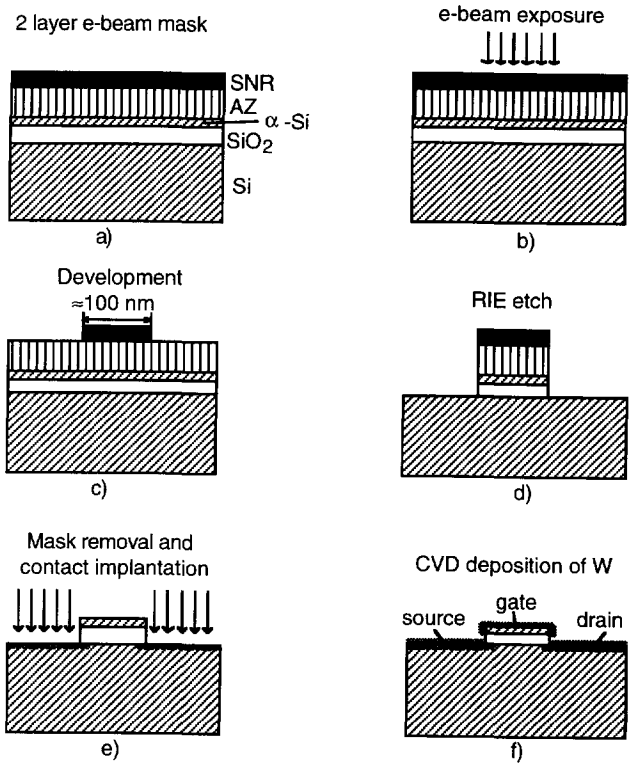

Fig. 2.4 Process flowchart of gate fabrication and metallisation.

2.2 Gate fabrication

Electron beam lithography (recipe L2) is used for the definition of the gate area and its contact pads. First a 2-layer resist system of AZ and SNR is spun on the wafer (Fig. 2.4a). The e-

beam sensitive negative resist SNR is the top layer of the 2-layer resist system. The pattern is written with a Philips EBPG/3 or a Leica EBPG/5 using automatic marker search for the alignment with the source and drain areas (Fig. 2.4b). The limiting factor in resolution is the use of the SNR resist. It has a practical resolution of about 100 nm. After development of the SNR (Fig. 2.4c) the bottom layer of AZ is anisotropically etched in a low pressure O_2 plasma (recipe DE5) using the silicon containing SNR as a mask. This gives vertical resist profiles, which improves the anisotropy of the oxide etching.

The gate pattern is transferred to the Si and SiO_2 layers by Reactive Ion Etching (RIE) (Fig. 2.4d). The Si is etched using a SF_6-O_2-He plasma[5] (recipe DE6) and the SiO_2 layer using a CHF_3 plasma (recipe DE1). The remaining resist is removed using fuming HNO_3 (recipe WE1).

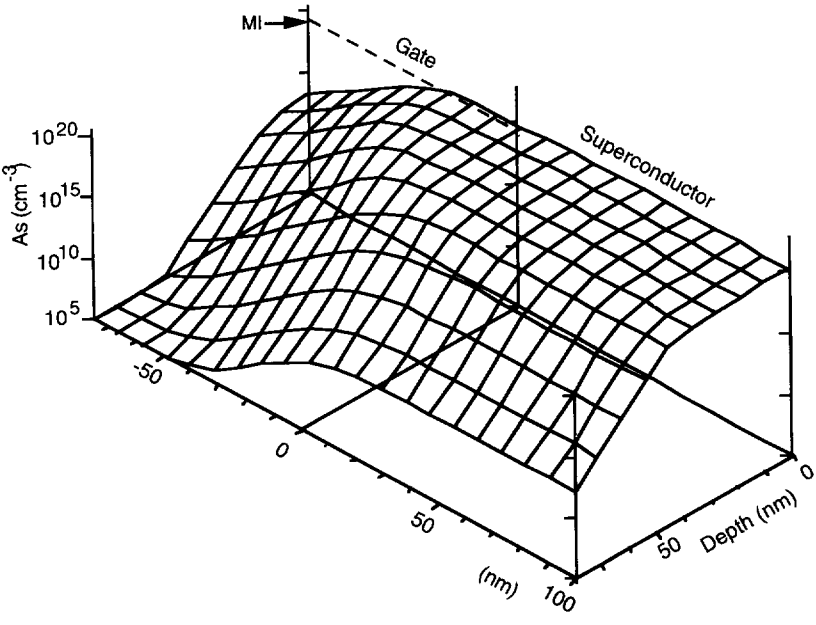

Fig 2.5 2D doping profile of the gate area. The right side is the implanted region underneath the W, left is underneath the gate. The dashed line gives the doping corresponding to the Metal-Insulator (MI) transition. Silicon doped below this level is insulating at low temperatures. A dose of 10^{15} cm^{-2} of As is implanted with 10keV.

To ensure good contact between the superconductor and the 2DEG the contact areas are implanted using the gate and field oxide as mask. (Fig. 2.4e) Because of the short gate length a very shallow implantation is needed. We used a 10 keV As implantation with a dose of $10^{15}cm^{-2}$. The anneal for activation of the doping and diffusion to reach the right lateral depth

is done in a Rapid Thermal Processor (as recipe A1, but 2 minutes at 975 °C). As shown in Fig. 2.5, the implantation profile[6] reaches a lateral distance under the gate of about 30 nm.

2.3 Metallisation

2.3.1 Self-aligned W-CVD

A 10 nm thick W film is deposited selectively on the source, drain and gate areas by chemical vapour deposition (CVD) (recipe D2,D3). It is a low temperature process based on the reduction of WF_6 with GeH_4 in an ASM Single Wafer Reactor. Details of the CVD process are reported by Van der Jeugd *et al.*[7] This is the first time W, self-aligned deposited using GeH_4, is used in a working device. A substrate temperature during growth of 275°C results in films with an amorphous W structure as demonstrated by X-ray diffraction. This temperature is chosen to suppress encroachment (see below). The resistivity of the deposited layers is on the order of 2 μΩm. A layer of silicon on top of the gate oxide promotes deposition on the gate. No metal is deposited on the insulating surfaces like the side walls of the gate oxide (Fig. 2.4f). In this process selectivity is only possible for thin layers. For thicker layers (> ≈10 nm) deposition on SiO_2 may occur as well.

2.3.1.1 Superconducting properties of amorphous W and ß-W

Table 2.1. Superconducting properties of different W-CVD films. The film of run 516 is amorphous, the others have the ß-W structure. The letter codes correspond to the samples mentioned in Chapter VII and in the figures.

Sample:	T_c:	H_{c2}:	$R_\square$:	RBS Ge content:	RBS Thickness:	RBS ρ:
	K	T	Ω	%	nm	μΩm
448, D	3.46±.02	7.45±.05	290±20	18%	6.46	2.18
448, F	3.43±.01	8.75±.05	290±20			
448, G	3.00±.05	9.60±.05	500±20			
455, E	2.84±.01		480±20	23%	4.72	2.78
475, I	2.83±.02	6.82±.05	135±20	16%	14.2	1.82
516, P	3.50±.05					
516, Q	3.91±.05					

Table 2.1 shows the superconductive properties measured on different samples. The thickness is designed to be 10 nm and the films are deposited selectively on silicon. The electrical properties are measured on strips of 10 μm wide and 1 mm long. Samples made in run 448, 455 and 475 consist of ß-W made by the GeH_4 W-CVD[7] (recipe D2). Samples made in run 516 are amorphous (recipe D3). Of the film deposited in run 448 and run 516 several samples are measured to get an estimate of the spread over the wafer. T_c and H_{c2} are defined as the

temperature and field where the normal resistance has been reduced by a factor of 2. H_{c2} is measured at 0.1 K with the magnetic field perpendicular to the film. The last three columns show results from RBS measurements. Fig. 2.6 gives the resistance vs. temperature. Fig. 2.7 gives the resistance vs. magnetic field. We also performed a critical field measurement with the magnetic field parallel to the film. For run 448 film F the result is: $H_{c2\|}>14.5$ T. Fig. 2.8 shows the critical current vs. temperature at zero magnetic field for sample F from run 448.

From the data of Table 2.1 can be concluded that the films are so thin that the properties are not well controlled. For our research application however they can be applied very well because our only demand is a film that becomes superconducting at a reasonable temperature and is selectively deposited. For the use in a production process the properties should be better controlled.

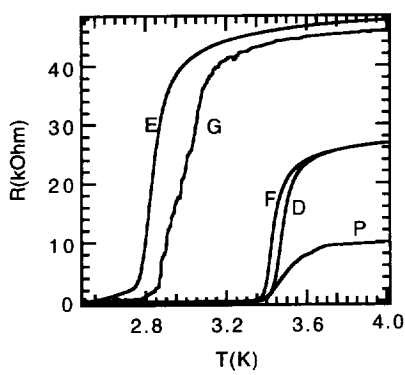

Fig. 2.6 Resistance vs. temperature near T_C for different W samples. Curve P is scaled to R_N=10kΩ because of a different sample geometry.

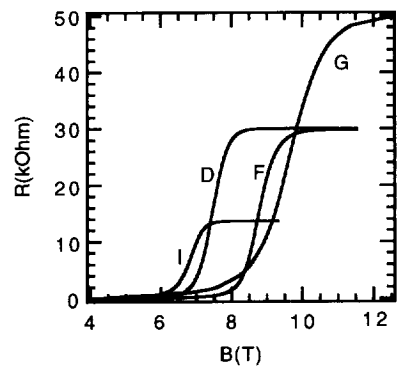

Fig. 2.7 Resistance vs. magnetic field for different ß-W samples.

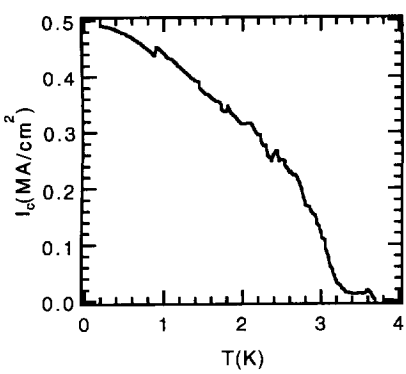

Fig. 2.8 Critical current vs. temperature for sample F of run 448.

2.3.1.2 Encroachment

High temperature W-CVD processes cause the problem of consumption of silicon by the growth of tungsten underneath the SiO_2 starting from the triple point between Si, W and SiO_2. This phenomenon is called encroachment. In extreme cases this can cause a short in the device. In the first runs we used a process for deposition of ß-W identical to that for amorphous W but at a temperature of 340°C (recipe D2). This gave, unexpectedly,[4] some encroachment (Fig. 2.9a) which bridged the contact implantation and brought the metal in direct contact with the 2DEG. I-V measurements (Fig. 2.10) show a gate voltage dependent breakthrough. A lower W deposition temperature (recipe D3) and an n^+ contact layer reaching further under the gate oxide, made by a longer anneal of 2 minutes instead of 30 seconds, eliminated that problem.

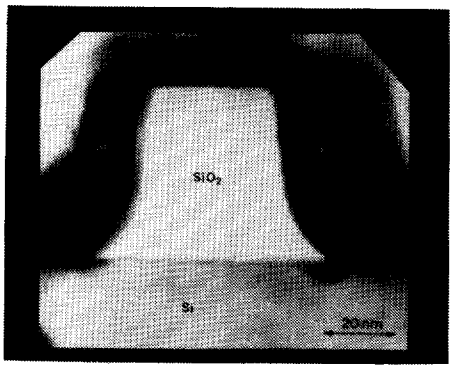

Fig. 2.9a TEM picture of the gate area showing encroachment.

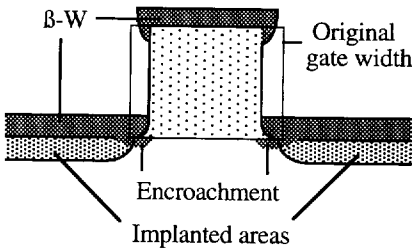

Fig. 2.9b Schematic view of the gate area showing encroachment.

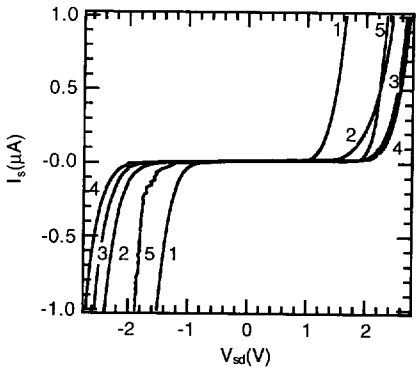

Fig. 2.10 Source current I_S vs. source-drain voltage V_{gs}, measured at different gate voltages: Curve 1 at V_g=-10 V, 2 at -4 V, 3 at 0 V, 4 at 4 V and 5 at 10 V.

2.3.2 Self-aligned $CoSi_2$ growth

Fabricating $CoSi_2$ in a self-aligned process is also not free of problems. Known problems in $CoSi_2$ formation are bridging (overgrowing oxide spacers) and compared to $TiSi_2$, a high sensitivity to surface cleanliness.[8] First we describe the general outline of the fabrication process, thereafter we continue with the problem of how to get a clean interface.

First the native oxide is removed in a 1% HF solution (recipe WE2) and then the substrate is immediately loaded into the vacuum system. After sputter deposition of 12 nm of cobalt (recipe D1) the $CoSi_2$ is selectively formed by a Rapid Thermal Anneal at 700°C for 30 s in Ar (recipe A1). As a result 45 nm of $CoSi_2$ is expected. The residual cobalt on the oxide is etched away selectively in a $HCl\text{-}H_2O_2$ (3:1) mixture (recipe WE3). This mixture also etches other cobalt silicides like CoSi and Co_2Si, which is important to suppress bridging.

The $CoSi_2$ forms because the Co reacts with the Si of the substrate. A layer of Si with the same thickness as the new $CoSi_2$ is consumed in the reaction. This is the basis of the self-alignment. Co only reacts with Si, not with SiO_2 and $CoSi_2$ is only formed on the exposed Si surfaces.

During $CoSi_2$ formation different atoms are moving. First Co reacts with Si to form Co_2Si in which case Co atoms are moving. Subsequently Co_2Si reacts with Si to form CoSi, in which process Si is the mobile species. The last step is reaction of CoSi to $CoSi_2$, in which Co is moving again.[9]

2.3.2.1 Interface

In the first experiments $CoSi_2$ was formed on an oxide pattern made by wet etching.[9] Here surface cleaning with HF only, turned out to be sufficient. We used RIE etching to pattern the oxide. Now $CoSi_2$ formation was not reliable, often no $CoSi_2$ was formed and no conductivity was measured. We suspected that this is caused by the RIE process. It is known[10] that the etching plasma contaminates the surface by carbon, fluorine and hydrogen. Carbon and fluorine will be implanted in the silicon to a depth of a few nm, hydrogen to about 10 nm. Cleaning of the surface might be a solution.

The following cleaning methods were compared:

1) HNO_3 to remove the resist followed by an HF-dip (recipe WE1, 2).

2) Like 1, but supplemented with Ar-sputtering before Co deposition (recipe DE2).

The films made following the first approach (1) do not conduct. No $CoSi_2$ is formed. AES analyses after the final wet etch with $HCl\text{-}H_2O_2$ show no sign of Co and a large amount of

oxygen down to about 60 nm (Fig. 2.11). AES analyses done before this etch show a layer of oxygen between the substrate and the Co containing top layer (Fig. 2.12). The ratio between the Co and Si signal makes it likely that the top layer mainly consists of Co_2Si. Co_2Si is one of the intermediate stages of the $CoSi_2$ formation and can be etched by $HCl\text{-}H_2O_2$.

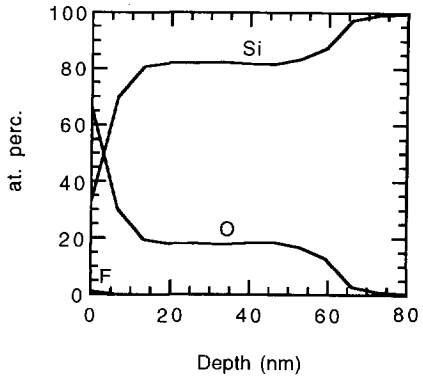

Fig. 2.11 Atomic concentration vs. depth measured by ESCA on a film made by method 1 after $HCl\text{-}H_2O_2$ etch.

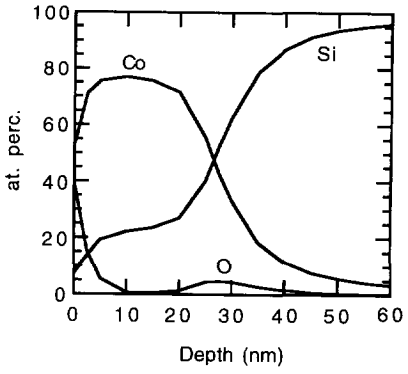

Fig. 2.12 AES profile of film made by method 1 before $HCl\text{-}H_2O_2$ etch. Note the oxygen containing layer near the Co-Si interface.

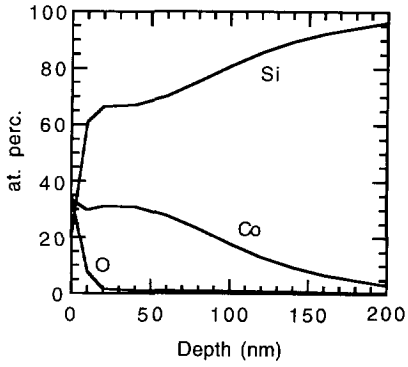

Fig. 2.13 AES profile of sample made by method 2. Note the 1:2 ratio of Co and Si.

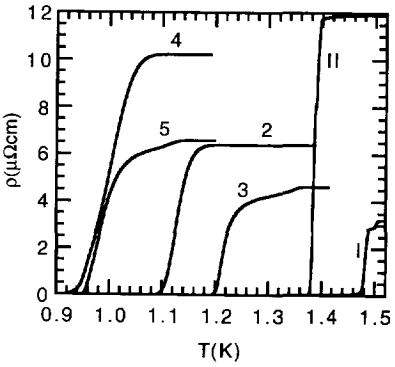

Fig. 2.14 Resistivity of different $CoSi_2$ samples as function of temperature near T_c. Samples 2-5 use as cleaning Ar sputtering, 3-5 with additional cleaning steps. In sample I and II the last 10-15 nm of oxide is etched by HF, sample I is made on low doped silicon, II on heavily B doped silicon.

Knowing that $CoSi_2$ formation proceeds in three steps, the Co_2Si present on top of an oxygen containing layer can be explained assuming that the contamination of the surface causes a

kinetic diffusion barrier for Co. If this is the case the reaction is too slow and there is no time available for all three reaction steps to take place.

Films made by method 2 do show $CoSi_2$ and no oxygen between the substrate and the $CoSi_2$ film (Fig. 2.13).

Resistance measurements (Fig 2.14) show a spread in resistivity, which might be due to remaining surface contamination. Sample 2 is made by cleaning method 2, samples 3-5 are made using different additional cleaning steps including RCA clean and application of an O_2 plasma. The resistivity varies from 5.5 μΩcm to 12 μΩcm. Resistance measurements show that T_c is not the same for all films (Fig. 2.14). Some films lack a clear transition and show a plateau in the middle of the transition. The question remains whether these effects are just a spread between different samples or that it is related to the cleaning method, the measurements have only been done on one sample for each cleaning method. An indication in favour of remaining surface contamination is curve I, this is measured on a sample where the last 10-15 nm is etched by HF instead of by RIE. This sample has a high T_c and a low resistivity.

In conclusion, Ar sputtering is sufficient to remove the diffusion barrier resulting from RIE etching in order to fabricate $CoSi_2$ reliably. The diffusion barrier consists probably of oxygen.

2.3.2.2 Sample fabrication

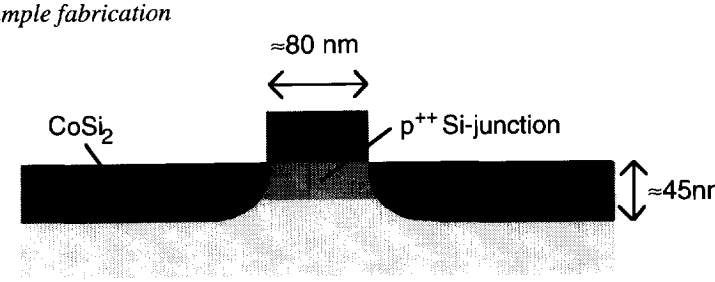

Fig. 2.15 Cross section of the device with $CoSi_2$ used as superconductor (schematic).

Devices used for the measurements described in Chapter IV (Fig 2.15) are fabricated in the following way. To get a well-defined current path the current is restricted to the top 20 nm of the Si. This is done by growing a thin layer of heavily B doped Si on a low doped wafer by MBE (Molecular Beam Epitaxy). On top of the Si a 60 nm thick oxide is deposited by LPCVD (Low Pressure Chemical Vapour Deposition), which is used as a mask for $CoSi_2$ formation. The pattern is transferred to this layer by e-beam lithography (recipe L2) after which it is etched by a RIE process using CHF_3 (recipe DE1). To get a clean surface for $CoSi_2$ formation, (see above) the oxide is not etched completely with RIE, the last 10-15 nm is etched in an HF

solution (recipe WE2) after resist removal (recipe WE1). $CoSi_2$ is formed as described above, the resistivity near T_c is shown in Fig. 2.14 curve II. To restrict the current path also in the lateral direction trenches are etched by argon sputtering.

References

1 S.Y. Shou, D.A. Antoniadis, H.I. Smith, IEEE Elec. Dev. Lett. **EDL-6,** 665 (1985).

2 T. Nishino, M. Hatano, H. Hasegawa, F. Murai, T. Kure, A. Hiraiwa, K. Yagi, and U. Kawabe, IEEE Elec. Dev. Lett. **10,** 61 (1989), M. Hatano, F. Murai, T. Nishino, H. Hasegawa, T. Kure, and U. Kawabe, J. Vac. Sci. Technol. **B7,** 1333 (1989).

3 L. van den Hove, R. Wolters, K. Maex, R. De Keersmaecker, and G. Declerck, J. Vac. Sci. Technol. **B 4**, 1358 (1986).

4 C.A. van der Jeugd, G.J. Leusink, T.G.M. Oosterlaken, P.F.A. Alkemade, L.K. Nanver, E.J.G. Goudena, G.C.A.M. Janssen, and S. Radelaar, J. Electrochem. Soc. **139,** 3615 (1992).

5 A. Manenschijn, G.C.A.M. Janssen, E. van der Drift, and S. Radelaar, J. Appl. Phys. **65**, 3226 (1989).

6 The 2 dimensional doping profile of the contact implantation is calculated with TMA-TSUPREM-4 Two-Dimensional Process Analysis Program.

7 C.A. van der Jeugd, G.J. Leusink, G.C.A.M. Janssen, and S. Radelaar, Appl. Phys. Lett. **57**, 354 (1990).

8 R.D.J. Verhaar, A.A. Bos, J.M.F.G. van Laarhoven, H. Kraaij, and R.A.M. Wolters, Appl. Surf. Sci. **38,** 458 (1989).

9 L. van den Hove, Phd thesis, K.U. Leuven (1988).

10 A.J. van Roosmalen, J.A.G. Baggerman, S.J.H. Brader, Dry Etching for VLSI. Plenum Press New York (1991).

CHAPTER III

CONCEPTUAL FRAMEWORK

1 Introduction

In electrical measurements on superconductor-normal metal-superconductor (SNS) structures we find a non-linear conductance at low voltages, already far below the superconducting energy gap. This is caused by a number of effects that can be divided into two categories: coherent and incoherent effects. Coherent effects are due to the quantum mechanical nature of the carriers. The other category, incoherent effects, are effects in which the observations can be accounted for by using a classical energy distribution description in the spirit of the Boltzmann equation. In this chapter we will focus on incoherent effects of superconductors in contact with normal materials. The coherent effects will be treated in chapter IV and VI. In chapter IV supercurrent is treated. In chapter VI reflection-less tunneling will be presented, another coherent effect, i.e. quantum interference enhanced Andreev reflection.

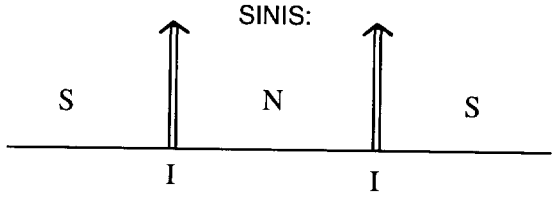

Fig. 3.1 Schematic diagram showing the model geometry used by OTBK to describe SNS structures. S stands for superconductor, N for normal material and I for interface barrier.

Incoherent effects are usually treated in a way initiated by Klapwijk *et al.*.[1] Transmission is treated in a full quantum mechanical way at the NS interface and an energy distribution description is used in the normal region. The SNS approach is refined by the introduction of an elastic scattering barrier at the interfaces (I), this leads to a SINIS model (Fig. 3.1). The current in this structure is calculated by Octavio and co-workers,[2] hereafter indicated as the OTBK model. Strictly speaking, the model is one-dimensional and based on the assumption that

carriers in the normal region maintain the same energy and can change direction and nature only at the interfaces. An interesting effect that can be explained by the OTBK model is subharmonic gap structure. This is structure on the differential resistance curve occurring at integer fractions of twice the superconducting gap. The OTBK model explains this by multiple Andreev reflections.[3] Andreev reflection is the reflection of an electron incident from the normal conductor into a hole, which retraces the path of the incident electron. This is required by the pair-correlation in the superconductor and results into an extra Cooper pair in the superconductor. A full quantum mechanical description of subharmonic gap structure is given by Arnold[4] for SIS structures, here qualitatively the same result is found.

In our devices with gate, which will be extensively discussed in chapter V and VI, no subharmonic gap structure is observed. Therefore, the theoretical study in this chapter is mainly focused on mechanisms that might suppress the subharmonic gap structure using the framework of the OTBK model. In doing so we first start with a short review of existing theory. To this aim we introduce in paragraph 2 the physical processes at the single Normal metal - Superconductor (NS) interfaces and Andreev reflection. In paragraph 3 the OTBK model for SINIS systems will be described.

In our devices the barrier between the superconducting electrodes consists of a semiconductor in which scattering can not be neglected. This scattering might cause the suppression of subharmonic gap structure. For that reason we present in paragraph 4 extensions of the OTBK model that includes scattering in the normal region. The elastic mean free path is much shorter than the length of our device. In paragraph 4.1 we consider the implications of elastic scattering in the normal region. The influence of elastic scattering on subharmonic gap structure and other aspects are studied. Inelastic scattering may be another cause for the suppression of subharmonic gap structure and will be studied in paragraph 4.2.

In the higher dimensional case elastic scattering is fundamentally different from the one-dimensional case because at each scattering event the angle of incidence at the interface changes. Because the transmission and reflection coefficients depend on the angle of incidence at the interface, the influence of elastic scattering on the transport properties of the device is different for the higher dimensional case. In paragraph 5 we calculate the effect of the angle-dependent transmission and reflection coefficients. We then integrate these coefficients over the angle to simulate the case of strong elastic scattering, assuming that the direction of motion of the electrons is completely random.

Andreev reflection, an important mechanism for subharmonic gap structure, is fully suppressed by high interface barriers. For this limit of interfaces with low transparency we will summarise the low transparency model from Heslinga *et al.*[5] in paragraph 6.

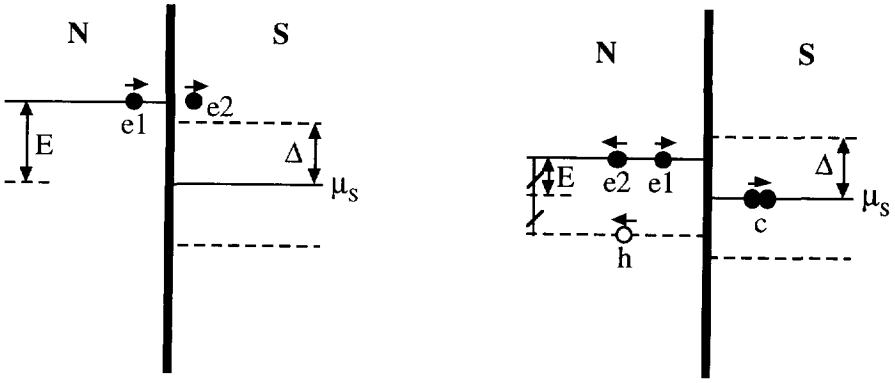

Fig. 3.2 Schematic diagram showing processes at the NS interface. Transmission through the interface is shown in the left figure, this is only possible for electrons with energy |E|>Δ relative to the electrochemical potential of the superconductor μ_s. The right-hand side shows ordinary reflection and Andreev reflection. Electron e1 with energy E can undergo ordinary reflection that results in electron e2 or Andreev reflection, this results in a reflected hole h with energy -E and a Cooper pair in the superconductor.

2 The NS interface

To understand the NS interface we assume, as in Klapwijk *et al.*,[1] an abrupt rise of the superconducting gap at the interface. The elastic scattering at the interface is represented by a delta function potential. Electrons from the normal side (Fig. 3.2) can either reflect at the interface, undergo Andreev reflection or pass the interface and proceed as a quasi-particle in the superconductor. Andreev reflection[3] is the process in which an electron with energy E incident from the normal side of the NS interface is reflected as a hole with energy -E while injecting a Cooper pair into the superconductor. The mirror process is possible for a hole incident on the NS interface. Both processes contribute a charge of 2e to the current, together with ordinary transmission that contributes a charge e. Using the Bogoliubov equations[6] and by matching the wave functions at the NS interface, one finds an energy-dependent transmission coefficient T(E), reflection coefficient B(E), and Andreev reflection coefficient A(E) of the NS interface. These coefficients depend on Z, a dimensionless parameter that gives the strength of the potential barrier V(x) at the interface, i.e. $V(x)=Z\hbar v_F\delta(x)$ with v_F the Fermi velocity and $\delta(x)$ a

delta function. The coefficients are given in table 3.1. The current through the contact is given by:

$$I=\frac{1}{eR_0}\int_{-\infty}^{\infty}[f_0(E-eV)-f_0(E)][2A(E)+T(E)]dE \qquad (3.1a)$$

with the Sharvin resistance $R_0=[2\mathcal{A}v_F e^2N(0)]^{-1}$ and $f_0(E)$ the Fermi distribution. Here $\mathcal{A}$ is the cross-sectional area of the contact and N(0) the density of states at the Fermi energy. The normal state resistance of an NS contact with a barrier of strength Z can be calculated by taking $\Delta=0$:

$$R_n=R_0(1+Z^2) \qquad (3.1b)$$

The charge transport of 2e by each incident electron in case of Andreev reflection leads to an excess current I_{exc} above the current carried in the normal state. This excess current is defined as the positive intercept with the current axis when the I-V curves are extrapolated from voltages above twice the superconducting gap to zero voltage. An analytical integration[7] of the coefficients of table 3.1 leads to:

$$\frac{eR_nI_{exc}}{\Delta}=\frac{1}{2Z^2}\left[1-\frac{1}{2Z(1+2Z^2)\sqrt{1+Z^2}}\operatorname{arctanh}\left(\frac{2Z\sqrt{1+Z^2}}{1+2Z^2}\right)\right] \qquad (3.2)$$

The calculated value using this equation is identical to the numerically result obtained by Klapwijk *et al.*.[1]

Table. 3.1 Andreev reflection coefficient A, ordinary reflection coefficient B and transmission coefficient T for electrons incident on the NS interface as a function of energy relative to the Fermi level. Here are used: $u_0^2=1-v_0^2=\frac{1}{2}\{1+\sqrt{(E^2-\Delta^2)/E^2}\}$ and $\gamma^2=[u_0^2+Z^2(u_0^2-v_0^2)]^2$. $N_S(E)=(u_0^2-v_0^2)^{-1}$ is the superconducting density of states is, Δ is the superconducting gap.

	A	B	T
$\lvert E\rvert<\Delta$	$\frac{\Delta^2}{E^2+(\Delta^2-E^2)(1+2Z^2)^2}$	1-A	0
$\lvert E\rvert>\Delta$	$\frac{u_0^2v_0^2}{\gamma^2}$	$\frac{(u_0^2-v_0^2)^2Z^2(1+Z^2)}{\gamma^2}$	$\frac{(u_0^2-v_0^2)(Z^2+u_0^2)}{\gamma^2}$

3 OTBK

The OTBK model[1,2] uses results obtained from quantum mechanical calculations for the NS interface as presented in table 3.1. The reflection and transmission coefficients are used to calculate the energy distribution in the normal region between the two superconductors. From this distribution function the current is calculated (Fig. 3.3).

The distribution function is divided into two parts: a distribution function of electrons that go to the right $f_{->}(E,x)$ and a distribution function of electrons that go to the left $f_{<-}(E,x)$, these distributions are coupled at the interfaces. The distribution of electrons that start at the left interface and go to the right, $f_{->}(E,0)$, is the sum of the contributions of the Andreev reflected holes, $A(E)[1-f_{<-}(-E,0)]$, the electrons that undergo ordinary reflection, $B(E)f_{<-}(E,0)$, and transmitted electrons, $T(E)f_0(E)$. $f_0(E)$ is the Fermi distribution, the superconducting density of states is incorporated in the transmission coefficient.

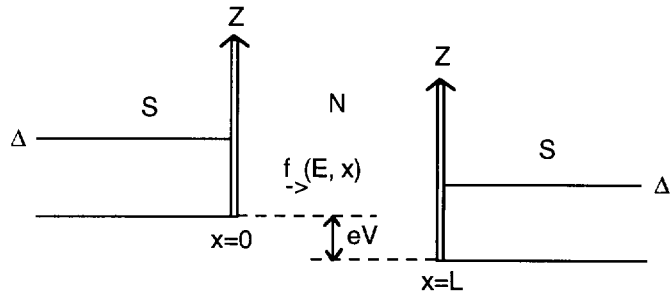

Fig. 3.3 Schematic diagram of the weak link model used in the OTBK model.

The distribution of electrons that start at the right interface and go to the left, $f_{<-}(E,L)$, consists of the same contributions. In equation form:[1,2]

$$f_{->}(E,0)=A(E)[1-f_{<-}(-E,0)]+B(E)f_{<-}(E,0)+T(E)f_0(E) \qquad (3.3)$$

$$f_{<-}(E,L)=A(E)[1-f_{->}(-E,L)]+B(E)f_{->}(E,L)+T(E)f_0(E) \qquad (3.4)$$

In the model it is assumed that the electrons that start at one interface reach the other with an unchanged energy distribution, except that the energy distribution is now shifted an amount eV relative to the electrochemical potential of the other superconductor:

$$f_{->}(E,L)=f_{->}(E-eV,0) \tag{3.5a}$$

$$f_{<-}(E,0)=f_{<-}(E+eV,L) \tag{3.5b}$$

Flensberg *et al.*[8] showed that, provided the barriers and the superconductors are identical, the symmetry in the problem can simplify the solution. Since the reflection and transmission coefficients are all even in energy, the electrons with distribution $f_{->}(E,0)$ which move to the right will have the same distribution as the holes of energy -E moving in the opposite direction with distribution $1-f_{<-}(-E,L)$ which gives:

$$f_{->}(E,0)=1-f_{<-}(-E,L) \tag{3.6}$$

Now we can eliminate one subpopulation by substituting Eq. 3.5 and 3.6 in Eq. 3.3 and obtain the result ($f_{->}(E)$ replaces $f_{->}(E,0)$ at x=0):

$$f_{->}(E)=A(E)f_{->}(E-eV)+B(E)[1-f_{->}(-E-eV)]+T(E)f_0(E) \tag{3.7}$$

Except for the Z=0 case this equation has to be solved self-consistently by numerical methods. The current through the junction is:

$$I=\frac{1}{eR_0}\int_{-\infty}^{\infty}dE[f_{->}(E)-f_{<-}(E)]=\frac{1}{eR_0}\int_{-\infty}^{\infty}dE[f_{->}(E)+f_{->}(-E-eV)-1]$$

$$=\frac{1}{eR_0}\left(\int_{-\infty}^{\infty}dE[2f_{->}(E)-1]+eV\right) \tag{3.8}$$

The normal resistance of the junction R_n can be calculated analytically:

$$R_n=R_0(1+2Z^2). \tag{3.9}$$

Important features of the electron transport explained by this model are subharmonic gap structure and excess and deficit current. Excess and deficit current can be detected by extrapolating the high voltage part ($eV>>2\Delta$) of the I-V curves to V=0 (Fig. 3.4a). Just as in the single NS case, excess current (positive intercept) is explained by the extra conductance resulting from Andreev reflections in the energy interval Δ around the Fermi energy of the

superconductor. On the other hand, the Andreev reflection probability decreases rapidly with increasing barrier strength Z and this leads to a current deficit (negative intercept) for higher Z values. In this case the conductance in the energy interval Δ around the Fermi energy of the superconductor is smaller than in the normal case. In a certain energy range the normal region has almost no "communication" with one superconductor and thus contributes less to the current.

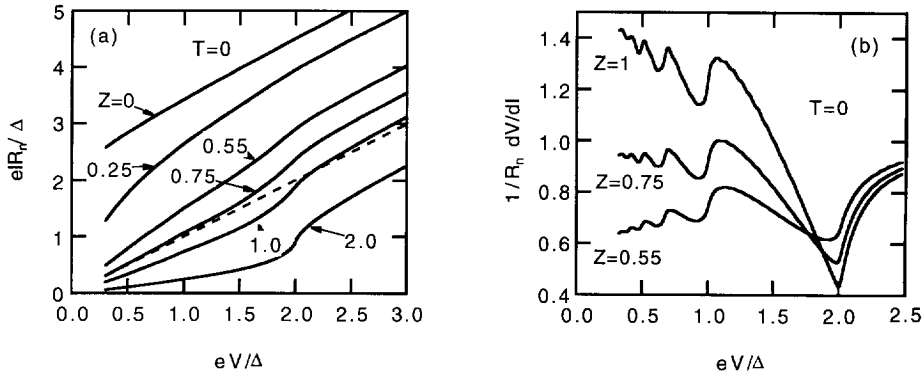

Fig. 3.4 Calculations that have been done using the OTBK model for different values of the barrier height Z and at T=0. a) Normalised I-V characteristics showing change from excess current to a current deficit as Z is increased. The dashed line corresponds to $V=R_nI$. b) Normalised differential resistance curves showing subharmonic gap structure. (See also ref. 8)

Subharmonic gap structure is structure in the differential resistance curves at integer fractions of twice the superconducting gap. Calculated results are shown in Fig. 3.4b. This structure originates from multiple Andreev reflections. When the applied voltage exceeds $2\Delta/ne$, the number of possible Andreev reflections changes with one, which shows up in the conductivity.

4 Scattering in the OTBK model

Underlying assumptions in the OTBK model are conservation of energy and of direction of motion of the carriers in the normal region. Only at the interfaces direction can change in this one-dimensional model. Although the devices studied by Van Huffelen *et al.*[9] are in the diffusive regime, the model has been successful in interpreting carrier transport phenomena in these semiconductor coupled structures. The authors studied a sandwich structure geometry of heavily doped silicon of 50 nm thick covered by niobium on both sides. The elastic mean free path in heavily doped silicon is about 5 nm, which means that only a small fraction reaches the other side without scattering. Since we expect elastic scattering to be even stronger in our case

we extend the OTBK with elastic scattering and study its effect on subharmonic gap structure in paragraph 4.1.

Suppression of higher order subharmonic gap structure is often attributed to inelastic scattering (Van Huffelen *et al.*[9] and Nitta *et al.*[10]). However, the number of electrons that undergo inelastic scattering is small, an inelastic scattering length a few times larger than the length of the device is not unusual. In devices where this is the case (see Van Huffelen *et al.*[9]) we still see suppression of higher order subharmonic gap structure. This can be understood by taking into account that subharmonic gap structure originates from multiple Andreev reflections, the electrons have to cross the normal area more than once and so have a higher probability of inelastic scattering. This causes the higher order structure to be more strongly suppressed. Nitta *et al.*[10] modelled inelastic scattering in the Z=0 case based on the OTBK model. Here we introduce inelastic scattering in the OTBK model in a similar way, but for general Z. This theory is treated in paragraph 4.2.

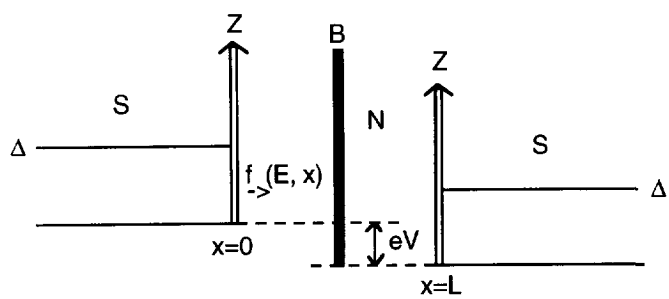

Fig. 3.5 Schematic diagram of the weak link model used in the extension on the OTBK model to include scattering. B is the barrier where the scattering takes place.

In both extensions of the OTBK model we assume scattering to take place at a barrier placed at the centre of the normal area. This is schematically shown in Fig 3.5. For elastic scattering in one dimension this is a good approximation if we do not include quantum mechanical effects. The only scattering possible in one dimension is a change of direction. For inelastic scattering the equilibrium energy distribution is very important. As can be seen in paragraph 4.2, we will assume that a fraction of the electrons scatter at the barrier B to the Fermi distribution. This is a gross simplification but perhaps the best possible in the framework of the OTBK model.

4.1 Elastic scattering

Elastic scattering is modelled by assuming that all scattering is confined to one barrier in the centre of the normal area (Fig 3.5). Quantum coherent effects are neglected. A fraction of the

electrons changes direction, depending on the height of the barrier. Not all electrons that start at one interface will reach the other so Eq. 3.5 is replaced by:

$$f_{->}(E,L)=Pf_{->}(E-eV,0)+(1-P)f_{<-}(E,L) \tag{3.10a}$$

$$f_{<-}(E,0)=Pf_{<-}(E+eV,L)+(1-P)f_{->}(E,0) \tag{3.10b}$$

with P the transmission probability of the barrier for electrons. This is the only difference with the original model. Using this assumption with the original equations 3.3, 3.4 and 3.6 we can eliminate one sub-population and calculate the other; the distribution of electrons leaving the interface at x=0:

$$f_{->}(E)=A(E)[Pf_{->}(E-eV)-(1-P)f_{->}(-E)]+B(E)[(1-P)f_{->}(E)-Pf_{->}(-E-eV)]+ T(E)f_0(E)+A(E)(1-P)+B(E)P \tag{3.11}$$

The current is:

$$I=\frac{1}{eR_0}\int_{-\infty}^{\infty}dE[f_{->}(E)-f_{<-}(E)]=\frac{P}{eR_0}\int_{-\infty}^{\infty}dE[f_{->}(E)+f_{->}(-E-eV)-1]$$

$$=\frac{P}{eR_0}\left(\int_{-\infty}^{\infty}dE[2f_{->}(E)-1]+eV\right) \tag{3.12}$$

Also in this case we can calculate the normal resistance:

$$R_n=\frac{1+2PZ^2}{P}R_0. \tag{3.13}$$

We calculated numerically the differential resistance curves using this model to see what the influence of elastic scattering is on the subharmonic gap structure. Fig. 3.6 shows the results for different P and Z values, scaled with the resistance in the normal state. The P=1 curves (no scattering) are identical to the original OTBK curves.

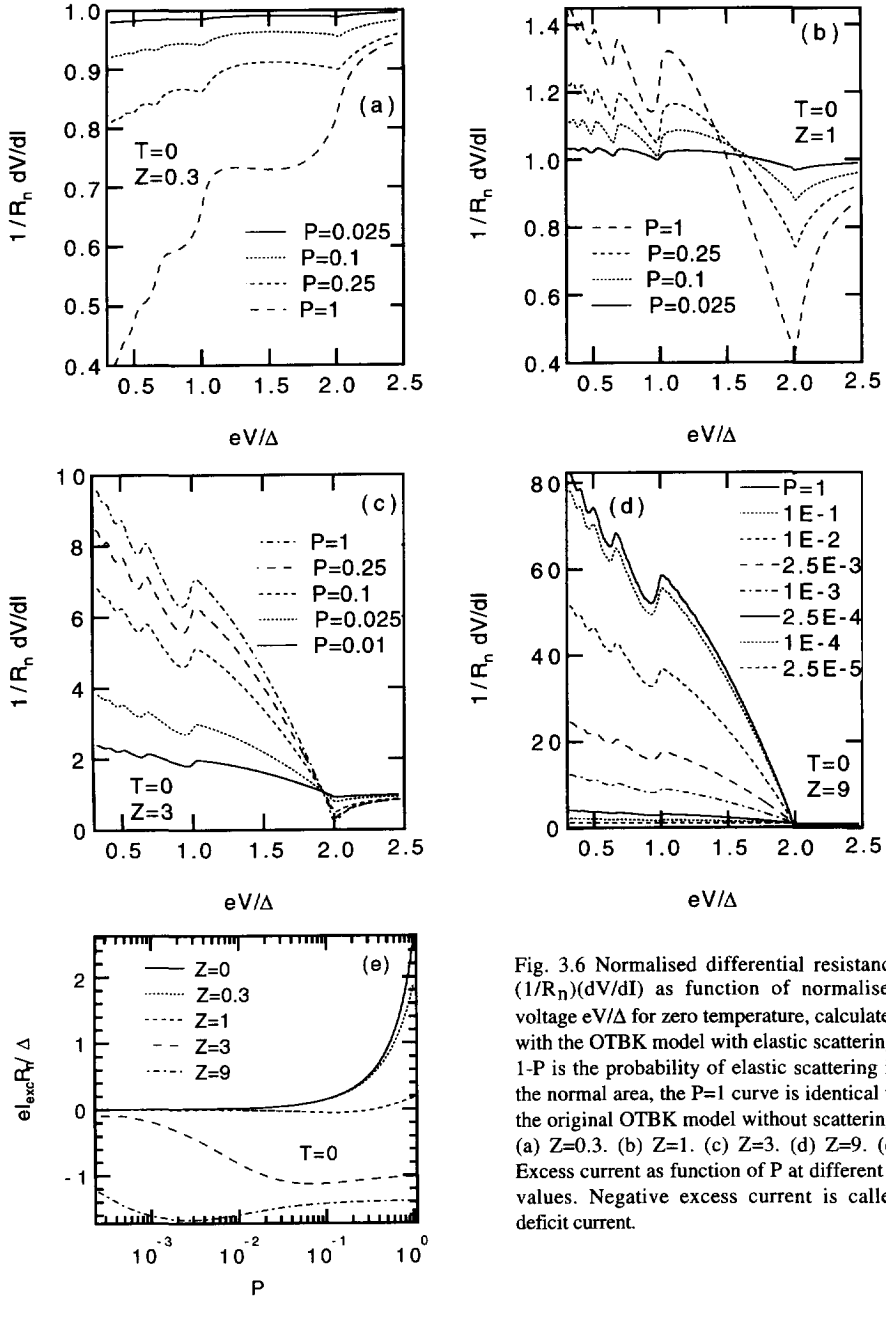

Fig. 3.6 Normalised differential resistance $(1/R_n)(dV/dI)$ as function of normalised voltage eV/Δ for zero temperature, calculated with the OTBK model with elastic scattering. 1-P is the probability of elastic scattering in the normal area, the P=1 curve is identical to the original OTBK model without scattering. (a) Z=0.3. (b) Z=1. (c) Z=3. (d) Z=9. (e) Excess current as function of P at different Z values. Negative excess current is called deficit current.

4.1.1 Influence on subharmonic gap structure

The main effect of the elastic scattering is the reduction of the amplitude of the structure on the differential resistance curves. When the curves are scaled it can be seen that the reduction is the strongest for the 2Δ dip (if $Z>1$). For $Z<1$ the structure at 2Δ is not reduced more strongly than the other structure. This is opposite to what can be naively expected because the structure at higher n originates from multiply Andreev-reflected particles that have to pass the scattering barrier more than once, as described by Arnold.[4]

This result can be understood if we think of the barrier in the normal region as if it has a certain width. As seen from inside the barrier Andreev reflection probability and transmission probability are changed because multiple reflections between the barrier and the NS interface are possible before the electron transmits or enters the barrier again as an electron or hole caused by Andreev reflection. We define the total Andreev reflection probability A' as the probability that the reflected hole comes back into the barrier.

The total Andreev reflection probability A' and transmission probability T' have the following value: $A'=\frac{AP}{(1-(1-P)B)^2-(1-P)^2A^2}$, $T'=\frac{T}{1-(A+B)(1-P)}$ with A, B and T from table 3.1. For small P this becomes $A'=0.5$ and $T'=0$ for $|E|<\Delta$ and $A'=0$ and $T'=1$ for higher energies, independent of Z.

The Andreev reflection "transmits" the structure in the total transmission around energy Δ, to the energies $2\Delta/n$. Although the structure is much weaker when P is small, the transmission is better; an Andreev reflection coefficient of 0.5 is higher than the Andreev reflection coefficient of an NS interface at $Z>1$.

4.1.2 Influence on excess and deficit current

Fig. 3.6e shows that the excess current is also reduced or even turns over to a deficit current when elastic scattering is introduced. The behaviour of the current deficit depends on barrier height. Excess current can be seen as a reduced interface resistance caused by Andreev reflection. Elastic scattering manifests itself as a series resistance, the relative contribution of the reduced interface resistance becomes smaller with higher amounts of elastic scattering.

The same argument can be used to explain the behaviour of the current deficit. Here it is useful to think in terms of a series resistance that depends on electron energy. Current deficit is then explained by a higher interface resistance in an energy interval 2Δ. Elastic scattering causes a series resistance at all energies, which reduces the relative importance of the higher interface

resistance in the energy interval 2Δ. The higher interface resistance in the energy interval 2Δ causing the current deficit rises with Z so an increasing amount of elastic scattering is needed to reach a comparable series resistance.

The initial increase in current deficit with increasing elastic scattering can be explained by the extra conductance caused by a high density of states near Δ. This conductance partly compensates the current deficit caused by a higher interface resistance. In case of elastic scattering there is an extra elastic scattering resistance in series, which causes (for high Z values) the initial increase in current deficit until it decreases again.

The influence of elastic scattering on the normal resistance (Eq. 3.13) can help solving another problem with the application of the OTBK model to devices with semiconductor barriers (Ref. 9). If we derive a barrier strength Z by comparing the differential resistance curves and use Eq. 3.9 to calculate the normal resistance, the calculated value is orders of magnitude smaller than the measured normal resistance. This can be explained by assuming that a fraction of the surface is transparent, which is supposed to be caused by the uneven distribution of doping atoms. However, this explanation is not consistent with Schottky barrier theory. Schottky barrier theory does give a reasonable estimation for the normal resistance while also there the distribution of doping atoms should be of major influence. The incorporation of elastic scattering gives the same amount of subharmonic gap structure for a higher Z value. This higher Z value together with the resistance contribution of the elastic scattering will give a much higher normal resistance.

We conclude that elastic scattering does not reduce subharmonic gap structure, the relative amplitude remains the same. Only the 2Δ structure is more strongly reduced. Elastic scattering does give extra normal resistance and suppresses excess current. The current deficit can be enlarged for intermediate amounts of elastic scattering and high interface barriers, but a higher amount of elastic scattering suppresses it in the end.

4.2 Inelastic scattering

Inelastic scattering is modelled in a similar way as elastic scattering: by assuming that all scattering is concentrated in one barrier in the centre of the normal area. A variable fraction of the electrons relaxes to the equilibrium distribution.

The problem here is that we have to make an approximation for the equilibrium energy distribution. For the case without scattering or only elastic scattering this was not necessary. All injected electrons kept the same energy until they reached one of the interfaces. In the case of one central barrier a chemical potential at the average level of the two superconducting banks

is a natural choice. For the equilibrium distribution we take the Fermi distribution. This is a reasonable approximation at higher temperatures and low probability of inelastic scattering, outside this region the model is not applicable. At low temperatures the Fermi distribution is very sharp. It is not to be expected that in reality, at low probability of inelastic scattering, the scattered electrons are fully relaxed and a broad distribution is expected. At high probability of inelastic scattering multiple inelastic scattering events can occur. This, together with a voltage drop across the normal region, causes different equilibrium distributions at different interfaces. In this case the assumption of an averaged chemical potential is clearly not justified. The limit of high interface barriers and including inelastic scattering is treated in paragraph 6.

At the barrier in the centre of the normal region a fraction P_e of the electrons scatters elastically, a fraction P_i scatters inelastically and a fraction P_t transmits through the barrier. The sum $P_t+P_e+P_i$ equals one. The distribution reaching an interface is the sum of the distribution of transmitted electrons coming from the other side $P_t f_{->}(E-eV,0)$, the distribution of electrons that have undergone elastic scattering and come from the same side $P_e f_{<-}(E,L)$ and the distribution of electrons that have relaxed to the Fermi distribution $P_i f_0(E-eV/2)$. Eq. 3.6 is then replaced by:

$$f_{->}(E,L)=P_t f_{->}(E-eV,0)+P_e f_{<-}(E,L)+P_i f_0(E-eV/2) \qquad (3.14a)$$

$$f_{<-}(E,0)=P_t f_{<-}(E+eV,L)+P_e f_{->}(E,0)+P_i f_0(E+eV/2) \qquad (3.14b)$$

Together with the original equations 3.3, 3.4 and 3.6 we can eliminate one sub-population and calculate the other. The distribution of electrons leaving the interface at x=0 is then given by:

$$\begin{aligned} f_{->}(E)=&A(E)(P_t f_{->}(E-eV)-P_e f_{->}(-E))+B(E)(P_e f_{->}(E)-P_t f_{->}(-E-eV))+\\ &T(E)f_0(E)+A(E)(1-P_t-P_i f_0(-E+eV/2))+B(E)(P_t+P_i f_0(E+eV/2)) \end{aligned} \qquad (3.15)$$

The current is:

$$I=\frac{1}{eR_o}\int_{-\infty}^{\infty} dE[f_{->}(E)-f_{<-}(E)]=\frac{2-2P_e-P_i}{2eR_o}\left(\int_{-\infty}^{\infty} dE[2f_{->}(E)-1]+eV\right) \qquad (3.16)$$

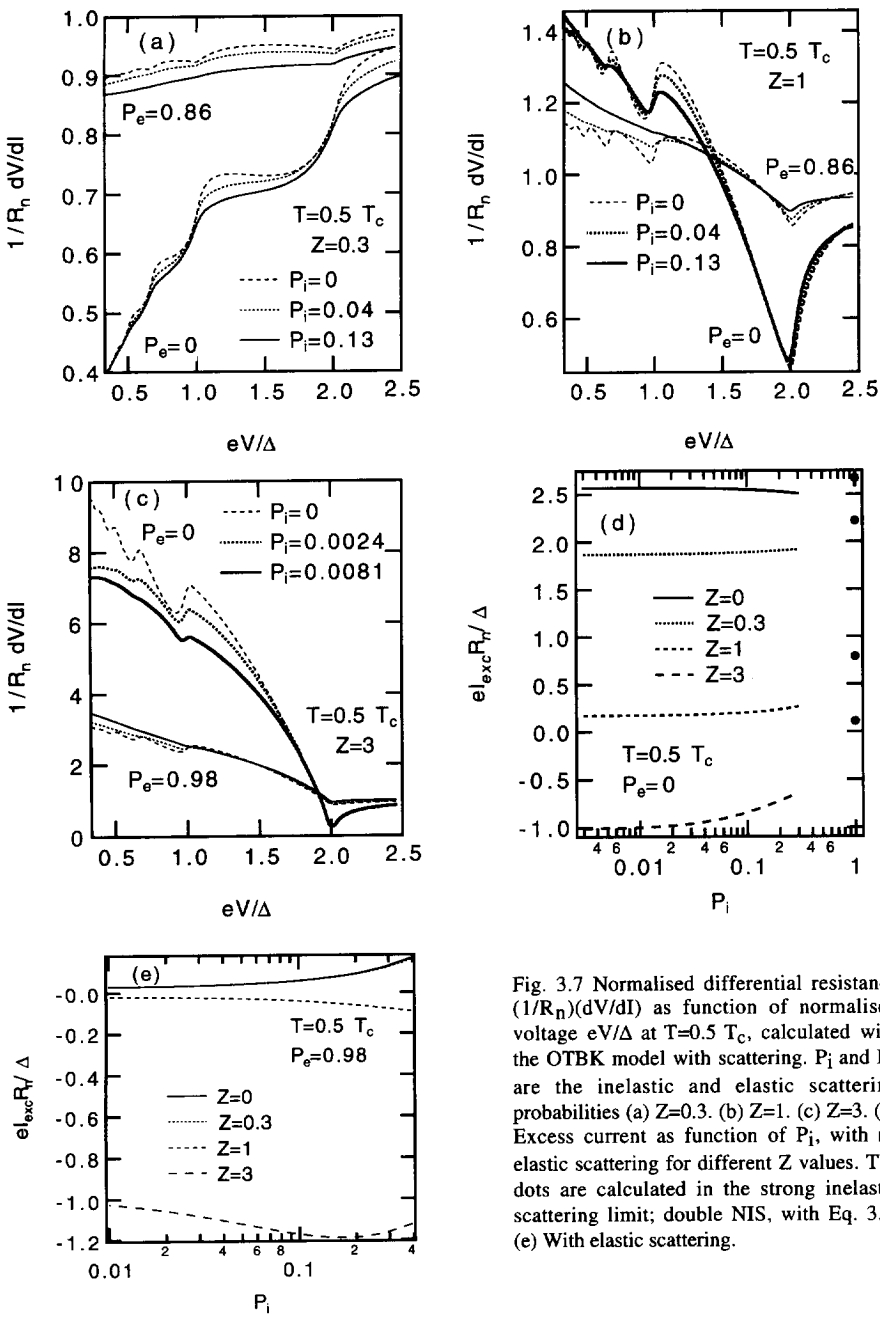

Fig. 3.7 Normalised differential resistance $(1/R_n)(dV/dI)$ as function of normalised voltage eV/Δ at $T=0.5\ T_c$, calculated with the OTBK model with scattering. P_i and P_e are the inelastic and elastic scattering probabilities (a) Z=0.3. (b) Z=1. (c) Z=3. (d) Excess current as function of P_i, with no elastic scattering for different Z values. The dots are calculated in the strong inelastic scattering limit; double NIS, with Eq. 3.2. (e) With elastic scattering.

which in the normal state becomes:

$$I_n=\frac{(2-2P_e-P_i)V}{2(1+(2-2P_e-P_i)Z^2)R_o} \qquad (3.17a)$$

or a resistance of:

$$R_n=(\frac{2}{2-2P_e-P_i}+2Z^2)R_o \qquad (3.17b)$$

Examples of the resulting differential resistance curves are shown in Fig. 3.7. For Z=0 we get the same results as provided by the analytic method of Nitta *et al.*.[10] We observe that inelastic scattering suppresses higher order subharmonic gap structure. With higher interface barriers Z less inelastic scattering is needed to suppress higher order subharmonic gap structure. In the low barrier case of Z=0.3 we observe that in the presence of elastic scattering a smaller amount of inelastic scattering is sufficient to suppress higher order subharmonic gap structure. The influence on excess and deficit current is small at these small amounts of inelastic scattering.

5 2-Dimensionality

In the higher dimensional case the result of scattering is fundamentally different from the one-dimensional case because the transmission and reflection coefficients depend on the angle of incidence on the interface. This angle changes at each scattering event. To see if in more than one dimension the resulting I-V curves are much different from the one-dimensional case, we calculate the scattering coefficients as a function of the angle of incidence. Then we compute the average over this angle, to model the case of strong elastic scattering in two dimensions, after which we compare the resulting transmission and scattering coefficients with the one-dimensional case.

First we have to calculate the transmission and scattering coefficients as a function of angle. We follow the same technique as in Ref. 1. The Bogoliubov wave functions are matched at the interface, using the extra coordinate φ, the angle to the normal on the NS interface. We assume refraction of the wave functions at the interface. The results are given in table 3.2.

Table. 3.2 Andreev reflection coefficient A_{2D}, ordinary reflection coefficient B_{2D} and transmission coefficient T_{2D} for electrons incident on the NS interface as a function of E, energy relative to the Fermi level and φ, angle to the normal on the NS interface. Here are used: $u_0^2=1-v_0^2=\frac{1}{2}\{1+\sqrt{(E^2-\Delta^2)/E^2}\}$ and $\gamma' = u_0^2\cos^2\varphi+Z^2(u_0^2-v_0^2)$.

	A_{2D}	B_{2D}	T_{2D}
$\lvert E\rvert<\Delta$	$\frac{\Delta^2\cos^4\varphi}{E^2\cos^4\varphi+(2Z^2+\cos^2\varphi)^2(\Delta^2-E^2)}$	1-A	0
$\lvert E\rvert>\Delta$	$\frac{u_0^2v_0^2\cos^4\varphi}{\gamma'^2}$	$\frac{Z^2(Z^2+\cos^2\varphi)(u_0^2-v_0^2)^2}{\gamma'^2}$	$\frac{(u_0^2-v_0^2)\cos^2\varphi(u_0^2\cos^2\varphi+Z^2)}{\gamma'^2}$

We integrate[7] over angle of incidence to model the case of strong elastic scattering in 2 dimensions. The results are:

For E>Δ:

$$A'_{2D}=\frac{2}{\pi}\int_0^{\pi/2}A_{2D}d\varphi=\frac{v_0^2}{2u_0^2}\left(2-\frac{Z\sqrt{u_0^2-v_0^2}(3u_0^2+2Z^2(u_0^2-v_0^2))}{(u_0^2+Z^2(u_0^2-v_0^2))^{3/2}}\right) \tag{3.18a}$$

$$B'_{2D}=\frac{2}{\pi}\int_0^{\pi/2}B_{2D}d\varphi=\frac{Z}{2}\sqrt{u_0^2-v_0^2}\,\frac{u_0^2+(1+2Z^2)(u_0^2-v_0^2)}{(u_0^2+Z^2(u_0^2-v_0^2))^{3/2}} \tag{3.18b}$$

$$T'_{2D}=\frac{2}{\pi}\int_0^{\pi/2}T_{2D}d\varphi=\frac{\sqrt{u_0^2-v_0^2}}{u_0^2}\left(\sqrt{u_0^2-v_0^2}+\frac{Z(u_0^2(2-3u_0^2)-Z^2(u_0^2-v_0^2)^2)}{(u_0^2+Z^2(u_0^2-v_0^2))^{3/2}}\right) \tag{3.18c}$$

for E<Δ:

$$A'_{2D}=\frac{2}{\pi}\int_0^{\pi/2}A_{2D}d\varphi=1-Z\sqrt{\frac{\sqrt{\Delta^2-E^2}}{\sqrt{1+(1+2Z^2)^2(\Delta^2-E^2)}+(1+2Z^2)\sqrt{\Delta^2-E^2}}}\,X$$

$$(1+\frac{2(1+Z^2)\sqrt{\Delta^2-E^2}}{\sqrt{1+(1+2Z^2)^2(\Delta^2-E^2)}}) \tag{3.19a}$$

$$B'=1-A' \tag{3.19b}$$

$$T'=0 \tag{3.19c}$$

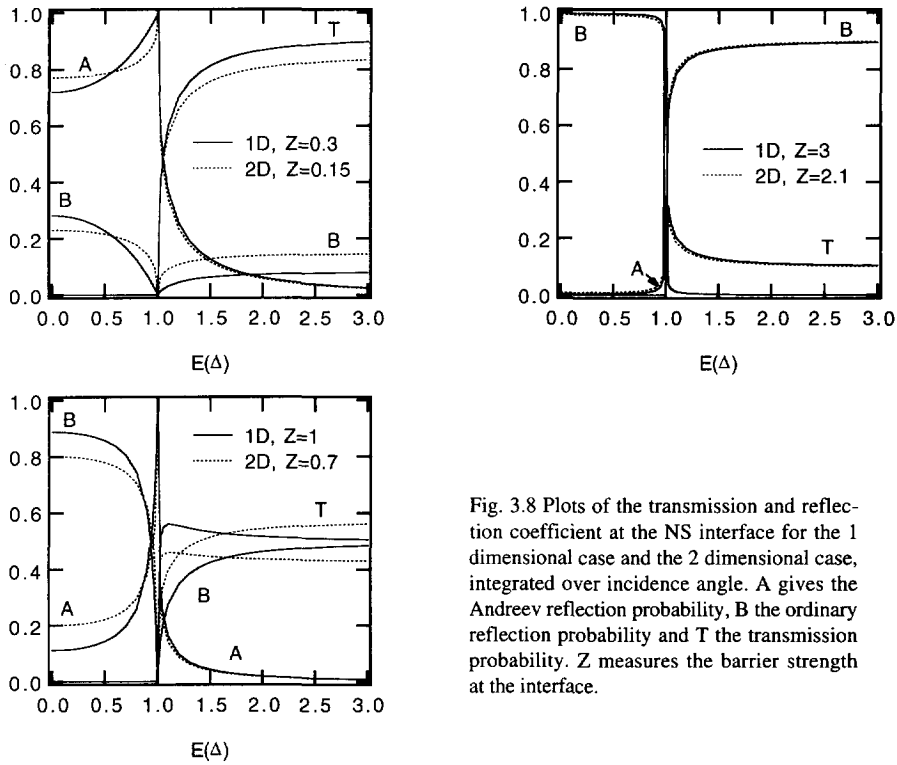

Fig. 3.8 Plots of the transmission and reflection coefficient at the NS interface for the 1 dimensional case and the 2 dimensional case, integrated over incidence angle. A gives the Andreev reflection probability, B the ordinary reflection probability and T the transmission probability. Z measures the barrier strength at the interface.

The resulting transmission and reflection coefficients are qualitatively the same as in the 1-dimensional case. It can easily be seen that for Z=0 the coefficients are identical to the coefficients in the 1-D case, for non-zero Z values the 1D and 2D cases are both shown in Fig. 3.8. Here the Z value in the 1-D case is changed slightly from the 2D value such that the curve is closest to the 2-D one.

We conclude that extending the calculations to two dimensions does not give a fundamental change in electrical behaviour, the changes caused by this extra dimension are comparable to a slightly different Z value in the one dimensional case.

6 Low transparency limit

The low transparency limit as described in the SINIS model by Heslinga *et al.*,[5] treats the case of high interface barriers and neglects Andreev reflection. It models the normal area as a reservoir of carriers that is in communication with the superconducting electrodes by tunneling through the interface, which causes a nonequilibrium energy distribution. This energy distribution relaxes to the Fermi distribution by inelastic scattering. Central in this model is the injection rate that is defined as:

$$\Gamma=\frac{1}{N_n e^2 R_c d} \tag{3.20}$$

Γ is the injection rate of electrons from the superconductor into the normal region and depends on d, the width of the normal area, N_n the density of states in the normal part and R_c, the contact resistance. The injection rate gives a rate for electrons entering and leaving the reservoir where relaxation occurs. Together with the relaxation rate τ_E it gives the degree of nonequilibrium. The degree of nonequilibrium rises with increasing $\Gamma\tau_E$, the electrical behaviour depends on the degree of nonequilibrium.

6.1 Injection and relaxation

The energy distribution in the normal region is determined by population from one superconducting electrode, extraction from the other and by relaxation. The population rate r_p at a certain energy level is the tunneling current at that level divided by the electronic charge:

$$r_p=\frac{\mathcal{A}}{e^2 R_c} N_s(E-eV/2)\,[f_0(E-eV/2) - f_n(E)] \tag{3.21}$$

where $\mathcal{A}$ is the surface area of the device, R_c the specific contact resistance in the normal state, $N_s(E)$ the reduced density of states of the superconductor, $f_0(E)$ the Fermi distribution, and $f_n(E)$ the energy distribution function of the normal region. The extraction rate from the normal region to the other electrode:

$$r_e=\frac{\mathcal{A}}{e^2R_c}N_s(E+eV/2)\,[f_n(E)-f_0(E+eV/2)] \tag{3.22}$$

The relaxation rate is written as:

$$r_r=\mathcal{A}N_n d\frac{f_n(E)-f_0(E)}{\tau_E} \tag{3.23}$$

The steady state occupation at energy E is determined by the balance $r_p=r_e+r_r$. This gives:

$$N_s(E-\frac{eV}{2})[f_0(E-\frac{eV}{2})-f_n(E)]=N_s(E+\frac{eV}{2})[f_n(E)-f_0(E+\frac{eV}{2})]+\frac{f_n(E)-f_0(E)}{\Gamma\tau_E} \tag{3.24}$$

using Γ as defined above. With this distribution function we calculate the current using the tunnel equation:

$$I=\frac{\mathcal{A}}{eR_c}\int_{-\infty}^{\infty}N_s(E-eV/2)\,[f_0(E-eV/2)-f_n(E)]dE \tag{3.25}$$

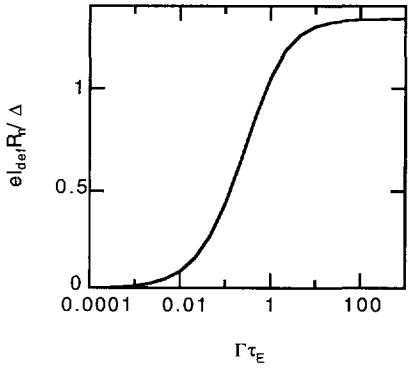

Fig. 3.9 Normalised current deficit as function of $\Gamma\tau_E$ for $T<<T_c$.

In Fig. 3.9 the current deficit is shown calculated with this model as function of $\Gamma\tau_E$. A high degree of nonequilibrium ($\Gamma\tau_E<<1$) suppresses the current deficit. The temperature dependence of the current deficit is nearly the same as that of the superconducting gap.[5]

In the next two chapters we will compare the models presented in this chapter with the observed strength of the subharmonic gap structure and the amount of excess or deficit current.

References

1 T.M. Klapwijk, G.E. Blonder, and M. Tinkham, Physica **109-110B+C,** 1657 (1982), G.E. Blonder, M. Tinkham, and T.M. Klapwijk, Phys. Rev. **B 25,** 4515 (1982).

2 M. Octavio, M. Tinkham, G.E. Blonder, and T.M. Klapwijk, Phys. Rev. **B 27,** 6739 (1983).

3 A.F. Andreev, Sov. Phys. JETP **19,** 1228 (1964).

4 G.B. Arnold, J. Low Temp. Phys. **68,** 1 (1987).

5 D.R. Heslinga, W.M. van Huffelen, T.M. Klapwijk, IEEE Trans. Magn. **Mag-27,** 3264 (1991).

6 P.G. DeGennes, Superconductivity of Metals and Alloys (Benjamin, New York, 1966), Chap. 5.

7 Result obtained with the help of MAPLE V, University of Waterloo, Canada

8 K. Flensberg, J.B. Hansen, and M. Octavio, Phys. Rev. **B 38,** 8707 (1988).

9 W.M. van Huffelen, T.M. Klapwijk, D.R. Heslinga, M.J. de Boer and N. van der Post, Phys. Rev. **B 47**, 5170 (1993).

10 J. Nitta, H. Nakano, T. Akazaki, and H. Takayanagi, Single-Electron Tunneling and Mesoscopic Devices, Proc. 4th Int. Conf. SQUID '91 (Berlin). Spinger-Verlag Berlin Heidelberg (1992) p.303.

CHAPTER IV

SNS DEVICES USING $CoSi_2$ AS SUPERCONDUCTOR

In this chapter we present results on planar devices consisting of two $CoSi_2$ superconducting electrodes coupled by a heavily doped silicon link. In these devices a supercurrent is observed as well as structure in current voltage curves at integer fractions of the energy gap resulting from multiple Andreev reflection (subharmonic gap structure). In planar devices similar results have only been obtained by Nitta *et al.*[1] in a InAs heterostructure. In a non-planar device also by Van Huffelen *et al.*[2] observed supercurrent and subharmonic gap structure using a thin crystalline membrane sandwiched between superconducting niobium electrodes.

We have used $CoSi_2$ because it can be deposited self-aligning and because it is known[3] to have a well-defined interface and a low interface resistance to Si. $CoSi_2$ is superconducting below 1.4 K. Using e-beam lithography and dry etching the distance between the superconducting electrodes can be made as small as 80 nm. Most measurements have been done below 1K in a ^{3}He-^{4}He dilution cryostat. The conductance is measured with a standard 4-point lock-in technique. The system is well shielded from external noise.

In paragraph 1 we briefly summarise the theory on supercurrents in SNS devices with interface resistance between the superconductor (S) and the normal (N), degenerately doped silicon in the middle. In paragraph 2.1 we describe measurements in the voltage carrying state and interpret them using the model of multiple Andreev reflection extended with contributions from elastic and inelastic scattering as described in chapter III. In paragraph 2.2 we will describe the measured supercurrent and interpret it using the theory of paragraph 1.

1 Supercurrent theory

The supercurrent through a SNS device depends on the interface barrier and on the length Cooper pairs diffuse into the normal material, i.e. the proximity length or normal metal coherence length. Van Huffelen *et al.*[2] found that the theory of Kupriyanov and Lukichev[4] is

well suited for the description of supercurrent in a SNS device with degenerate silicon as normal region. Near T_c and without interface barrier, this theory gives results identical to the model presented by Likharev[5] that does not include an interface barrier. The theory of Kupriyanov and Lukichev[4] allows a variable barrier strength. The supercurrent is calculated in the theory of Kupriyanov and Lukichev[4] using the Usadel equations[6] for the superconducting order parameter. The Usadel equations are valid in the dirty limit (elastic mean free path much smaller than the BCS coherence length) and not subjected to restrictions on temperature range as are the Ginzburg-Landau equations. Different regimes are studied in which the length of the normal region and the barrier transparency is varied.

1.1 Coherence length

The coherence length $\xi_{Sm}(T)$ in a dirty normal material represents the depth Cooper pairs diffuse into the normal material and is expressed as:[4]

$$\xi_{Sm}(T)=\sqrt{\frac{\hbar D}{2\pi kT}} \tag{4.1}$$

For an order of magnitude estimate we substitute the value for the diffusion constant D found by Heslinga *et al.*[7] for $9*10^{19}$ cm^{-3} P doped Si. We obtain a value of: $\xi_{Sm}(1K)\approx 20$ nm which is to be compared with a length between the superconducting electrodes of 80 nm.

1.2 Kupriyanov and Lukichev theory

In the long junction limit ($L>>\xi_{Sm}(T)$ with L the length of the normal link) Kupriyanov and Lukichev[4] find for the critical current:

$$I_c=\frac{64\pi kT}{eR_n}(1+2\Gamma_B)\frac{L}{\xi_{Sm}(T)}C_0^2\exp\left(\frac{-L}{\xi_{Sm}(T)}\right) \tag{4.2a}$$

with C_0 the solution of:

$$\sin\left(\arctan\frac{\Delta}{\pi kT} - 4\arctan C_0\right)=2\gamma_B\sqrt{\frac{T}{T_c}}\sin(2\arctan C_0) \tag{4.2b}$$

with parameter $\gamma_B=\Gamma_B L/\xi_{Sm}(T_c)$ and Γ_B the barrier strength. The normal resistance of the junction $R_n=\rho L(1+2\Gamma_B)/\mathcal{A}$. $\mathcal{A}$ is the area and ρ the resistivity of the normal link. In the limit

of $\gamma_B=0$ and near T_c the results of Kupriyanov and Lukichev[4] are identical to the results calculated by Likharev.[5] For other temperatures small differences appear.

2 Measurement results

2.1 Voltage-carrying state

Current vs. voltage measurements are shown in fig. 4.1 for two devices; one with a low resistance (32f) and one with a high resistance (32d). The two devices clearly show different behaviour. The low resistance device 32f shows a superconducting state near V=0 and a small excess current. The high resistance device 32d shows a large current deficit indicating high interface resistances.

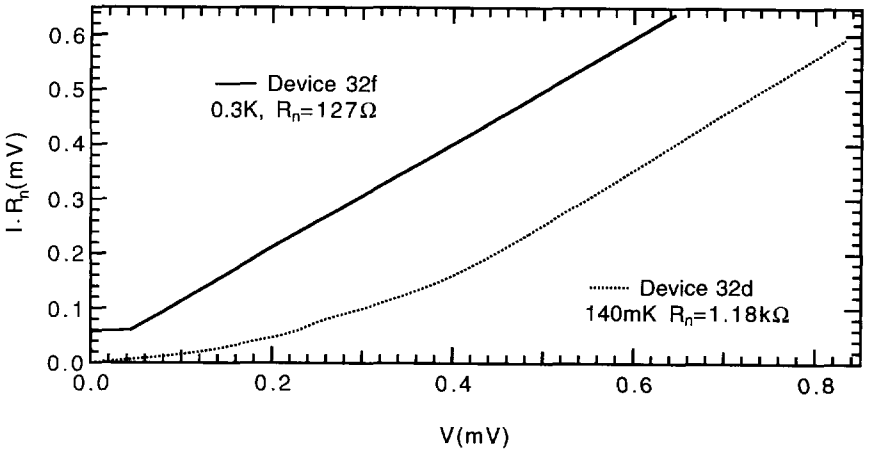

Fig. 4.1 Measured current as function of bias voltage for device 32f (upper curve) and 32d (lower, dashed curve). The graph shows the superconducting state of device 32f near V=0. Note the large current deficit of device 32d.

Figs. 4.2 show the differential resistance measurements vs. voltage. In Fig. 4.2a the behaviour of device 32d is shown. Subharmonic gap structure can be seen, assuming a gap of 0.25 meV it occurs at $2\Delta/2$ and $2\Delta/3$. The shift of the $2\Delta/2$ structure in the 500 mK measurement might be due to heating of the sample which suppresses the gap. The dip in differential resistance near V=0 can be a sign of reflectionless tunneling (see chapter VI).

Fig. 4.2b shows the behaviour of device 32f, the main figure shows the measurements done at higher temperatures and the insert shows the enlarged measurements at the lowest temperatures. At the lowest temperatures (see insert) the differential resistance drops to zero

near V=0 corresponding to the observed supercurrent. Above 600 mK this does not occur. We cannot explain the sharp peak in the differential resistance at small voltage in the 0.5 K curve.

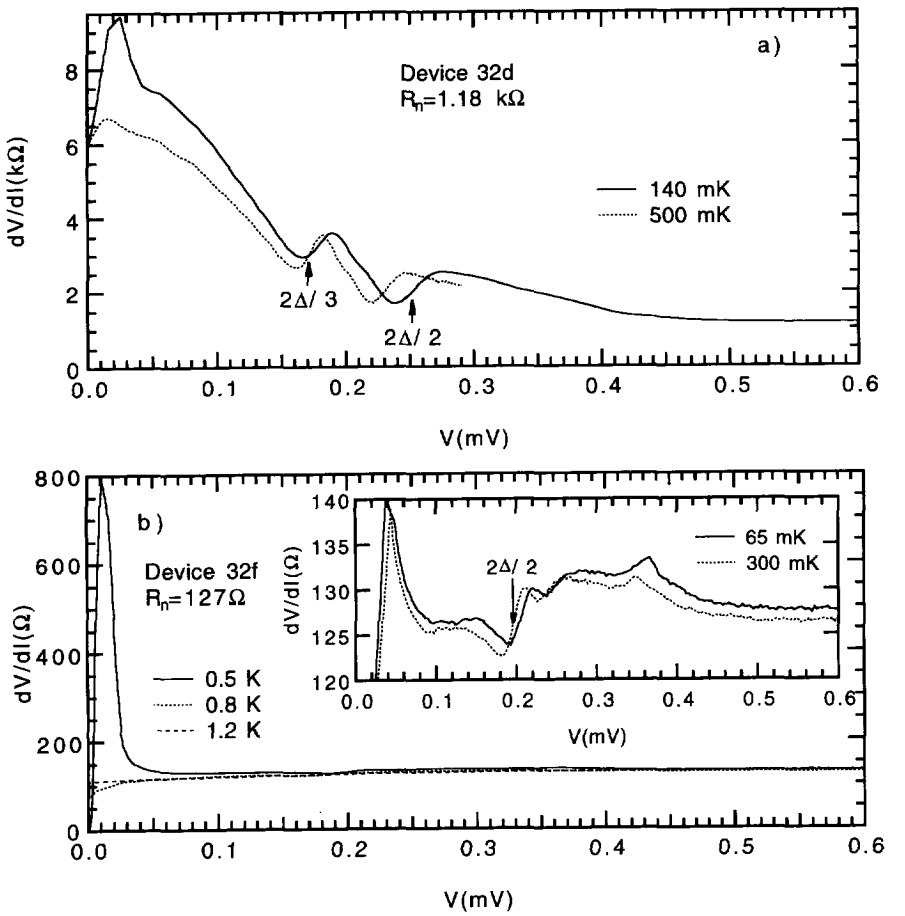

Fig. 4.2 Measured differential resistance as function of bias voltage for the two devices. a) Device 32d. Note the subharmonic gap structure at 2Δ/2 and 2Δ/3, a superconducting gap of 0.25 meV is assumed. b) Device 32f. The insert shows the measurements at the lowest temperatures in detail. The structure at 0.2 mV is identified as subharmonic gap structure at 2Δ/2, the remaining structure can not be connected to subharmonic gap structure.

Device 32f has a low normal state resistance, shows supercurrent at low temperatures (see paragraph 2.2) and weak subharmonic gap structure combined with a small excess current of 80nA. This indicates a device with low interface barriers.

Device 32d has a higher normal state resistance, no supercurrent and clear subharmonic gap structure and a current deficit of 220 nA, all indications of a device with poorly transmissive barriers.

2.1.1 Interpretation

To describe the above observations in terms of the extended OTBK model as presented in chapter III, we first make an estimate of the model parameters P (the transmission probability of the scattering barrier in the normal region), Z (strength of the barrier at the NS Interface) and P_i (inelastic scattering probability).

The transmission probability P was introduced in chapter III paragraph 4.1 and follows from the bulk resistance of the doped silicon and the Sharvin resistance R_o, using Eq. 3.13:

$$R_n=\frac{1+2PZ^2}{P}R_o \qquad (3.13)$$

with Z set equal to zero. The current path through the silicon barrier L is 80±20 nm long and the device has a surface area $\mathcal{A}$ of 0.2 x 20 μm^2. The doping level of the silicon is about 10^{20} cm^{-3} of boron. At these high doping levels the resistivity at low temperature is nearly identical to the resistivity at room temperature.[8] Using the corresponding resistivity $\rho=1.2\cdot10^{-3}$ Ωcm (Sze[9]) we find a normal resistance of the silicon barrier of 2.4 Ω. Comparison with the actual values of more than 100 Ω indicates that the main part of the resistance is caused by the interface. Using the doping level and the free electron model we estimate a Fermi energy E_F of 90 meV, a Fermi velocity v_F of $1.9\cdot10^5$ m/s and a density of states at the Fermi level N(0) of $1.7\cdot10^{27}m^{-3}eV^{-1}$. From this follows that the Sharvin resistance $R_0=[2\mathcal{A}v_Fe^2N(0)]^{-1}$ has a value of 30mΩ. Altogether, this gives a value for the transmission probability of the central barrier in the extended OTBK model P of 0.01.

The barrier strength Z can be estimated from the measured normal resistance of the devices using Eq. 3.13. This gives for device 32d: Z=140 and for device 32f: Z=50. From measurements on the contact resistance we can also estimate Z by using Eq. 3.1. Van den Hove *et al.*[3] measured $1.5\cdot10^{-11}$ Ωm^2 for a contact using the same fabrication process and doping. This gives Z=40. This value is different from the values derived above which is not unusual because contact resistances often show large variation. Contact resistances are very sensitive to the doping near the interface and to processing conditions. For device 32d we expect a high interface barrier strength from the current deficit, 220 nA is near $4\Delta/3eR_n$, the value in the strong barrier limit.[10] For device 32f however, a Z value near unity is expected since this

device shows a small excess current. At this stage we already see that for device 32f the Z values estimated from the resistance and from the I-V curve do not agree. This discrepancy might be explained by an interface that is only partly transparent.

To estimate P_i, the inelastic scattering probability, we first make an estimation of the inelastic mean free path. This length is calculated using the diffusion constant D and the inelastic relaxation time: $l_i=\sqrt{D\tau_E}$. The diffusion constant is derived from the resistivity ρ. From the free electron model we get: $D=(e^2N(E_F)\rho)^{-1}$ and using the resistivity from Sze[9] $\rho=1.2\cdot10^{-3}$ Ωcm we get: $D=3\cdot10^{-4}m^2/s$.

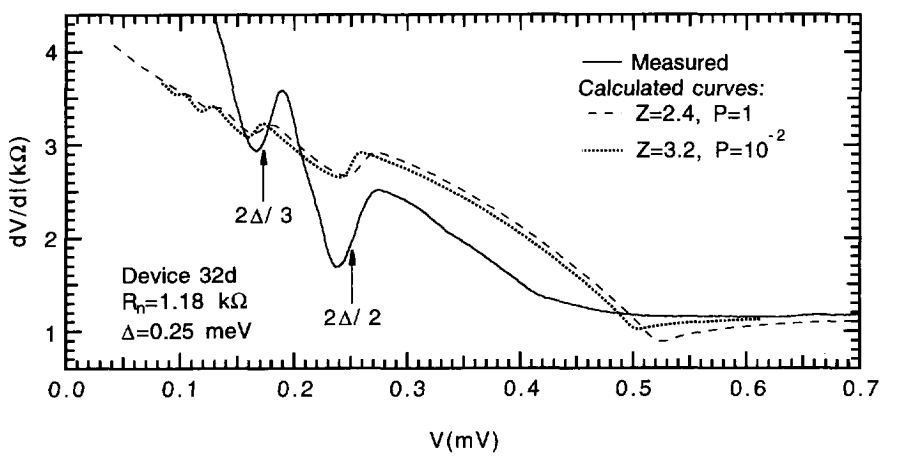

Fig. 4.3 Measured and calculated differential resistance curves as function of bias voltage for device 32d. The measurement is done at 140 mK. The dashed line is calculated using the original OTBK model with Z=2.4. The dotted curve uses the OTBK model extended with elastic scattering with Z=3.2 and P=0.01. In all calculations is assumed: Δ=0.25meV.

In our case carriers with an energy on the order of Δ have to relax to the Fermi energy. In this energy range ($E\approx\Delta$) electron-phonon scattering is of major importance. The relaxation time for electron-phonon scattering can be calculated using a deformation potential approach.[11] In this approach phonons are thought of as waves in an elastic continuum in which the change in energy of the carriers by the strain is given by the deformation potential times the strain. For our case, where $k_BT\ll\Delta$, $eV\ll E_F$, the following expression is obtained[11]:

$$\tau_E^{-1}=3\Lambda^2(m^*)^{5/2}\sqrt{2E_F}/(\pi\hbar^4 d) \qquad (4.3)$$

Here Λ is the deformation potential of silicon ($\approx$3 eV), m^* the effective hole mass (0.43 m_0), and d the density of silicon. This gives: $\tau_E=8\cdot10^{-11}$s; $l_i\approx0.2$ μm, which means $l_i/L\approx3$ from

which we estimate for the inelastic scattering probability P_i a value of the order of one third of the transmission probability.

Calculations using the barrier strength Z of 140 as obtained from the normal resistance gives an unrealistic differential resistance curve that rises to very high values (more than 10 times the normal resistance value) at voltages below twice the gap. In Fig. 4.3 the measured differential resistance curve for device 32d (R_n=1.18 kΩ) is compared with calculations based on the original OTBK model with Z=2.4 (dashed line), and with the OTBK model extended with elastic scattering of the amount calculated above (P=0.01) and Z=3.2 (dotted). Both observations and calculations show subharmonic gap structure near eV=2Δ/2 and eV=2Δ/3.

Clearly, the introduction of elastic scattering does not resolve the discrepancy between the observed and calculated normal resistance. If we use $P=2.5\cdot10^{-5}$ and Z=14 the normal resistance is in reasonable agreement with the observations and the differential resistance curve is nearly identical to the Z=3.2, P=0.01 curve without the slight dip near 0.5 mV. This transmission probability P value however does not agree with the transmission probability calculated from the bulk resistance of the silicon barrier calculated above.

This means that we, like Van Huffelen *et al.*,[2] have to assume an interface that is only partly transparent. These authors assume that the variation in transparency is caused by the distribution of doping atoms near the interface. At places where a doping atom is close to the interface the potential barrier is lower which gives a better transparency. This smaller effective area leads to a larger Sharvin resistance R_0 and to a lower Z value than calculated from the normal resistance and the dimensions of the link (Eq. 3.13). The variation in transparency can also be caused by contamination of the interface.

The incorporation of elastic scattering gives a better agreement of the calculated normal resistance and gives a smaller resistance dip near eV=2Δ (the $P=2.5\cdot10^{-5}$, Z=14 curve does not have a resistance dip near eV=2Δ, in agreement with the observations). The overall structure, especially the rise below eV=Δ, is still not well reproduced. The introduction of a difference in barrier strength between the two sides of the junction can improve the agreement between measurement and calculation as shown by Van Huffelen *et al.*.[2] Here the introduction of a difference in barrier strength Z of almost a factor 2 gives a steeper rise of the differential resistance at voltages below the gap of also a factor 2, while at voltages above the gap the overall shape remains the same. Such a difference in barrier strength is not unlikely as we consider the variation in normal resistance between different devices fabricated in the same batch.

A very low amount of inelastic scattering is sufficient to suppress the subharmonic gap structure. The suppression is already significant for $l_i/L=3\cdot10^4$, corresponding to an inelastic scattering probability P_i which is a fraction of $3\cdot10^{-5}$ of the transmission probability of the central barrier. Calculations with a higher value for P_i gave no structure on the curve at all. The difference with the estimation using Eq. 4.3 ($l_i/L\approx3$) is unrealistically large and indicates that the extension of the OTBK model with inelastic scattering does not give quantitatively useful results. This is probably due to the simplifying assumptions made about the energy relaxation in the model. In our model as presented in chapter III carriers are assumed to relax to the Fermi distribution in one scattering event. In reality relaxation happens in many steps and carriers do not fully relax on such a short distance.

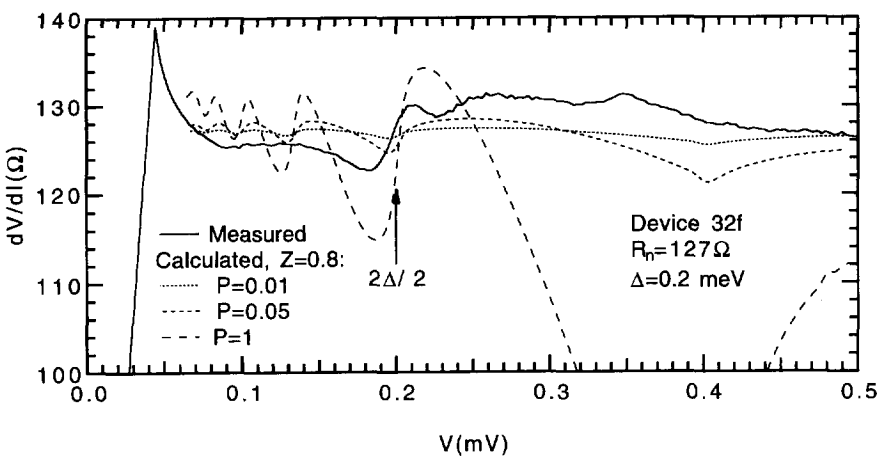

Fig. 4.4 Measured and calculated differential resistance curves as function of bias voltage for device 32f. The measurement was done at 300 mK. Different amounts of elastic scattering are assumed, the P=1 curve uses the OTBK model without extension. In all calculations is used: Z=0.8 and Δ=0.2meV.

In Fig. 4.4 the measured differential resistance curve for device 32f is compared with model calculations. All calculations use Z=0.8, this value does give the best agreement with the data and is consistent with the observed small excess current and the observation of a supercurrent. We have to assume a partly transparent interface to explain the difference between the estimated Z value and the observations. In paragraph 2.2 we will see that a partly transparent interface is also necessary to explain the supercurrent observed in device 32f. The P=1 curve is calculated using the original OTBK model and has a subharmonic gap structure with a much higher amplitude than measured. The P=0.01 curve uses the amount of elastic scattering needed to explain the bulk resistance. This suppresses the subharmonic gap structure too much. In the

P=0.05 curve a smaller amount of elastic scattering is used, here the amplitude of the structure on the curve is comparable with the measurement, but the position of peaks is very different.

The resistance step at about eV=Δ is used to scale the curves, this gives a Δ of about 0.2 meV. Differences in superconducting gap as observed here between the two devices are not unusual. Near the interface the superconductor can very well be slightly degraded compared to the bulk and the gap of the material near the interface is what is observed.

Calculations including the estimated inelastic scattering gave no structure on the curve whatsoever, only when a few orders of magnitude larger inelastic length is assumed, the structure returns.

From this we conclude that I-V characteristics of device 32f can not be described completely in the framework of the OTBK model. Some structure on the differential resistance curve can be understood, some other features remain unexplained.

2.1.2 Conclusion

Device 32d can be described by the OTBK model if only partly transparent interfaces are assumed. The extension with elastic scattering gives a small improvement: the Z value from this model is slightly closer to the estimated one from the contact resistance and the structure near eV=2Δ is somewhat suppressed, as in the observations. With this assumption reasonable agreement in differential resistance can be obtained, if some difference in barrier strength between the two sides is assumed. This is not unrealistic if the spread in normal resistance values between samples of the same batch is taken into account.

The extension with inelastic scattering does not give realistic results. The amount of inelastic scattering needed in the model to get about the right suppression of higher order subharmonic gap structure is unrealistically small (4 orders of magnitude smaller than expected). We conclude that the extension with inelastic scattering to the OTBK model does not give quantitative agreement, which might be due to the simplifying assumptions made about the equilibrium distribution.

Device 32f can not be well described by the OTBK model with or without extensions. The introduction of elastic scattering does give a suppression of the amplitude of the subharmonic gap structure, identical to the observations. Except the subharmonic gap structure near 2Δ/2, there is more structure on the differential resistance curve that can not be described by the OTBK model. This structure could be due to coherent effects, as is the supercurrent.

2.2 Superconducting state

In this paragraph the measurements of the supercurrent will be presented and will be compared with the Kupriyanov and Lukichev[4] model as presented in paragraph 1.

Device 32f shows a supercurrent of which the temperature dependence is shown in Fig. 4.5. No supercurrent is observed at temperatures above 600 mK instead of 1.4K which is the critical temperature of the superconductor. This can be due to the noise level in the instrumental set-up. If the noise energy is larger than the Josephson coupling energy of $\frac{\hbar I_c}{2e}$ observation of the supercurrent is difficult. The thermal noise corresponding to a temperature of 0.7 K is equivalent to a critical current of 30 nA. Some extra noise, transmitted into the cryostat through the measuring wiring for instance, can be sufficient to suppress the expected supercurrent.

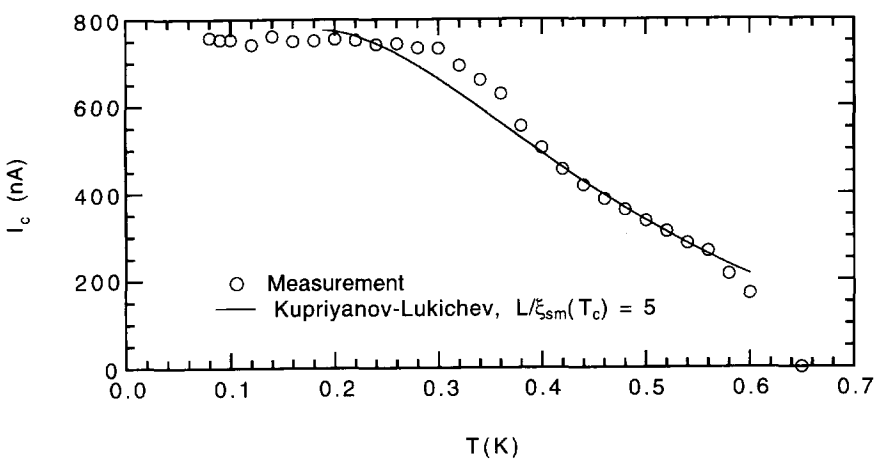

Fig. 4.5 Critical current as function of temperature for device 32f together with calculations using the model of Kupriyanov and Lukichev[4].

To compare the experimental results with the theory of Kupriyanov and Lukichev[4] (Eq. 4.2) we have to estimate the coherence length in the doped silicon $\xi_{Sm}(T)$ (Eq. 4.1) and the barrier strength Γ_B. To determine the coherence length we use the diffusion constant as calculated above: $D=3\cdot10^{-4}m^2/s$. The barrier strength Γ_B is derived using the normal resistance: $R_n=\rho L(1+2\Gamma_B)/\mathcal{A}$ which gives: $\Gamma_B\approx26$. For the area $\mathcal{A}$ we take as above 0.2 x 20 μm^2. With this value and the coherence length we can also calculate the parameter γ_B: $\Gamma_B=\xi_{Sm}(T_c)\gamma_B/L$. This gives: $\gamma_B\approx130$, in this range of $\gamma_B>>\sqrt{T_c/T}$ Eq. 4.2b reduces to:

$$C_0=\frac{1}{4\gamma_B}\frac{\Delta\sqrt{T_c/T}}{\sqrt{(\pi kT)^2+\Delta^2}} \tag{4.4}$$

This gives for the critical current:

$$I_c=\frac{4\pi(1+2\Gamma_B)kT_c}{eR_n\gamma_B^2}\ \frac{\Delta^2}{(\pi kT)^2+\Delta^2}\ \frac{L}{\xi_{Sm}(T)}\exp\left(\frac{-L}{\xi_{Sm}(T)}\right) \tag{4.5}$$

In model calculations we use T_c = 1.4 K. Substituting the values given above results in a critical current of about 10 nA at 200 mK is found, much lower than the measured value.

Another approach would be to use the barrier strength Z as derived in paragraph 2.1. There we use P to make a correction on the bulk resistance using Eq. 3.13, and then we get $\Gamma_B=PZ^2$. This results in a γ_B value much smaller than unity.

Then, a better agreement with the data (full line in Fig. 4.5) in the range 0.2 K - 0.6 K is obtained using $L/\xi_{Sm}(T_c)\approx5$ and $\gamma_B\approx1$ or smaller. In this range the resulting supercurrent is no longer very sensitive to the value of γ_B. Here we can not use Eq. 4.4 but we have to solve Eq. 4.2b. The value $L/\xi_{Sm}(T_c)\approx5$ agrees with the observed junction length of 80 nm and the coherence length calculated using Eq. 4.1. The interface barrier strength is much lower. The barrier strength found gives $\mathcal{A}\approx10^{-14}$ m^2 instead of $4\cdot10^{-13}$ m^2 as designed. This agrees with the calculations for the voltage-carrying state where also a partly transparent interface is assumed to explain the observations.

We conclude that we have observed a supercurrent in a $CoSi_2$-Si-$CoSi_2$ junction. The measured current as function of temperature is compared to the calculations using the theory of Kupriyanov and Lukichev.[4] Agreement between theory and measurement is found if a barrier strength much smaller than expected from the measured normal resistance and the resistivity of the silicon of the barrier is allowed. The calculated coherence length did agree with expectations. The disagreement in barrier strength can be explained by an interface that is only partly transparent. A low barrier strength is consistent with the measurements in the voltage carrying state where also a low barrier strength of Z=0.8 did agree closest to the measurements.

References

1 J. Nitta, H. Nakano, T. Akazaki, and H. Takayanagi, Single-Electron Tunneling and Mesoscopic Devices, Proc. 4th Int. Conf. SQUID '91 (Berlin). Spinger-Verlag Berlin Heidelberg (1992) p.303.

2 W.M. van Huffelen, T.M. Klapwijk, D.R. Heslinga, M.J. de Boer and N. van der Post, Phys. Rev. **B 47**, 5170 (1993).

3 L. van den Hove, R. Wolters, K. Maex, R. de Keersmaeker, and G. Declerck, J. Vac. Sci. Technol. **B 4**, 1358 (1986).

4 M.Yu. Kupriyanov and V.F. Lukichev, Zh. Eksp. Teor. Fiz. **94,** 139 (1988) [Sov. Phys. JETP **67,** 1163 (1988)].

5 K.K. Likharev, Pis'ma Zh. Tekh. Fiz. **2,** 29 (1976) [Sov. Tech. Phys. Lett. **2,** 12 (1976).

6 K.D. Usadel, Phys. Rev. Lett. **25,** 507 (1970).

7 D.R. Heslinga and T.M.Klapwijk, Solid State Comm. **84**, 739 (1992).

8 P. Dai, Y.Zhang, and M.P. Sarachik, Phys. Rev. Lett. **66,** 1914 (1991).

9 S.M. Sze, Physics of Semiconductor Devices, 2nd ed., John Wiley & Sons, New York (1981).

10 K. Flensberg, J.B. Hansen, and M. Octavio, Phys. Rev. **B 38,** 8707 (1988).

11 K. Seeger, Semiconductor Physics, Springer-Verlag, Berlin (1985).

CHAPTER V

MOSFETS WITH SUPERCONDUCTING SOURCE AND DRAIN

In this chapter we report on the electrical behaviour of short channel MOSFETs with superconducting source and drain. We analyse the results and compare those with the different theories described in Chapter III.

Amorphous tungsten (W) is used as superconductor in these MOSFETs, details of the fabrication are described in Chapter II. The conductance is measured at temperatures ranging from 1.2K down to 65 mK in a ^{3}He-^{4}He dilution refrigerator equipped with a superconducting magnet. A standard 4-probe measuring technique is used to diminish the influence of lead resistances. The magnetic field, if applied, is directed perpendicular to the SiO_2/Si interface.

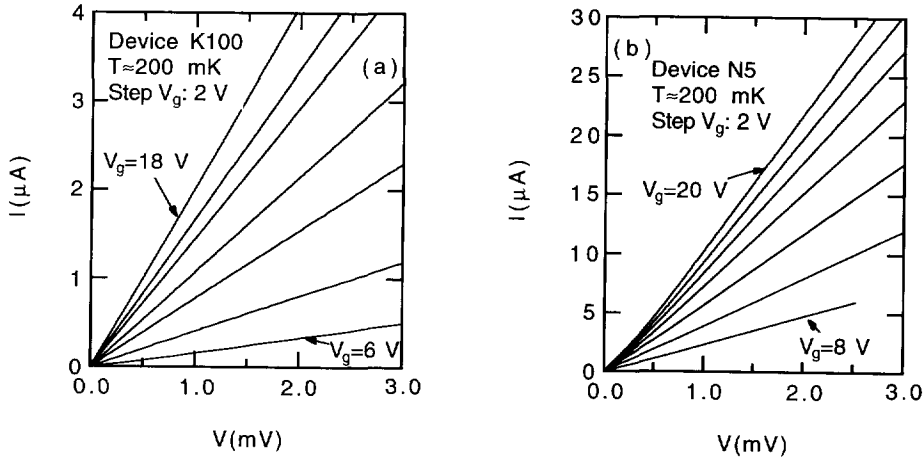

Fig. 5.1 Measured I-V Curves of MOSFETs with superconducting source and drain. a)Device K100, with a gatelength of about 1μm and b) Device N5, with a gatelength below 100 nm. Both devices use amorphous W as superconductor

A typical experimental result is shown in Fig. 5.1 where the current through the devices as a function of source - drain voltage is shown for various values of the gate voltage, i.e. carrier density. A clear increase in conductance is observed for increasing gate voltage, as expected for a field - effect device. Fig. 5.1a shows results for a relatively long device (1μm), whereas Fig. 5.1b shows results for a short device (0.1μm). Note that in the second device the conductance is non-linear approaching an asymptote at high voltage that does not extrapolate to the origin.

In a more detailed analysis we will look at the conductance around V=0. For example in Fig. 5.4b a minimum value of the resistance is observed at V=0, which evolves into a maximum at finite voltage, before gradually the asymptotic value is reached at voltages above twice the superconducting gap. The initial minimum is due to quantum coherent transport and will be discussed in detail in Chapter VI. Here we focus on more mundane aspects that can be understood within the framework of the Boltzmann equation approach outlined in Chapter III. We will first analyse the behaviour in terms of a standard MOSFET model, ignoring the influence of the superconductivity of the source and drain (paragraph 1) to determine the device parameters. Subsequently we will show and analyse the influence of the superconducting state (paragraph 2).

1 Device parameters

1.1 MOSFET model

The device parameters are extracted using a standard MOSFET model.[1] It assumes a resistance R_S in series with a channel at the SiO_2/Si interface. The channel should at low temperatures be considered as a 2-dimensional electron gas (2DEG) with mobility μ. The series resistance R_S represents the resistance between both metal electrodes and silicon together with the resistance of the heavily doped contact layer underneath the metal contacts. These 3-dimensional electronic systems touch the 2DEG on both sides. Note that by describing the resistance as two series resistors we ignore quantum coherent transport. Moreover, the use of this model is justified only for small source - drain voltages, far from saturation, and at gate voltages well above threshold. In this regime the sub-threshold current and short channel effects can be neglected. The total resistance of the device is then given by:

$$R_n = R_S + R_{2DEG} = R_S + \frac{d_{ox}L}{W\mu\varepsilon_{ox}(V_g - V_t)} \qquad (5.1)$$

where V_g is the gate voltage, V_t the threshold voltage, d_{ox}=60 nm the thickness of the gate oxide, μ the mobility of the 2DEG, and ε_{ox}=3.45·10^{-11} C/Vm the dielectric constant of the gate oxide. W is the width and L the length of the channel. The channel length is the lithographically defined gate length minus the length of the two heavily doped regions reaching under the gate (about 60 nm, see Fig. 2.5).[2] The width is 5 μm for both samples. We have studied 8 samples with channel lengths ranging from 0.1 μm and 1 μm. They all show qualitatively similar behaviour. We will focus here on two samples, one with a gate length of 100 nm and one with a gate length of 1 μm for a detailed quantitative analysis.

Fig. 5.2 shows a typical fit of the data (full line) to Eq. 5.1. The data represent the conductance at voltages above twice the superconducting gap, the asymptotic limit, which is believed to be the true normal state resistance as will be explained in paragraph 2. In Table 5.1 the fitting parameters μ, V_t and R_s are listed. The channel length L is estimated by subtracting the depth of the calculated doping profile from the lithographically defined width. The errors indicated in the table for μ, V_t and R_s are twice the standard deviation given by the fitting routine. Most values are reasonable, except for the negative value of R_s for sample K100. In this case the total resistance R_n is an order of magnitude larger than R_s. Hence we attribute the negative value to the inaccuracy.

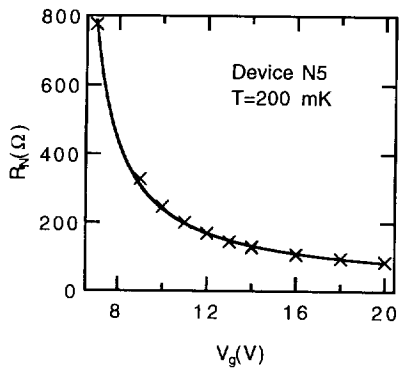

Fig. 5.2 Fit of Eq. 5.1 to the differential resistance at bias voltages above 2 times the gap.

Table 5.1. Characteristic properties of the devices. The mobility μ, threshold voltage V_t and series resistance R_s are results obtained by fitting Eq. 5.1 to the normal state resistance. L is the estimated channel length.

Device:		N5	K100
Gate length	nm	100	1000
L	nm	40±15	940±15
μ	cm^2/Vs	180±70	458±83
V_t	V	5.78±0.15	5.14±0.37
R_s	Ω	18±7	-98±101

1.2 Series resistance

We can compare R_s also with an estimated value using the metal - Si contact resistance and the resistance of the heavily doped silicon. Let us assume a half-infinite contact. Then the current distributes itself exponentially over a characteristic length $\sqrt{R_c/R_\square}$, with R_c the specific metal -

Si contact resistance and $R_\square$ the sheet resistance of the heavily doped contact layer. Then the combined series resistance for two of these contacts equals $R_s=2\sqrt{R_c R_\square}/W$. From the calculated doping profile[2] we estimate $R_\square=175\ \Omega$ and obtain $R_c=1.3\cdot10^{-6}\ \Omega cm^2$ (doping level $2\cdot10^{20}\ cm^{-3}$), using experimental data given by Van der Jeugd *et al.*.[3] This value for the contact resistance may easily be a factor of 2 smaller or larger depending on processing conditions. Using $R_c=1.3\cdot10^{-6}\ \Omega cm^2$ we find R_s which is 60 Ω, higher than the value given in table 5.1 for sample N5. In the following we will use $R_s=18\ \Omega$ as a reasonable value for both samples.

1.3 Mobility

The relatively low mobility and high threshold voltage found in the fit (Table 5.1) indicate[1] a high density of interface charge at the SiO_2/Si interface. A threshold voltage of 5 V corresponds to a negative interface charge of $1.8\cdot10^{12}\ cm^{-2}$, which sets[4] a mobility maximum of about 1000 cm^2/Vs. This interface charge is for example due to the electron trapping during plasma processing. An additional cause for the deterioration of the mobility is the high doping in the channel region resulting from the source and drain contact implantation. For a doping of 10^{18} cm^{-3} (estimated average for device N5, see Fig. 2.5) an additional positive charge of $10^{12}\ cm^{-2}$ resides within 10 nm from the interface. This is consistent with the differences in μ for sample N5 compared to sample K100, which has a lower average doping level resulting from diffusion from the contact areas because of the longer channel.

The uncertainty in the mobility of device N5 is mainly determined by the uncertainty in the determination of the channel length L. The lithographically defined gate length and the length of the heavily doped region reaching under the gate are not accurately known. A lithographic gate length of 100 nm is near the limit of resolution of the SNR resist used in the processing. The actual dimensions depend sensitively on the process conditions, in particular for e-beam writing and resist development. The length of the heavily doped region is derived from doping profile simulations, which are also very sensitive to the process conditions.

1.4 Carrier density and Fermi energy

The gate voltage controls the carrier concentration N_s of the inversion layer through:

$$N_s = \frac{\varepsilon_{ox}(V_g - V_t)}{e d_{ox}} \qquad (5.2)$$

with the symbols having the meaning defined in Eq. 5.1. Using the density of states of the 2DEG[5]: $N'_n=2m^*/\pi\hbar^2$ we find the Fermi energy from: $E'_F=N_s/N'_n$ with m* the effective mass, 0.19 times the free electron mass. To check the 2-dimensional nature of the electron gas the resistance of the device was measured as function of magnetic field. We find weak

Shubnikov-de Haas oscillations (Fig. 5.3), the weakness is caused by the low mobility. Only for the device with the highest mobility, K100, we have been able to get reliable data. From the observed periodicity in 1/B we find for the carrier density: N_s=4.7±0.3 ·10^{12} cm^{-2} to be compared with N_s=3.54±0.2 ·10^{12} cm^{-2} calculated using Eq. 5.2. The slight difference might be due to a thinner gate oxide than designed (≈45 nm), in which case, according Eq. 5.1, also the mobility would be 25% lower.

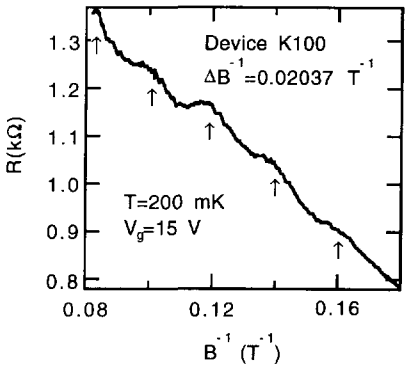

Fig. 5.3 Longitudinal resistance measured as a function of magnetic field for device K100 at V_g=15V. Above H_{c2} of the metallisation weak oscillations are observed from which a carrier concentration of 4.7±0.3·10^{12} cm^{-2} is derived. The arrows indicate the maximums.

2 Influence of the superconducting electrodes

Until now we have focused on the resistance at voltages above twice the superconducting gap, which resistance is taken as a measure of the resistance for a device with normal metal electrodes. As is evident from Fig. 5.1a and 5.1b and more clearly in the differential resistance, changes occur over a range of 0.7 mV. This energy range is what one would expect, although it is somewhat small for a superconductor with a T_c of 3.9 K. In the experiments no supercurrent has been observed. Also sub-harmonic gap structure, changes in resistance at fractional values of the superconducting gap due to multiple Andreev reflections, are not observed. The main aspect, which reflects the superconducting nature of the electrodes is the change over a range of 0.7 mV and the shifted asymptote, i.e. that the extrapolated linear slope intercepts the current axis at a negative value; the current deficit. If all other phenomena can be ignored one expects a peak in resistance around V=0 extending all the way up to the energy gap 2Δ/e followed by a constant value. In a narrow range of voltages around V=0 one finds in some samples a small dip as in Fig. 5.4b. This is the quantum coherent effect mentioned in the introduction and further discussed in Chapter VI. For the present analysis we describe curves

as a broad peak in differential resistance over about $2\Delta/e$ (dashed line in Fig. 5.4b, V_g=10V) followed by a constant value.

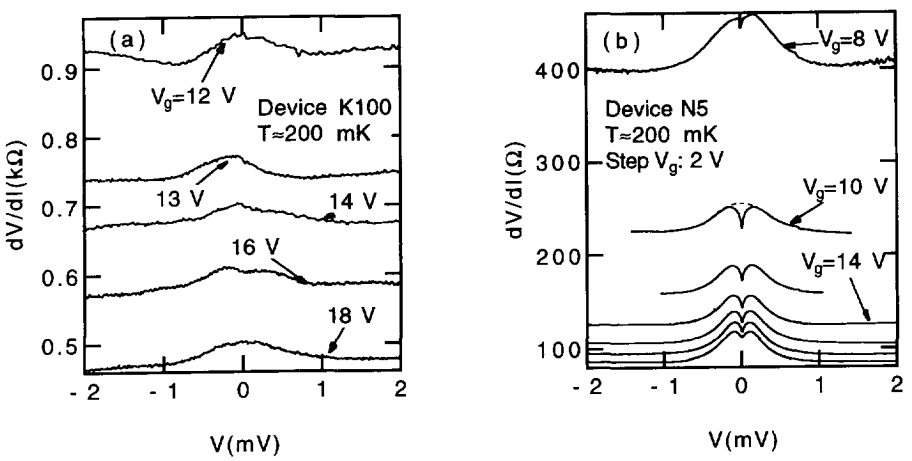

Fig. 5.4 Measured differential resistance as function of bias voltage for different gate voltages. a) Device K100. b) Device N5, the dashed line in the V_g=10V curve illustrates the type of behaviour discussed in this chapter. The dip at V=0 is discussed in chapter VI.

2.1 Interpretation

In Chapter III we have extensively analysed the conceptual framework, relevant to the present data. The absence of sub-harmonic gap structure and/or a supercurrent indicates a weak coupling between the superconducting electrodes. Within the constraints of the SINIS model this points to a high interface resistance diminishing the probability of Andreev reflections. In addition it may indicate that substantial inelastic scattering is present. The barrier strength can be estimated from the normal state series resistance. In table 5.1 we find a series resistance R_s of 18 Ω, the series resistance contains the barriers on both sides. Using Eq. 3.1 and the definition of Sharvin resistance $R_0=[2\mathcal{A}v_F e^2 N_n]^{-1}$, with $v_F=3.6\cdot10^5$ m/s, $N_n=3\cdot10^{21}cm^{-3}eV^{-1}$ and the area $\mathcal{A}=Ws=10^{-13}$ m^2 we find Z=18. Such a large value of Z is equivalent to a transmission probability of 0.003. Alternatively we can also estimate a Z value from the metal - silicon contact resistance. In paragraph 1.2 we find $R_c=1.3\cdot10^{-6}$ Ωcm^2, from this we calculate Z=210. This corresponds to a transmission probability of $2\cdot10^{-5}$.

Clearly we are in the limit of high Z or strong elastic scattering at the interfaces. Hence Andreev reflection can in first order be ignored and we use the low transparency model.

2.1.1 Current deficit

When the I-V curves are extrapolated from voltages above twice the superconducting gap to zero voltage, they intercept the current axis at a negative value. This current-deficit (see chapter III) is caused by the fact that in an energy interval Δ around the Fermi energy of the superconductor, no electrons can be injected from the superconductor into the normal region but can be extracted at the other electrode. This causes a non-equilibrium distribution in the normal region. The current-deficit is a result of the influence of superconducting electrodes on the current through the device.

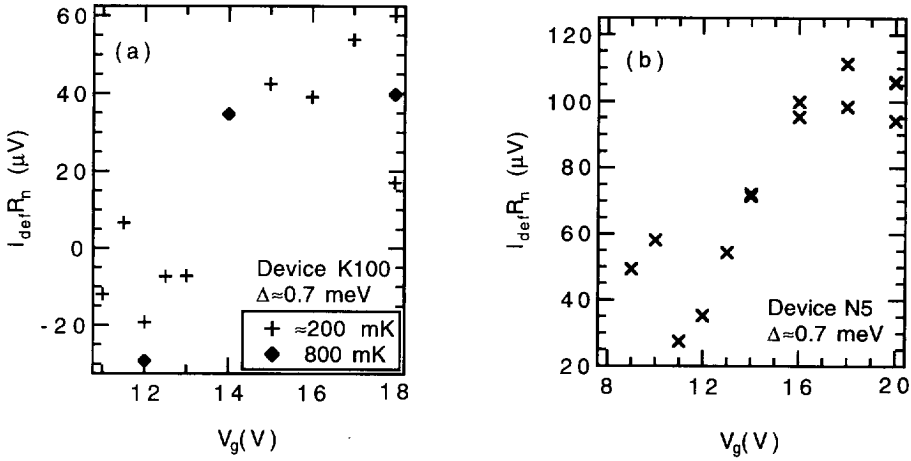

Fig. 5.5 Measured current deficit, multiplied by the normal resistance. a) Device K100 at ≈200 mK (+ symbols) and 800 mK (diamonds). b) Device N5, measured at ≈200 mK.

The current-deficit, multiplied by the normal resistance, is shown in Fig. 5.5. The values at low gate voltages have large uncertainties, as is evident from the differences between the values measured at about the same gate voltage. Particularly for device K100 $I_{def}R_n$ is not significantly different from zero at low gate voltages. The experiments suggest a rising $I_{def}R_n$ with gate voltage beginning at about 12 V. The same trend is visible in Fig. 5.5b for sample N5.

2.1.1.1 Temperature dependence

Measurements for device K100 in Fig. 5.5a do not show significant differences between the 200 and 800 mK measurements. For device N5 all measurements at high bias voltages are done at low temperatures, but in the low bias differential resistance curves (Fig. 6.3) no strong temperature dependence can be seen. The curves only differ near zero bias and are nearly identical at higher bias. From these curves we can estimate the current deficit using:

$$I_{def}R_n=V-I(V>>2\Delta)R_n=\int_0^{V>>2\Delta}\left(1-R_n\frac{dI}{dV}\Big|_v\right)dv. \qquad (5.3)$$

This results in a few percent difference between 1.2 K and 65 mK. We conclude that also for device N5 the current deficit is very weakly temperature dependent.

2.1.1.2 Energy relaxation

In this paragraph we make an order of magnitude estimate of the energy relaxation time and investigate if it is in reasonable agreement with existing theory. In Fig. 5.5 we observe the normalised current $eI_{def}R_n/\Delta$ deficit in the range 0.05 - 0.14. In Fig. 3.9 we see that this value corresponds to a $\Gamma\tau_E$ value of about 0.01. We estimate Γ using the series resistance R_s. We rewrite Eq. 3.21 as:

$$\Gamma=\frac{1}{\mathcal{A}dN_n e^2R_s/2} \qquad (5.4)$$

$\mathcal{A}d$ is the volume of the device which means that $\mathcal{A}dN_n$ is the total number of available states in the device. This number is the sum of available states in the 2DEG and in the heavily doped contact layers. The effective volume of heavily doped silicon per contact we estimate to be $Ws\sqrt{R_c/R_\square}$ with $\sqrt{R_c/R_\square}$ the effective length of current transport as derived in paragraph 1.2. This gives a number of available states in the two contacts of $3\cdot10^{27}$ J^{-1}, compared to which the number of available states in the 2DEG can be neglected. Together with $R_s = 18\ \Omega$ we get $\Gamma\approx10^9$ s^{-1} which results in an energy relaxation time $\tau_E\approx10^{-11}$ s.

Now we investigate if the temperature independent relaxation time is in reasonable agreement with existing theory. In our case electrons with an energy on the order Δ have to relax to the Fermi energy. In this energy range ($E\approx\Delta$) electron-phonon scattering is of major importance. As in chapter IV can we calculate the relaxation time for electron-phonon scattering rate using a deformation potential approach.[6] Here phonons are seen as waves in an elastic continuum in which the change in energy of the carriers by the strain is given by the deformation potential times the strain. For our case where $k_BT<<\Delta$, $eV<<E_F$ the following expression is obtained[6]:

$$\tau_E^{-1}=3\Lambda^2(m^*)^{5/2}\sqrt{2E_F}/(\pi\hbar^4d) \qquad (4.3)$$

Here Λ is the deformation potential of silicon ($\approx$3 eV), m^* the effective electron mass, and d the density of silicon. This gives in our case: $\tau_E=3*10^{-10}$s. This is larger than the value derived from the measurements but not unreasonable because of the uncertainty in the device parameters and the simplifications used in applying the low transparency model. The value obtained using Eq. 4.3 is temperature independent because all parameters are independent of temperature. This agrees with the measurements, in contrast to the phase breaking time derived from weak localisation that is suggested as measure for energy relaxation by Van Huffelen *et al.*[7], Heslinga[8] and Nitta *et al.*.[9] Phase breaking time has a strong temperature dependence, in heavily n-doped silicon Heslinga *et al.*[10] measured $\tau_\phi \approx 9*10^{-10}T^{-2.23}$s.

The difference between energy relaxation in our system and phase breaking scattering, which is an important parameter in weak localisation, is that in our case the electrons have an energy on the order of the superconducting gap ($\approx$1 meV), caused by applied bias, while in weak localisation an order of k_BT ($\approx$0.02 meV at 0.2 K) is assumed. Another difference is that in weak localisation scattering events with a small energy transfer contribute equally to the scattering rate, while in our case these events are unimportant.

2.1.1.3 Gate voltage dependence

The rise of current deficit with gate voltage can be understood if we think of the channel as an extra resistive barrier in the normal region. The strength of the current deficit is determined by the parameter of non-equilibrium $\Gamma\tau_E$, the injection rate times the relaxation time. The injection rate Γ can be seen as the inverse of the mean time carriers are inside the normal region. In this time they have probability to relax to the equilibrium distribution set by the time τ_E. If the reservoir size ($\mathcal{A}dN_n$ in Eq. 5.4) remains the same and the current at a certain bias voltage rises with gate voltage, the mean time carriers are inside the normal region decreases. This gives a higher value for $\Gamma\tau_E$ which gives a higher current deficit.

2.1.2 Gap structure at $2\Delta/e$ or Δ/e

A peculiar feature of the observations is that the gap structure occurs at a bias voltage that is closer to Δ/e($\approx$0.7 meV) than to $2\Delta/e$. The latter is expected from the SINIS models such as the one proposed by OTBK[11] and Heslinga *et al.*.[12] In these models the $2\Delta/e$ - feature appears as a result of energy conservation of particles emitted from one superconductor and absorbed by the other. This is possible when a voltage difference of $2\Delta/e$ allows that carriers enter from filled states below the gap of one superconducting electrode to empty states above the gap of the other superconducting electrode. If there is strong relaxation in the normal region the energy distribution relaxes to a quasi-normal distribution centred around the average potential. A

strong increase in current is possible when the Fermi level of the relaxed electrons passes the gap edge; this also occurs at a voltage of $2\Delta/e$.

In our device relaxation mainly occurs in the heavily doped contact layers. Here a Fermi level close to the potential of the superconducting contacts is expected. When this Fermi level passes the gap edge of the superconducting electrode of the opposite side, a strong increase of current can be expected, occurring at a voltage of Δ/e.

2.2 Conclusion

The superconducting behaviour at bias voltages in the regime between reflection-less tunneling around V=0 and a few times the superconducting gap can be qualitatively described using the low transparency model. Using this model we explain the low current deficit by a high amount of relaxation in the normal region. The absence of subharmonic gap structure is explained by the high interface barriers. This means that the interface barriers are very strong and probably the main obstacle for a supercurrent through the device. To fabricate a MOSFET that carries supercurrent a low contact resistance is essential.

References

1 R.S. Muller and T.I. Kamins, Device Electronics for Integrated Circuits, 2nd Edition, John Wiley & Sons, New York (1986).

2 The 2 dimensional doping profile of the contact implantation is calculated with TMA-TSUPREM-4 Two-Dimensional Process Analysis Program.

3 C.A. van der Jeugd, G.J. Leusink, T.G.M. Oosterlaken, P.F.A. Alkemade, L.K. Nanver, E.J.G. Goudena, G.C.A.M. Janssen, and S. Radelaar, J. Electrochem. Soc. **139,** 3615 (1992).

4 A. Hartstein, T.H. Ning, and A.B. Fowler, Surf. Sci. **58,** 178 (1976).

5 T.Ando, A.B. Fowler, and F. Stern, Rev. Mod. Phys. **54,** 437 (1982).

6 K. Seeger, Semiconductor Physics, Springer-Verlag, Berlin (1985).

7 W.M. van Huffelen, T.M. Klapwijk, D.R. Heslinga, M.J. de Boer and N. van der Post, Phys. Rev. **B 47**, 5170 (1993).

8 D.R. Heslinga, Thesis, University of Groningen, 1991.

9 J. Nitta, H. Nakano, T. Akazaki, and H. Takayanagi, Single-Electron Tunneling and Mesoscopic Devices, Proc. 4th Int. Conf. SQUID '91 (Berlin). Spinger-Verlag Berlin Heidelberg (1992) p.303.

10 D.R. Heslinga and T.M.Klapwijk, Solid State Comm. **84**, 739 (1992).

11 M. Octavio, M. Tinkham, G.E. Blonder, and T.M. Klapwijk, Phys. Rev. **B 27,** 6739 (1983).

12 D.R. Heslinga, W.M. van Huffelen, T.M. Klapwijk, IEEE Trans. Magn. **Mag-27**, 3264 (1991).

CHAPTER VI

OBSERVATION OF CARRIER CONCENTRATION DEPENDENT REFLECTIONLESS TUNNELING IN A SUPERCONDUCTOR - 2DEG - SUPERCONDUCTOR STRUCTURE

1 Introduction

Traditionally, mesoscopic transport phenomena are studied by coupling a short conductor to metallic contacts at different chemical potentials. The consequences of using *superconducting* contacts, are presently largely unexplored. A detailed experimental investigation of many aspects of the conduction mechanism through such contacts is lacking, in particular its energy-dependence and dependence on phase-coherence. In this chapter we focus on a phenomenon first reported by Kastalsky *et al.*.[1] They observed an enhanced conductance around zero-bias at a superconductor-semiconductor junction. This enhanced conductance was found to decrease strongly with bias voltage and applied magnetic field, and quantum-coherent scattering combined with Andreev reflections have been suggested by Van Wees *et al.*[2] as an explanation. In the remaining part of the article we will call this effect reflectionless tunneling (RLT) following a proposal of Marmorkos *et al.*.[3]

1.1 Device description

We have developed a new type of superconductor-semiconductor MOSFET structure (Fig. 6.1), which allows us to study this phenomenon in a well-characterised way. Fabrication of the device is described in more detail in Ref. 4. All previous experiments reported only on magnetic field and temperature dependencies, Refs. 1 and 5 dealt with scattering in 3 dimensions, Ref. 6 reported reflectionless tunneling in a structure with a two-dimensional electron gas (2DEG). The novelty of the present experiment is the use of a 2DEG with a controlled change of the electron density.

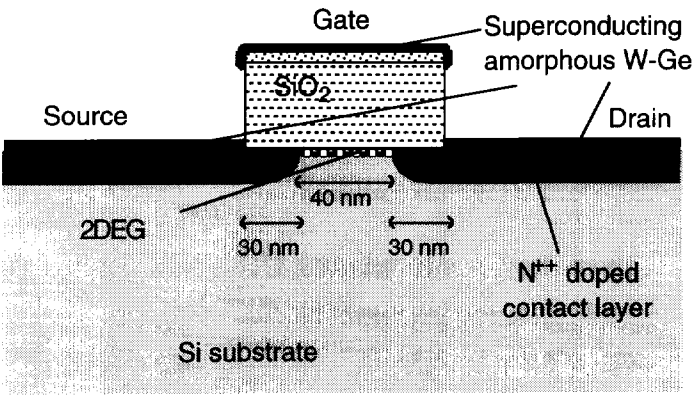

Fig. 6.1 Cross section of the device (schematic).

The device is structured as a short-channel MOSFET with superconducting source and drain contacts. These contacts are made by selective chemical vapour deposition of amorphous W-Ge,[7] which is superconducting with a transition temperature of about 4 K, the precise value depending on the thickness. The material has an upper critical field of about 5 T. The fabrication procedure allows the simultaneous formation of a self-aligned gate with a length of less than 100 nm. We used a strong As-implant (doping at the surface $\approx 2 \cdot 10^{20}$ cm^{-3}) underneath the a-W/Ge superconducting contacts to promote superconductivity in the heavily doped silicon. The conductance of the samples is studied at temperatures below 1 K in a ^{3}He-^{4}He dilution refrigerator equipped with a superconducting magnet. The conductance is measured with standard lock-in techniques and additional care is taken to avoid the influence of external noise sources. The 2-dimensional nature of the electron gas was verified by Shubnikov-de Haas oscillations.

2 Measurements

The measured I-V curves for various carrier concentrations, i.e. gate voltages, are shown in Fig. 6.2. In contrast to Refs. 8 and 9 we did not observe a supercurrent. A gradual decrease of the resistance with increasing gate voltage is clearly visible, demonstrating a proper field effect operation of the device. A change in slope is observed around 0.6 meV, the energy gap value of the superconducting electrode. For voltages above the gap voltage the curve does not extrapolate to the origin but intercepts the current-axis at negative values, a phenomenon known as 'current-deficit'.[10] In Fig. 6.2 (inset) the current deficit is shown as a function of gate voltage. Clearly the amount of current-deficit decreases with decreasing carrier concentration.

Heslinga *et al.*[11] have identified the current-deficit as due to a non-equilibrium distribution of carriers in the normal conductor between the superconducting electrodes. The degree of non-equilibrium depends on the competition between injection rate from the superconducting contact into the normal area and energy relaxation rate in the normal area. The physical origin is the blockage of conducting channels in a band of 2Δ due to the presence of the energy gap in the electrode. If the energy gap is absent these channels do conduct. Heslinga *et al.* assume that the voltage drop is mainly present across the interface. In our case a large part of the voltage drop occurs across the channel. The ratio between the voltage drop across the channel and across the interface increases with decreasing gate voltage. We assume that this phenomenon is the main reason for the decrease of the current deficit with decreasing gate voltage.

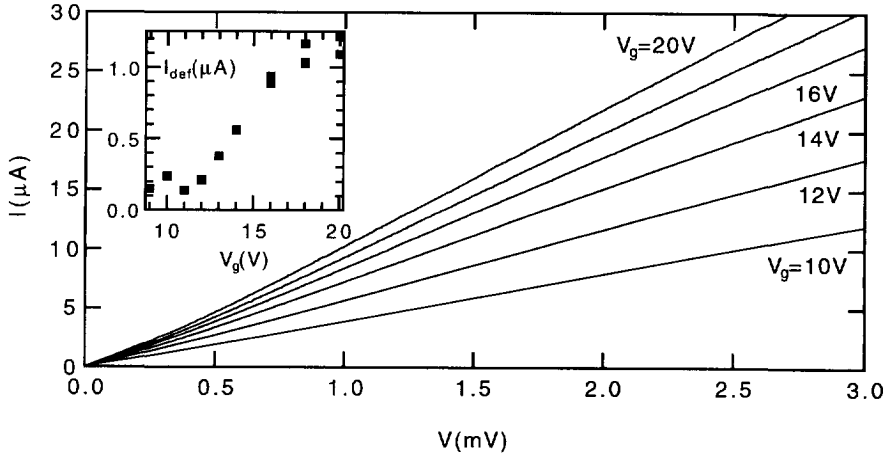

Fig. 6.2. I-V characteristic of the device at different gate voltages at 200 mK. The inset shows the current deficit I_{def} as function of gate voltage V_g.

In the present paper we focus on the differential resistance around V=0. From Fig. 6.2 we expect a broad maximum in resistance extending up to the gap-voltage, where the curve would become flat. As shown in Fig. 6.3 such a broad maximum is indeed found. As the temperature is lowered below 1.2 K a narrow region of reduced resistance (or excess conductance) near zero-bias clearly becomes visible, extending to approximately 0.1 meV. A similar signature has been reported previously for Nb-InGaAs interfaces by Kastalsky *et al.*,[1] Nb-Si interfaces by Magnée *et al.*[5] and in GaAs/AlGaAs-Sn 2DEG structure by Lenssen *et al.*.[6] An explanation based on quantum-coherent enhanced Andreev reflection has been proposed by Van Wees *et al.*,[2] i.e. reflectionless tunneling.[3]

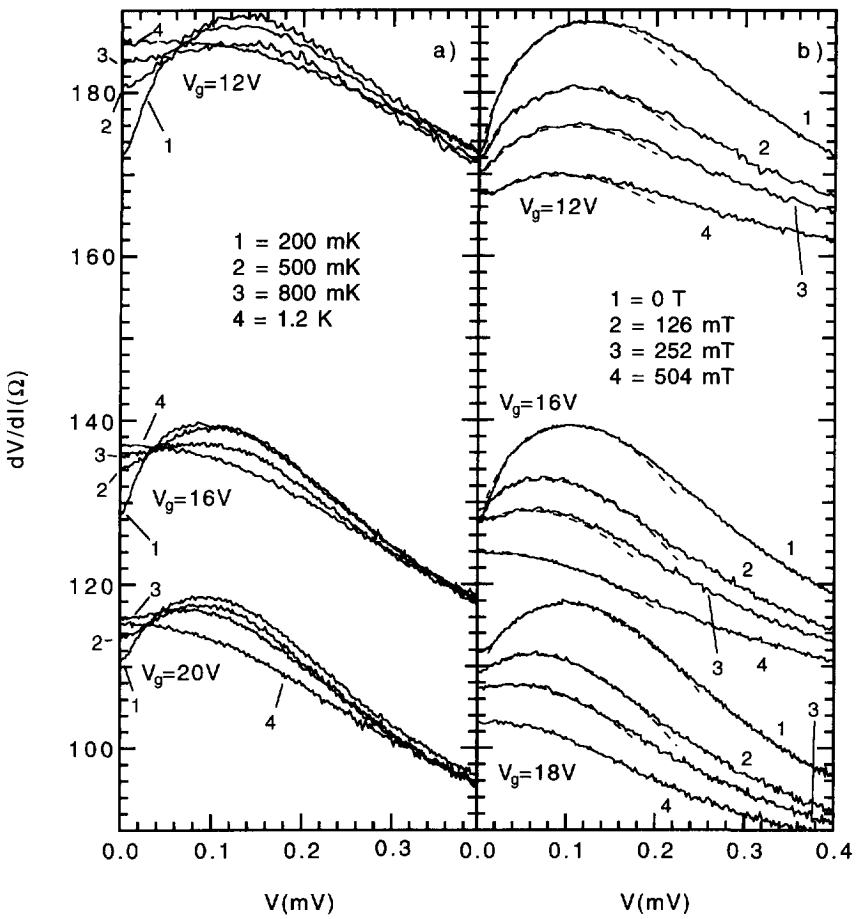

Fig. 6.3. Differential resistance as function of bias voltage at different gate voltages. (a) At different temperatures. (b) At different magnetic fields. The broken lines are fits using expression given by Volkov *et al.* and using a parabolic background.

Fig. 6.3 shows the differential resistance as function of bias voltage for different gate voltages, temperatures (Fig. 6.3a), and magnetic fields (Fig. 6.3b). As usual for MOSFETs, the resistance decreases with increasing electron concentration (gate-voltage). Similarly, the absolute size of the RLT structure decreases. Figure 6.4 shows the differential resistance as a function of voltage bias normalised to the normal state resistance of the device R_N. The inset shows the difference ΔR between the minimum at V=0 and the maximum at finite voltage, as a function of gate voltage. Apparently, the relative resistance change ΔR associated with the RLT is roughly gate voltage independent. In addition, we find from Fig. 6.3 that the temperature at

which the RLT is fully suppressed (defined as the point where the differential resistance no longer decreases near V=0) is not influenced by the carrier-density, whereas the corresponding magnetic field is.

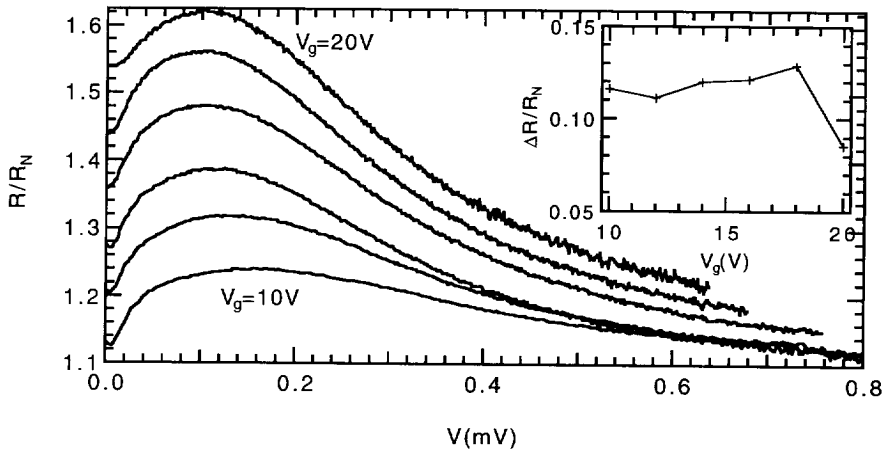

Fig. 6.4. Normalised differential resistance of the device as function of bias voltage at different gate voltages, the upper one at 20 V down in steps of 2 V to the lowest on at 10 V. The curves are results normalised to the resistance of the 2DEG as defined in Eq. 6.1. Inset: Magnitude of the normalised excess conductance as function of gate voltage.

We believe that the conductance peak can be described by a modification due to phase-coherent processes of the Boltzmann-equation approach outlined by Heslinga *et al.*.[10] First however, we need to address a crucial question related to the specific structure of our device. Ideally, the device (Fig. 6.1) should behave as a superconductor-2DEG-superconductor system. The additional complication here is the induced superconductivity within the heavily doped silicon, which causes a further intermediate region between the superconductor and the 2DEG. Moreover, the heavily doped layer extends to a certain depth underneath the gate. Below we therefore first discuss whether the observed RLT is a modification of either the contact- or the channel-resistance alone, or if it is an effect in which the whole structure of the device is of importance.

3 Device characterization

For the extraction of the device parameters the standard small source-drain voltage MOSFET model[11] is fitted to the low temperature differential resistance at voltages well above twice the superconducting gap in which we neglect the proximity effect. In this MOSFET model, a resistance R_S is connected in series with the 2DEG region. This resistance models the contact

resistance between metal and silicon as well as the resistance contribution of the heavily doped contact layer underneath the metal contact. The total resistance of the device is then given by

$$R_N = R_S + R_{2DEG} = R_S + \frac{d_{ox}L}{W\mu\varepsilon_{ox}(V_g - V_t)} \qquad (6.1)$$

where V_g is the gate voltage, V_t the threshold voltage, d_{ox} the thickness of the gate oxide, μ the mobility of the 2DEG, and $\varepsilon_{ox}=3.45\cdot10^{-11}$ C/Vm the dielectric constant of the gate oxide. W is the width and L the length of the channel. The channel length is the gate length ($\approx$100 nm) minus the length of the heavily doped area reaching under the gate (twice about 30 nm).[12]

In our device the different parameters have the following values: d_{ox}=60 nm, L$\approx$40 nm and W=5 µm. A fit to Eq. 6.1 gives R_S=18±7 Ω, V_t=5.78±0.15 V, and μ=180±70 cm^2/Vs. The relatively low mobility and high threshold voltage indicate[11] a high interface charge on the silicon - silicon dioxide interface. Another reason for the low mobility might be the high doping (around 10^{18} cm^{-3}) in the channel. The uncertainty in the mobility originates mainly from uncertainty in the determination of L. We can alternatively estimate R_S from the contact resistance and the resistance of the heavily doped silicon. In this case $R_S=2\sqrt{R_C R_\square}/W$, where R_C is the contact resistance and $R_\square$ the sheet resistance of the heavily doped contact layer. We estimate $R_\square$=175 Ω from the calculated doping profile[12] and obtain $R_C=1.3\cdot10^{-6}$ Ωcm^2 (doping level $2\cdot10^{20}$ cm^{-3}), using data from Van der Jeugd *et al.*.[13] The resulting value R_S=60 Ω is higher than the experimental value of 18 Ω given above, even without taking into account mobility degeneration caused by the perpendicular electric field. The discrepancy between the estimated series resistance and the fitting result might have its cause in the large uncertainties associated with the fit. In addition, the contact resistance is very difficult to measure and very sensitive to doping. For instance, we found that R_C decreased by a factor two if some parameters in the simulation are slightly changed within the error margins of the processing conditions.

In MOSFETs the gate voltage controls the carrier concentration of the inversion layer through $N_S = \varepsilon_{ox}(V_g - V_t)/(ed_{ox})$. Changing the carrier concentration also changes the diffusion constant and the Fermi velocity and the mean free path[14]: $D=\pi N_S\mu\hbar^2/(\nu em^*)$, $v_F=k_F\hbar/m^*=\sqrt{2\pi N_S/\nu}\,\hbar/m^*$, $l=2D/v_F=\sqrt{2\pi N_S/\nu}\,\hbar\mu/e$ where m^* is the effective mass which is 0.19 times the free electron mass and ν the valley degeneracy in the (100) plane which is 2.

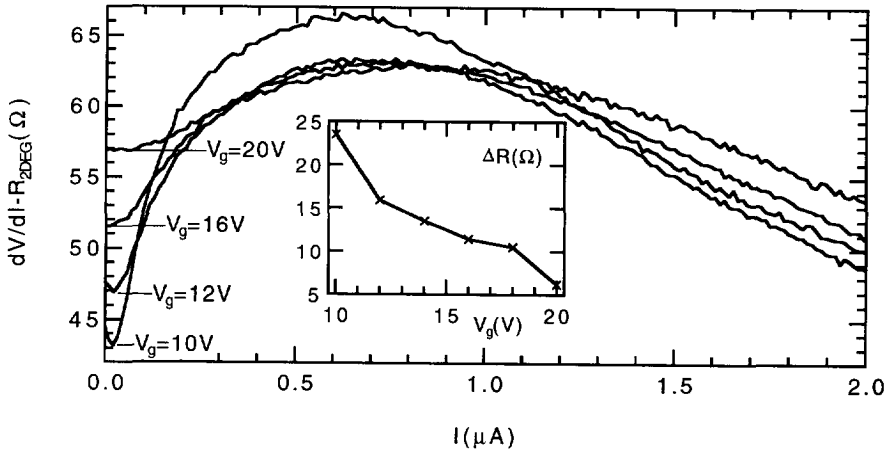

Fig. 6.5. Differential resistance of the device, after subtraction of the resistance of the 2DEG, as function of current at different gate voltages. The dependence of the RLT on gate voltage is clearly visible. Inset: Strength of the RLT (defined as difference between the resistance value at V=0 and at the maximum at finite voltage) as function of gate voltage.

In Fig. 6.5 we have plotted the data of Fig. 6.3 as a function of bias current after subtracting the resistance of the 2DEG (second part of Eq. 6.1). If the observed RLT was caused only by effects occurring at the interface between the superconductor and the heavily doped silicon, i.e. if the 2DEG was just a series resistance, all curves for different gate voltages should fall on top of each other. At higher bias voltages the traces are indeed almost identical. However, although their overall shape is similar it can clearly be seen that a gate voltage increase from 10V to 20V decreases the RLT by a factor three. This demonstrates that the RLT is not caused only by effects occurring at the superconductor - contact layer interface and that the 2DEG clearly plays an important role. This is also supported by the gate voltage independence of the relative strength of the RLT seen in the normalised differential resistance in Fig. 6.4.

We can neglect the influence of the gate on the heavily doped silicon underneath it. The sheet carrier concentration in our device is about a factor of 100 higher in the heavily doped silicon than in the 2DEG, dropping by a factor of 100 over a length scale of about 20 nm. This makes the region where they are comparable exceedingly small (a few nm).

Gao *et al.*[15] measured the phase breaking length in a 2DEG and found l_ϕ=220 nm at 1.76 K and a $T^{-1/2}$ dependence on temperature. Scaling this value for our lower mobility gives about a factor 7 shorter phase breaking length. This means that at 1.2 K the phase breaking length in the 2DEG is about the same as the channel length (≈40nm), but at lower temperatures it exceeds the channel length. In heavily n-doped silicon Heslinga *et al.*[16] measured l_ϕ=408 nm at 1.2 K and a $T^{-1.1}$ power law. The energy-dependent correlation length for superconducting

correlations[17] $\sqrt{\hbar D/E}$ becomes shorter than the channel length only for E > 0.15 meV. Thus for bias voltages below about 0.15 mV and temperatures below 1 K both the correlation length and the phase breaking length exceed the channel length. In Fig. 6.3 these conditions coincide with the onset of RLT.

4 Discussion

We now turn to a discussion of potential mechanisms behind the observed RLT. All the presently available models considered a somewhat idealised device configuration. However, a qualitative comparison with the observations should be possible. A semiclassical picture for the RLT has been proposed by Van Wees *et al.*.[2] In this explanation Andreev reflection and normal reflection on the superconductor - semiconductor interface are assumed as well as elastic scattering in the semiconductor. Excess conductance is caused by constructive quantum interference that results from the phase conjugation between electrons and holes. This phase conjugation originates from Andreev reflection and is destroyed by finite energy, eV or kT, or a magnetic field.

Numerical simulations with a more rigorous treatment of the scattering have been done by Takane *et al.*[18] and Marmorkos *et al.*.[3] Here, as in the model of Van Wees *et al.*,[2] the calculation is done by using a disordered two-dimensional square lattice connected on one side with a superconductor via a potential barrier and on the other side with a perfect-conducting lead. Only small bias voltages are considered ($V \ll \Delta$). Both groups find the RLT, but with a different bias-, magnetic field-, and disorder-dependence than Van Wees *et al.*[2].

Marmorkos *et al.*[3] define a magnetic field B_c at which the excess conductance is reduced by one half. In wide channels ($W > l_\phi > L_N$) they find that B_c is given by $2\Phi_0/l_\phi L_N$ with Φ_0 the magnetic flux quantum and L_N the total length of the normal region. For our device this leads to $B_c \approx 0.3$ T, decreasing with increasing gate voltage, a value reasonably close to the observations and with the correct dependence on gate voltage. The same group also defines V_c, the bias voltage at which the excess conductance is reduced by a factor of two. In Fig. 6.6 we plot quantities characteristic for the RLT as a function of gate voltage. The width of the excess conductance at the base (crosses) decreases with increasing gate voltage. The half-width (the definition used by Marmorkos *et al.*[3]) is roughly constant and increases at high gate voltages (open squares). According to Marmorkos *et al.*[3] V_c should be equal to the Thouless energy ($\pi D\hbar/e(L_N)^2$, with $D=\frac{1}{2}v_F l$). Given the geometry of our device we estimate the Thouless energy about 0.1 meV, which is clearly the right order of magnitude.

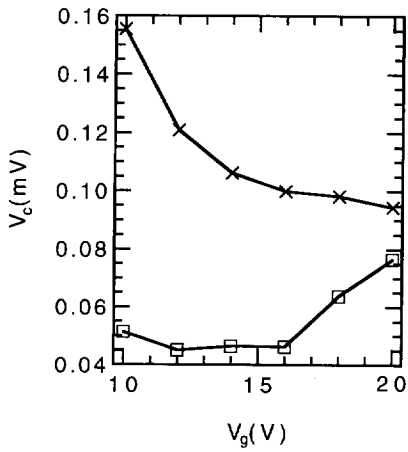

Fig. 6.6. Characteristic size of the RLT as a function of gate voltage. The symbols show both the width of the excess conductance peak at the base (crosses) and the half-width (open squares).

Analytic calculations using Green's function techniques were done by Volkov *et al.*[17] for double barrier structures (a SININ' geometry) with bias voltages in the range from zero to above the gap Δ/e. In these calculations it is assumed that the length of the current path through the normal area L_N is larger than the pair coherence length $\xi_N(\Delta)=\sqrt{\hbar D/\Delta}$. Volkov *et al.*[17] provide an expression for the normalised excess conductance as a function of both voltage and magnetic field:

$$\sigma_d(v)=\left(1+\sqrt{\frac{h^4+v^2}{v_0(h^2+\sqrt{h^4+v^2})}}\right)^{-1} \qquad (6.2)$$

with h the normalised magnetic field $h=2\pi\lambda\xi_N(\Delta)B/\Phi_0$ with λ the London penetration depth and v the voltage eV normalised to the energy gap Δ. In Eq. 6.2 v_0 is a characteristic voltage, which depends on the barrier transmission and normal state conductance of the normal metal N. Here it is used as a free parameter. Superposing a parabolic background on Eq. 6.2 the excess conductance, shown in Fig. 6.3b is very well reproduced, using λ and v_0 as fitting parameters. Excellent fits are obtained with v_0 varying by a factor of ten for different magnetic fields. Strictly speaking if the definition for v_0 of Volkov *et al.*[17] applies, v_0 should be constant. However, our geometry is different from the double barrier tunnel device studied by Volkov *et al.*. A further test is the magnetic field at which the RLT is fully suppressed. For our geometry we estimate a theoretical value in the order of 1 T, decreasing with increasing gate voltage, which is in reasonable agreement with the observations.

5 Conclusion

We have observed a dependence of reflectionless tunneling on the electron density in a 2DEG between superconducting electrodes. The relative strength of the RLT and the temperature at which the RLT is fully suppressed were found to be independent of carrier concentration. On the other hand, our data show that the magnetic field at which the RLT is suppressed does depend on carrier concentration and decreases with increasing carrier concentration. Presently available numerical calculations for several model-geometries with a rigorous treatment of the scattering[3,18] and analytic Green's function approaches[17] provide a good estimate for the characteristic magnetic field.

References

1 A. Kastalsky, A.W. Kleinsasser, L.H. Greene, R. Bhat, F.P. Milliken, and J.P. Harbinson, Phys. Rev. Lett. **67,** 3026 (1991).

2 B.J. van Wees, P. de Vries, P. Magnée, and T.M. Klapwijk, Phys. Rev. Lett. **69,** 510 (1992).

3 I.K. Marmorkos, C.W.J. Beenakker, and R.A. Jalabert, Phys. Rev. **B48**, 2811 (1993).

4 S.J.M. Bakker, B.A.C. Rousseeuw, E. van der Drift, T.M. Klapwijk, and S. Radelaar, Microelectronic Engineering **21,** 435 (1993).

5 P.H.C. Magnée, N. van der Post, B.J. van Wees and T.M. Klapwijk, Physica **B194-196,** 1031 (1994).

6 K.-M.H. Lenssen, L.A. Westerling, P.C.A. Jeekel, C.J.P.M. Harmans, J.E. Mooij, M.R. Leys, W. van der Vleuten, J.H. Wolters, S.P. Beaumont, Physica **B194-196,** 2413 (1994).

7 C.A. van der Jeugd, G.J. Leusink, G.C.A.M. Janssen, and S. Radelaar, Appl. Phys. Lett. **57,** 354 (1990).

8 T. Nishino, M. Hatano, H. Hasegawa, F. Murai, T. Kure, A. Hiraiwa, K. Yagi, and U. Kawabe, IEEE Elec. Dev. Lett. **10,** 61 (1989), M. Hatano, F. Murai, T. Nishino, H. Hasegawa, T. Kure, and U. Kawabe, J. Vac. Sci. Technol. **B7,** 1333 (1989).

9 H. Takayanagi, T. Kawakami, Phys. Rev. Lett. **54,** 2449 (1985).

10 D.R. Heslinga, W.M. van Huffelen, T.M. Klapwijk, IEEE Trans. Magn. **Mag-27,** 3264 (1991).

11 R.S. Muller and T.I. Kamins, Device Electronics for Integrated Circuits, 2nd Edition, John Wiley & Sons, New York (1986).

12 The 2 dimensional doping profile of the contact implantation is calculated with TMA-TSUPREM-4 Two-Dimensional Process Analysis Program.

13 C.A. van der Jeugd, G.J. Leusink, T.G.M. Oosterlaken, P.F.A. Alkemade, L.K. Nanver, E.J.G. Goudena, G.C.A.M. Janssen, and S. Radelaar, J. Electrochem. Soc. **139,** 3615 (1992).

14 T.Ando, A.B. Fowler, and F. Stern, Rev. Mod. Phys. **54,** 437 (1982).

15 J.R. Gao, J.R. Caro, A.H. Verbruggen, S. Radelaar, and J. Middelhoek, Phys. Rev. **B40,** 11676 (1989).

16 D.R. Heslinga and T.M.Klapwijk, Solid State Comm. **84,** 739 (1992).

17 A.F. Volkov, Pis'ma Zh. Eksp. Teor. Fiz. **55,** 713 (1992), JETP Lett. **55,** 746 (1992); A.F. Volkov, and T.M. Klapwijk, Phys. Lett. **A 168,** 217 (1992).

18 Y. Takane and H. Ebisawa, J. Phys. Soc. Jpn. **62,** 1844 (1993).

CHAPTER VII

SUPERCONDUCTIVITY AND LOCALISATION IN THIN POLYCRISTALINE TUNGSTEN-GERMANIUM FILMS

1 Introduction

The coexistence of superconductivity with a normal resistivity two orders of magnitude higher than in ordinary metals has made amorphous metal alloys such as Mo-Ge[1] and Nb-Si[2] model systems for the investigation of electron localization effects. Similar alloys exist also in the case of tungsten alloyed with Si,[3] Ge[4] and Re[5]. These elements have been found to stabilize amorphous thin films and lead to transition temperatures in the range 2 - 5 K, substantially higher than the value of 11mK in crystalline α-W. Using a low temperature chemical vapour deposition (CVD) process we have been able to grow thin, crystalline W-Ge films. These films exhibit high normal-state resistivities of 200μΩcm and transition temperatures, T_c, around 3K, yet are characterized by the ß-W (A15) crystal structure. Here we report on detailed magnetoresistance measurements.

Two competing effects determine the low-temperature resistance of thin, two-dimensional films. Electron localization and electron-electron interaction effects give rise to an increase in resistance. In superconductors, on the other hand, superconducting fluctuations lead to a resistance reduction which can compete with localization effects already at temperatures significantly above T_c. From the temperature and magnetic field dependence of these contributions transport parameters, such as scattering lengths, can be determined. To our knowledge, the first magnetoresistance measurements on W thin films are performed by Rosenbaum *et al.*[6]. Their samples are probably polycrystalline, but with further unspecified structure. Raffy and Laibowitz[5] studied amorphous W-Re alloys. For crystalline ß-W little is known about the low-temperature electronic transport properties besides the superconducting

transition temperature.[7] The crystalline W-Ge films investigated here allow for the first time a direct comparison with the electron-phonon scattering theory for the dirty crystalline limit[8].

2 Theory

For two-dimensional metal films detailed predictions for low temperature quantum contributions to the classical residual resistance are available.[9] Both weak localization and electron-electron interactions give rise to a logarithmic resistance increase as the temperature is reduced. For given temperature there are additional corrections arising from the magnetic field dependence of these quantum corrections. This magnetoresistance we label in the following as $\Delta R/R = [R(T,B) - R(T,0)]/R(T,0)$. Here B is an externally applied perpendicular magnetic field. There are different contributions to the magnetoresistance; here we summarise localization contribution, electron-electron interaction contribution and two superconducting fluctuation contributions, the Maki-Thompson term and the Aslamazov-Larkin term. The sign of the weak localization contribution depends on the strength of spin-orbit scattering characterized by a spin-orbit scattering time τ_{so}, in the limit of small τ_{so} the sign is positive. For materials with high atomic numbers such as W with Z=74 studied here, spin-orbit scattering times approach those of elastic scattering processes (with characteristic time τ) as is expected from the relation[10]

$$\tau/\tau_{so}=(\alpha Z)^4, \tag{7.1}$$

where α is the fine structure constant ($\approx$1/137). This gives in our case a value of about 0.085. In addition to τ_{so} also the inelastic scattering time τ_i and the magnetic impurity scattering time or time of spin relaxation due to spin-spin scattering τ_s determine the magnetoresistance. It is common to write the expression for the magnetoresistance in terms of two effective magnetic fields B_ϕ and B_2 associated with relevant combinations of the scattering rates, namely the phase breaking rate $\tau_\phi^{-1} = \tau_i^{-1} + 2\tau_s^{-1}$ and the rate $\tau_2^{-1} = \tau_i^{-1} + \frac{4}{3}\tau_{so}^{-1} + \frac{2}{3}\tau_s^{-1}$. The corresponding fields B_x (x=ϕ,2) are then given by $B_x = \hbar/(4eD\tau_x)$, where D is the three-dimensional diffusion constant. The weak localization contribution to the two-dimensional magnetoresistance is then written as[11,12,13]:

$$\frac{\Delta R^{loc}}{R} = \frac{3}{2} f_2(B,B_2) - \frac{1}{2} f_2(B,B_\phi), \tag{7.2a}$$

with

$$f_2(B,B_x) = -\frac{e^2R_\square}{2\pi^2\hbar}\left[\Psi\left[\frac{1}{2}+\frac{B_x}{B}\right]-\ln\frac{B_o}{B}\right]. \qquad (7.2b)$$

Here $\Psi(x)$ is the digamma function, $R_\square$ the sheet resistance of the film, $B_o=\hbar/4eD\tau$ the characteristic field corresponding to elastic scattering. For strong spin-orbit scattering, i.e. $B_2/B >> 1$, the B-dependence of the term $f_2(B,B_2)$ in Eq. 7.2 becomes much smaller than that of $f_2(B,B_\phi)$ and the magnetoresistance becomes insensitive to any spin-orbit scattering parameters at the magnetic fields used. In this limit $f_2(B,B_2)$ can be approximated by $^1/_6(B/2B_2)^2 + \ln(B_0/B_2)$.

The diffusion constant is given by $D=v_F^2\tau/3$, where v_F is the Fermi velocity. In the case of superconducting films it can be obtained from the Ginzburg-Landau equations[14]:

$$D^{-1} = \frac{\pi e}{4k_B}\left.\frac{dB_{c2}}{dT}\right|_{T_c}. \qquad (7.3)$$

Eq. 7.3 allows a determination of D directly from the measured temperature dependence of the upper critical field B_{c2} near T_c.

Coulomb interactions between electrons gives rise to a positive magnetoresistance. For sufficiently small perpendicular magnetic fields $g\mu_BB/k_BT << 1$ this contribution[15] is:

$$\frac{\Delta R^C}{R} = \frac{e^2R_\square}{2\pi^2\hbar}(F/2)\ 0.084\ (g\mu_BB/k_BT)^2. \qquad (7.4)$$

Here F is the electron screening constant. For metals F is typically of order one and often treated as an adjustable parameter in the fits.

The contribution of the superconducting fluctuations to the magnetoresistance above T_c are characterized by two parts, the Maki-Thompson term which includes inelastic, Cooper pair breaking processes and the Aslamazov-Larkin term derived from pair fluctuations. For temperatures sufficiently far above T_c such that $2\pi k_B(T-T_c) >> \hbar/\tau_\phi$ and for small applied magnetic fields $B << 2\pi k_B(T-T_c)/4eD$ the Maki-Thompson contribution to the magnetoresistance[11,12,16] is written as:

$$\frac{\Delta R^{MT}}{R} = \frac{e^2 R_\square}{2\pi^2 \hbar} \beta(T/T_c) \left[\Psi \left[\frac{1}{2} + \frac{B_\phi}{B} \right] - \ln \frac{B_\phi}{B} \right], \qquad (7.5)$$

where $\beta(T/T_c)$ is a coefficient tabulated by Larkin[16] and also calculated by Lopes dos Santos and Abrahams[17]. $\beta(x)$ diverges as $\pi^2/[4\ln x]$ when $x \to 1$ and for large x approaches $\pi^2/[6\ln^2 x]$. For fixed temperature, Eq. 7.5 displays the same structure as Eqs. 7.2a,b. The Maki-Thompson term thus contributes in a similar fashion to a positive magnetoresistance as the weak localization term in the strong spin-orbit scattering limit.

Finally, the Aslamazov-Larkin term[18] in the presence of small perpendicular magnetic fields is:

$$\frac{\Delta R^{AL}}{R} = -\frac{\pi^2}{16} \frac{e^2 R_\square}{2\pi^2 \hbar} \frac{1}{[\ln(T/T_c)]^3} \frac{B^2}{(T\, dB_{c2}/dT)^2}. \qquad (7.6)$$

Eq. 7.6 always shows a negative magnetoresistance. However, in moderate fields of up to several Tesla, and typical values of order 1T/K for the upper critical field slope, the Aslamazov-Larkin term is small compared to the Maki-Thompson term except for temperatures very close to T_c.

3 Sample preperation

For sample fabrication a low temperature chemical vapour deposition (CVD) process is employed based on the reduction of WF_6 with GeH_4. Details of the CVD process are reported elsewhere.[4] Substrate temperatures during growth between 300 and 435°C resulted in films with a pure ß-W crystal structure as seen in the X-ray diffraction patterns. The crystalline structure is also revealed by transmission electron microscopy. Rutherford backscattering (RBS) analysis shows a germanium concentration of 16-18% in the films studied. The resistivity of these samples is about 200 μΩcm (Table 7.1).

This high value does not appear to be strongly dependent on the Ge content in the ß-W phase but changes from 190 to 10μΩcm at a deposition temperature of 435°C, above which α-W is deposited. The α-W phase has a Ge concentration of less than 5%. We did not detect any Ge segregation, e.g. at grain boundaries or at the films' surface, at temperatures below 700°C. This indicates that the Ge is uniformly incorporated into the film.

Table 7.1: Relevant parameters for the studied $W_{100-x}Ge_x$ films, T_c and H_c are defined at the mid-point of the resistive transition.

sample	d	$R_\square$	T_c	H_c	D	τ_s^{-1}	A	p
	nm	Ω	K	T	m^2/s	s^{-1}	$s^{-1}K^{-p}$	
$W_{84}Ge_{16}$ (I)	14	135	2.82	6.82	$4.15 \cdot 10^{-5}$	$2.6 \cdot 10^{9}$	$3.17 \cdot 10^{6}$	4
$W_{83}Ge_{17}$ (D)	7.5	290	3.43	7.45	$4.63 \cdot 10^{-5}$	$1.3 \cdot 10^{10}$	$4.92 \cdot 10^{6}$	4
$W_{83}Ge_{17}$ (F) (best fit)	7.5	290	3.39	8.75	$4.63 \cdot 10^{-5}$	$9.9 \cdot 10^{9}$	$13.8 \cdot 10^{7}$	3
						$2.1 \cdot 10^{10}$	$8.80 \cdot 10^{6}$	4
W (Rosenbaum *et al.*)	5	306	2.75	≈5	$6.7 \cdot 10^{-5}$	$\approx 10^{10}$		

We believe that the high resistivity of our films results from compositional disorder in the crystalline structure where all atoms sit on regular A15 places but randomly W atoms are replaced by Ge.

The films are grown on a patterned amorphous silicon layer on an oxidized silicon substrate. The patterning is done by optical lithography. In the CVD process the W is deposited selectively on the amorphous silicon, it only grows on conducting surfaces and not on insulators. Typical film dimensions are 10 μm wide and 1000 μm long. For low temperature electrical transport measurements a standard four terminal configuration is used, the films are mounted in a temperature-controlled helium cryostat. Magnetoresistance data are taken with a Linear Research LR-400 resistance bridge while the magnetic field is swept using a superconducting magnet.

4 Experimental data and fitting results

In the following we discuss results on three different ß-W films (see Table 7.1).Using the measured upper critical field slope, dB_c/dT = 2.37T/K - 2.64T/K near T_c Eq. 7.3 gives the diffusion constant. If we assume $v_F = 1.5 \cdot 10^6$ m/s, which is an average Fermi velocity for metals, this diffusion constant results in an elastic scattering time $\tau = 6 \cdot 10^{-17}$s, corresponding to a mean free path l of about 0.1nm. This value for the Fermi velocity does not take into account the bandstructure of ß-W and the influence of the high Ge content. Since no other data for ß-W are available we assume l = 0.1nm in the following. Eq. 7.1 then leads to spin-orbit parameters $\tau_{so} = 7 \cdot 10^{-16}$s, $l_{so} = (D\tau_{so})^{1/2}$ = 0.2nm and $B_{so} = \hbar/(4el_{so}^2) = 5 \cdot 10^3$T. These values place our films into the strong spin-orbit scattering regime. These values should, however, only be considered rough estimates[6,11,19]. The upper limit for the spin-orbit scattering length can be derived from the fits of the magnetoresistance; although the fits are not very sensitive for the exact value of l_{so}, values larger than 1-2 nm clearly degrade the fits.

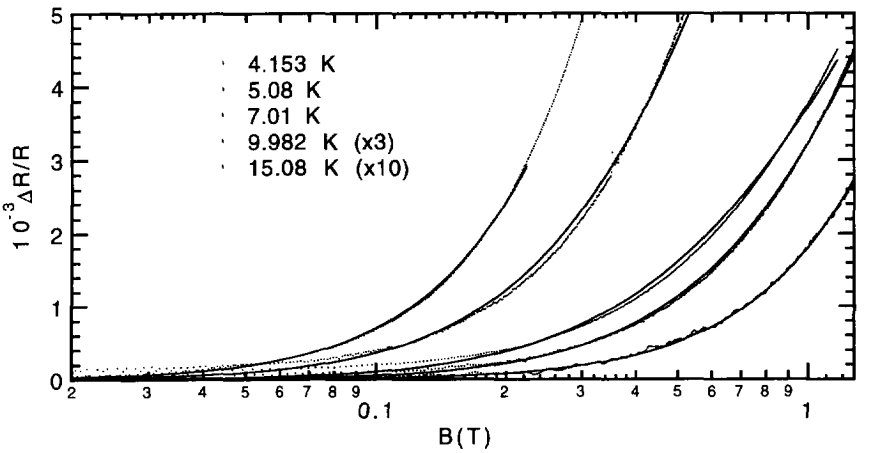

Fig. 7.1: Magnetoresistance curves $\Delta R/R = [R(T,B) - R(T,0)]/R(T,0)$ for sample D, a crystalline, 7.5nm thick $W_{83}Ge_{17}$ film. The solid lines are fits to weak localization and Maki-Thompson contributions (Eqs. 7.2 and 7.5).

The resistance as a function of applied magnetic field for sample F is plotted in Fig. 7.1 for different temperatures. The magnetoresistance is positive at all temperatures which clearly indicates strong spin-orbit scattering. The solid lines are fits of the Maki-Thompson and weak localization functions as described by Eqs. 7.2 and 7.3 to the data using a non-linear least-square fitting procedure. From these fits the inelastic and magnetic scattering times are obtained. All values below $2 \cdot 10^{-14}$s for τ_{so} give equally good fitting results, confirming the idea of a spin-orbit scattering length l_{so} below 1nm. The fits in Fig. 7.1 extend over the range $|B| < k_B(T-T_c)/4eD$. In this range the sample is two dimensional with respect to weak localization, i.e. $d^2 << D\tau_\phi$, $d^2 << \hbar/(4eB)$, and the additional condition, $2\pi k_B(T-T_c) >> \hbar/\tau_\phi$, for the applicability of the Maki-Thompson term are fulfilled. Other contributions like Aslamazov-Larkin fluctuations (Eq. 7.6) and the electron-electron interactions (Eq. 7.4) are neglected over the range of the fits as they are comparatively small.

We note that the fits to Eqs. 7.2 and 7.3 work remarkably well considering that these are results from a perturbation expansion relying on $(k_F l)^{-1} << 1$. In our case we find a product $k_F l = 0.4$ from the diffusion constant using $k_F l = Dm^*/\hbar$, taking the free electron mass for m^*. So the perturbation results might break down. However, in similar systems[1] such as amorphous Mo-Ge with comparable resistivity and Ge content, localization theory successfully describes the data for small $k_F l$.

5 Scattering rate theory

In order to obtain the temperature dependence of the phase breaking rate, it is useful to represent τ_ϕ as a sum of three different contributions, namely electron-electron, electron-phonon and magnetic scattering: $\tau_\phi^{-1} = \tau_{ee}^{-1} + \tau_{ep}^{-1} + 2\tau_s^{-1}$. While magnetic scattering is independent of temperature, in two-dimensional systems in the dirty limit the contribution of electron-electron scattering[20] is proportional to T:

$$\tau_{ee}^{-1} = \left(\frac{e^2 R_\square}{2\pi\hbar^2}\right) k_B T \ln\left[\frac{\pi\hbar}{e^2 R_\square}\right]. \tag{7.7}$$

Eq. 7.7 holds for film thicknesses d such that $d^2 << \hbar D / k_B T << \pi\hbar^2 D / k_B T e^2 R_\square$. For films in the regime $\hbar D / k_B T << d^2 << \pi\hbar^2 D / k_B T e^2 R_\square$ the linear dependence is modified by a logarithmic correction:

$$\tau_{ee}^{-1} = \left(\frac{e^2 R_\square}{2\pi\hbar^2}\right) k_B T \ln\left[\frac{\pi\hbar}{e^2 R_\square} \frac{(\hbar D/k_B T)}{d^2}\right]. \tag{7.8}$$

Electron-phonon scattering leads to a rate τ_{ep}^{-1} proportional to T^p with p between 2 and 4 depending on the ratio $k_B T\, l / \hbar\, c_s$. Here c_s is the velocity of sound and l the electronic mean free path. For the dirty limit in crystalline materials Schmid *et al.*[8] predict for $k_B T\, l / \hbar\, c_s << 1$ that:

$$\tau_{ep}^{-1} = \eta \frac{(\pi k T)^4 l}{\hbar^2 m M c_s^5}, \tag{7.9}$$

where M is the ion mass, m is the electron mass and $\eta = 1/20$ for the transverse case and $\eta = 1/30$ for the longitudinal. Because for longitudinal phonons c_s is usually larger than for transverse phonons, only scattering of electrons with transverse phonons is important.

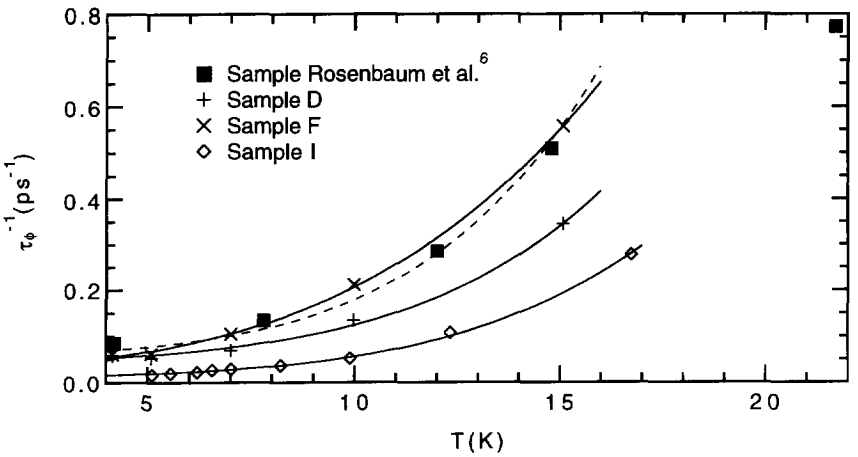

Fig. 7.2: Temperature dependences of the phase breaking rate. The solid lines (————) are the best fits including contributions from magnetic, electron-electron and electron-phonon scattering (Eq. 7.11). For comparison the broken line (– – – – –) is a fit with p=4 to the F sample.

6 Discussion

The phase breaking rate τ_ϕ resulting from the fits is plotted in Fig. 7.2. For our samples the expression for τ_{ee} given in Eq. 7.8 is applicable and the temperature dependence of τ_ϕ is fitted to

$$\tau_\phi^{-1}=2\tau_s^{-1}+5.07\cdot10^6\, R_\square\, T \ln\left(\frac{10^{-7}\, D}{R_\square d^2 T}\right)+AT^p. \qquad (7.10)$$

We find temperature-independent magnetic scattering rates between $\tau_s^{-1} = 0.3\cdot10^{10}s^{-1}$ and $1.3\cdot10^{10}s^{-1}$. A power p=4 for the electron-phonon scattering contribution gives the best fits for two samples, resulting in a coefficient A of $3.17\cdot10^6\ s^{-1}K^{-4}$ and $4.92\cdot10^6\ s^{-1}K^{-4}$. From Eq. 7.9 with a weighted average of the ion masses and l =0.1 nm we obtain $1.3\cdot10^3$m/s and $1.2\cdot10^3$m/s for the transverse speed of sound c_s. These values can be used to calculate an estimate for the Fermi velocity using the Bohm-Staver relation[21] $v_F = c_s\sqrt{3M/Qm}$ where Q is the charge of the ions in units e. The resulting v_F on the order of 10^6 m/s serves as a consistency check for our earlier assumption of an average Fermi velocity, even without taking into account different longitudinal and transverse sound propagation. For film F a power p=3 produces the best fitting results with a coefficient A = $13.8\cdot10^7\ s^{-1}K^{-3}$. Fig. 7.2 compares the p=4 fit with the p=3 fit. In Table 7.1 also the p=4 results are given. The difference between sample D and F is

at present not understood. Using $c_s = 1.2 \cdot 10^3$m/s we find $k_B T\, l / \hbar c_s = 10^{-2}\ T << 1$ over the relevant temperature range. Taking into account that the longitudinal sound propagation speed is usually larger than the transverse we conclude that all films are well within the dirty limit for electron-phonon scattering. Eq. 7.9 may be used and p=4 is the expected exponent.[8]

The temperature dependence with power 3-4 of τ_ϕ^{-1} in our data is in contrast to results on amorphous W-Re alloys. In these materials Raffy and Laibowitz[5] find a linear temperature dependence of τ_ϕ^{-1} which they explain by assuming that τ_ϕ^{-1} is dominated by electron-electron scattering. An alternative explanation could be that in amorphous materials electron-phonon scattering has a different temperature dependence. Also shown in Fig. 7.2 are the data obtained by Rosenbaum *et al.*[6] in granular W films. Their data indeed are of comparable magnitude with ours. Since also the inclusion of oxygen can stabilize the ß-W phase it is conceivable that the films of Rosenbaum *et al.*, fabricated by vacuum arc deposition, contained a significant fraction of oxygen stabilized ß-W grains. Our films, on the other hand, are formed in the presence of a strongly reducing CVD environment and showed no detectable oxygen content. However, it is possible that a thin layer of oxide formed on top of the films after fabrication. Vranken *et al.*[22] shows that such surface layers enhance τ_s^{-1}. Table 7.1 indeed shows a higher τ_s^{-1} for the thinner films.

7 Conclusions

The magnetoresistance data on crystalline W-Ge films can be well understood in terms of weak localization and Maki-Thompson contributions. The calculated phase braking rate can be explained using magnetic scattering, electron-electron scattering and electron-phonon scattering. The electron-phonon scattering follows the theory of Schmid[8] reasonably well. These crystalline films are comparable to amorphous transition metal alloys such as Mo-Ge and Nb-Si, with respect to the high resistivity and the strong spin-orbit scattering. In contrast to amorphous W-Re alloys, however, the temperature dependence of the inelastic scattering rate can certainly not be explained on the basis of electron-electron interactions and significant electron-phonon scattering is found.

References

1 J.M. Graybeal, Physica **135B,** 113 (1985)

2 M. Denhoff and S. Gygax, Phys. Rev. **B 34,** 151 (1986)

3 S.Kondo, J. Mater. Res. **7,** 853 (1992)

4 C.A. van der Jeugd, G.J. Leusink, G.C.A.M. Janssen, and S. Radelaar, Appl. Phys. Lett. **57,** 354 (1990)

5 H. Raffy and R.B. Laibowitz, Phys. Rev **B 30,** 5541 (1984); H. Raffy, R.B. Laibowitz, P. Chaudhari, and S. Maekawa, Phys. Rev. **B 28,** 6607 (1983)

6 R. Rosenbaum, M. Ben-Shlomo, S. Goldsmith, and R.L. Boxman, Phys. Rev. **B 39,** 10009 (1989)

7 W.L. Bond, A.S. Cooper, K. Andres, G.W. Hull, T.H. Geballe, and B.T. Matthias, Phys. Rev. Lett. **15,** 260 (1965); S. Basavaiah and S.R. Pollack, J. Appl. Phys. **39,** 5548 (1968)

8 A. Schmid, Z. Phys. **259,** 421 (1973), B. Keck and A. Schmid, J. Low Temp. Phys. **24,** 611 (1976), A. Schmid, Localization, Interaction and Transport Phenomena, Springer Verlag, Berlin (1985) p.212, S.Chakravarty and A. Schmid, Phys. Rep. **140,** 193 (1986)

9 For a review see: B.L. Al'tshuler, A.G. Aronov, M.E. Gershenson, and Yu.V. Sharvin, Sov. Sci. Rev. A. Phys. **9,** 223 (1987)

10 A. Abrikosov and L.P. Gor'kov, Zh. Eksp. Teor. Fiz. **42,** 1088 (1962) [Sov. Phys.–JETP **15,** 752 (1962)]

11 P. Santhanam, S.Wind,and E. Prober, Phys. Rev. **B 35,** 3188 (1987)

12 G. Bergmann, Phys. Rev. **B 29,** 6114 (1984)

13 G. Bergmann, Phys Rep. **107,** 1 (1984)

14 M. Tinkham, Introduction to Superconductivity, McGraw-Hill, New York (1975)

15 PA. Lee and T.V. Ramakrishnan, Phys. Rev. **B 26,** 4009 (1982)

16 A.I. Larkin, Pis'ma Zh. Eksp. Teor. Fiz. **31,** 239 (1980) [JETP Lett. **31,** 219 (1980)]

17 J.M.B. Lopes dos Santos and E. Abrahams, Phys. Rev. **B 31,** 172 (1985)

18 K.D. Usadel, Z.Phys. **227,** 260 (1969)

19 J. Romijn, R.M.G. Boesten, T.M. Klapwijk, and J.E. Mooij, Springer Proceedings in Physics, Vol. 28, Springer Verlag, Berlin (1987), p. 198

20 B.L. Al'tshuler, A.G. Aronov, and D.E. Khmel'nitskii, J. Phys. **C 15,** 7367 (1982)

21 N.W. Ashcroft and N.D. Mermin, Solid State Physics, Saunders College, Philadelphia (1976); D. Bohm and T. Staver, Phys. Rev. **84,** 836 (1950)

22 J. Vranken, C. Van Haesendonck, and Y. Bruynseraede, Phys. Rev. **B 37,** 8502 (1988)

APPENDIX

RECIPES

1 Lithography

L1: Optical lithography using AZ-resist

1) Dispense HDMS-primer, wetting of the wafer for 10 s and spin at 2000 rpm for 30 s.

2) Put a 12.5% wt. solution of AZ-1470 resist on the wafer, spin 5 s at 500 rpm and then 55 s at 1500 rpm; this gives a layer thickness of about 460 nm.

3) Soft bake at 90°C for 30 min

4) UV exposure for 12 s in the Karl-Süss mask aligning machine.

5) Develop in a solution of AZ developer in water of 1:3 for 60 s.

6) Rinse in DI-water for more than 60 s

7) Post bake at 120°C for 30 min.

L2: E-beam lithography using the AZ-SNR system

1) Dispense HDMS-primer, wetting of the wafer for 10 s and spin at 2000 rpm for 30 s.

2) Put a 12.5% wt. solution of AZ-1470 resist on the wafer, spin 5 s at 500 rpm and then 55 s at 5500 rpm; this gives a layer thickness of about 300 nm.

3) Bake: start at 130°C heat up to 200°C in 20 min, 1 hour at 200°C

4) Put a 1:1 solution of 'SNR-M2 in MIBK' (TOSOH Europe b.v.) in MIBK (Methyl-Iso-Butyl-Keton) on the wafer, spin 5 s 500 rpm and then 55 s 5500 rpm; this gives a layer thickness of about 80 nm

5) Bake at 60°C for 30 min

6) Write the pattern with e-beam, at 50 keV a dose of 80 $\mu C/cm^2$ is sufficient for large areas

7) Develop the resist for 15 s in xyleen, than rinsing for 30 s in IPA(Iso-Propyl-Alkahol). If some residue remains repeat the process only with 3 s in xyleen.

8) Etch through the AZ with O_2 plasma acording to DE5

2 Wet etching

WE1: Resist removal with fuming HNO_3

1) Ultrasonic removal of resist in fuming HNO_3 for 10 min.

2) Rinsing in water for more then 10 min and spin dry.

WE2: SiO_2 etch with HF 1%

1) Etching of native oxide on silicon in a 1% HF solution in water.

Etch rate ≈8.4 nm/min.

2) Rinsing in water for more then 10 min and spin dry.

WE3: Residual Co etch with HCl-H_2O_2

1) Take 3 parts of a 37% HCl solution in water and 1 part of a 30% H_2O_2 solution in water.

2) Add the H_2O_2 slowly to the HCl, be careful that the mixture doesn't boil over.

3) When all the H_2O_2 is added the mixture should have a higher temperature, (60-80°C) now immediately etch the substrate for 10 s.

4) Rinsing in water for more then 10 min and spin dry.

This etching mixture etches also Co_2Si and CoSi.

WE4: RCA-clean

1) NH_4OH-H_2O_2 solution in water, temperature 80 °C, etching for 10 min.

2) Rinsing in water.

3) WE2 for 1 min

4) HCl-H_2O_2 solution in water, temperature 80 °C, etching for 10 min.

5) Rinsing in water.

6) WE2 for 1 min

WE5: SiO_2 etch with BHF 10%

1) Etching of silicondioxide in a 10% HF solution in water, buffered by NH_4F

Etch rate ≈100 nm/min.

2) Rinsing in water for more then 10 min and spin dry.

WE6: Anisotropic Si etch with a KOH Propanol solution in water

1) 150 ml H_2O, 45 gram KOH, 20 ml Propanol-1 at 85 °C,

2) Add another 30 ml Propanol-1

Etch rate ≈ 1 μm/min.

3) Rinsing in water for more then 10 min and spin dry.

3 Dry etching

DE1: SiO_2 etch with CHF_3 plasma

Processing conditions in the Leybold-Heraeus F etcher:

-20 sccm CHF_3

-Total AC power about 100W (= 0.32 W/cm^2)

-Pressure 1.3 Pa

-Bias ≈ -460 V

-Etch rate ≈ 27 nm/min

1) Check the vacuum and the leak tightness.

2) Condition the reactor for about a hour with the processing conditions.

3) Etch until required dept is reached.

DE2: Ar sputter clean before Co deposition

Processing conditions in the Leybold-Heraeus Sputter machine:

-100 sccm Ar

-Pressure ≈3.8 Pa

-Total AC power about 1000W (= 0.35 W/cm^2)

-Bias ≈ -70 V

-Time: 10 min

DE3: Ar sputter etch in F etcher

Processing conditions in the Leybold-Heraeus F etcher:

-20 sccm Ar

-Total AC power about 50W (=0.16 W/cm^2)

-Pressure 1.3 Pa

-Bias ≈ -350 V

-Etch rate ≈ 1 á 1.4 nm/min

-Time: 5 min

DE4: Resist removal with O_2 plasma

Processing conditions in the TEPLA microwave stripper:

-20 % O_2

-50 % Ar

-Pressure 150 Pa

-Total microwave power 615 W

-Frequency 2.45 GHz

-Time 5 - 15 min

DE5: Resist etch with O_2 plasma

Processing conditions in the Leybold-Heraeus F etcher:

-20 sccm O_2

-Total AC power about 30W (= 0.1 W/cm^2)

-Pressure 0.4 Pa

-Bias: -100- -200 V

-Etch rate ≈ 28 nm/min

DE6: Si etch with SF_6-O_2-He plasma

Processing conditions in the Leybold-Heraeus F etcher:

-15 sccm SF_6

-3 sccm O_2

-12 sccm He

-Total AC power about 30W (= 0.1 W/cm^2)

-Pressure 1.3 Pa

-Bias: -40- -80 V

-Etch rate ≈ 120 nm/min

4 Deposition

D1: Co sputter deposition

Processing conditions in the Leybold-Heraeus Sputter machine:

-Background pressure <1e-6 mBar

-15 sccm Ar

-Pressure ≈0.5 Pa

-DC-plasma

-145 Watt (0.35 A, 414 V) -> 5.1 nm Co/min

-Rotate the table at 6 rpm

D2: ß-W CVD deposition

1) Fist cleaning with process WE2 and drying by pulling the wafers slowly out of the vapour of boiling isopropyl alcohol.

2) Then immediately loading into a Varian cold wall W-LPCVD reactor.

Processing conditions:

-Wafer temperature 340 °C

-Pressure 11.5 Pa

-1000 sccm H_2

-10 sccm GeH_4

-10 sccm WF_6

-5 sccm Ar

-This gives about 10 nm/min

-Time 1 min

D3: Amorphous W CVD deposition

1) Fist cleaning with process WE2 and drying by pulling the wafers slowly out of the vapour of boiling isopropyl alcohol.

2) Then immediately loading into the ASM Single Wafer Reactor.

Processing conditions:

-Wafer temperature 275 °C

-Pressure 20 Pa

-200 sccm H_2

-20 sccm GeH_4

-10 sccm WF_6

-This gives about 9 nm/min

-Time 1 min

5 Anneal

A1: RTP anneal for $CoSi_2$ formation

1) Put the wafer in the Rapid Thermal Processor.

2) Let Ar gas flow for over 4 minutes.

3) Heat the RTP to 700°C for 30 s.

4) Let the wafer cool down to below 200°C before removing.

A2: Dry thermal oxidation of Silicon (60 nm)

1) Temperature stabilising at 800 °C for 10 min in a flow of 3 slm N_2 and 0.15 slm O_2

2) Heating from 800 °C to 1000 °C in 20 min in a flow of 3 slm N_2 and 0.15 slm O_2

3) Temperature stabilising at 1000 °C for 15 min in a flow of 3 slm N_2 and 0.15 slm O_2

4) Oxidation at 1000 °C for 1 h 15 min in a flow of 3 slm O_2

5) Anneal at 1000 °C for 20 min in a flow of 3 slm N_2

6) Short oxidation at 1000 °C for 1 min 30 s in a flow of 3 slm O_2

7) Cool down from 1000 °C to 800 °C in 40 min in a flow of 3 slm N_2

A3: Wet thermal oxidation of Silicon (0.5 μm)

1) Temperature stabilising at 800 °C for 10 min in a flow of 3 slm N_2 and 0.15 slm O_2

2) Heating from 800 °C to 1050 °C in 25 min in a flow of 3 slm N_2 and 0.15 slm O_2

3) Temperature stabilising at 1050 °C for 15 min in a flow of 3 slm N_2 and 0.15 slm O_2

4) Purging at 1050 °C for 40 s in a flow of 2.25 slm O_2

5) Oxidation at 1050 °C for 1 h 6 min in a flow of 2.25 slm O_2 and 3.85 slm H_2

6) Purging at 1050 °C for 30 s in a flow of 2.25 slm O_2

7) Anneal at 1050 °C for 15 min in a flow of 3 slm N_2

8) Cool down from 1050 °C to 800 °C in 50 min in a flow of 3 slm N_2

SAMENVATTING

Het proximity effect, de diffusie van Cooper paren vanuit een supergeleider in een normaal materiaal, is reeds lang bekend in dunne, metallische lagen. Bij lage temperaturen strekt dit effect zich uit over afstanden variërend van enkele μm's in goed geleidende metalen tot enkele tientallen nm's in hoog gedoteerde halfgeleiders. Nu fabricage van devices van 100nm en kleiner mogelijk is geworden, is dit effect te gebruiken voor de realisatie van een Supergeleidende Field Effect Transistor; een SFET. Dit onderzoek is oorspronkelijk gestart als samenwerking met Dr. U. Kawabe van Hitachi Central Research Laboratory in Japan. Hij was geïntereseerd in het gebruik van geavanceerde microfabricage technieken voor het maken van een SFET. In een SFET worden twee supergeleiders door middel van het proximity effect gekoppeld en wordt de koppeling door een electrische spanning op een gate electrode beïnvloed. In dit proefschrift worden diversen van dergelijke structuren bestudeerd, alle gebruik makend van silicium als halfgeleidende koppeling. Twee typen devices worden besproken met verschillende supergeleiders: $CoSi_2$ en amorf wolfram. Er is gekozen voor deze supergeleiders omdat deze zelf-uitlijnend gedeponeerd kunnen worden zodat de fabricage eenvoudiger is. De doelstelling van dit onderzoek is om meer inzicht te krijgen in het stroomtransport in dit soort strukturen en de mogelijkheden om ze te fabriceren.

In hoofdstuk II wordt de fabricage beschreven. Alle devices hebben een MOSFET (Metal-Oxide-Semiconductor FET) struktuur met silicium als basis materiaal. Supergeleidende source en drain metallisaties worden gescheiden door een gate boven een 2-dimensionaal electron gas (2DEG). Dit 2DEG koppelt de twee supergeleiders, de ladingdragers concentratie wordt bepaald door middel van een spanning op de gate. De verbinding tussen het 2DEG en de supergeleidende electrodes wordt verzorgd door een hoog gedoteerde laag, vlak onder de supergeleidende elektrodes. Ook worden devices beschreven waar source en drain rechtstreeks gekoppeld worden door hoog gedoteerde materiaal.

De devices zijn gemaakt met behulp van elektronenlithografie, anisotroop reactief ionenetsen (RIE) en zelf-uitlijnende metallisatie en contact-implantatie. Elektronenlithografie is noodzakelijk om de vereiste afmetingen van de gate in de orde van 100 nm te krijgen. Optische lithografie wordt gebruikt bij fabricagestappen die minder hoge eisen stellen aan de resolutie.

Zelf-uitlijnende implantatie en metallisatie zijn gebruikt om met slechts één lithografische stap met hoge resolutie te kunnen volstaan. Dit is van belang omdat het uitlijnen van twee hoge-resolutiestappen t.o.v. elkaar moeilijk is en waarbij mogelijk veel van de bereikte resolutie weer verloren gaat. Zelf-uitlijnende contact-implantatie betekent dat de reeds gedefinieerde gatestructuur als masker dient voor de implantatie. Zelf-uitlijnende metallisatie wordt in dit proefschrift op twee manieren bereikt, afhankelijk van de gebruikte supergeleider. Amorf wolfram ($T_c \approx 4K$) kan selectief gedeponeerd worden in een LPCVD proces op silicium en niet op SiO_2. $CoSi_2$ ($T_c \approx 1.4K$) wordt selectief gevormd door middel van het verhitten van een gesputterde laag kobalt op silicium. Dan reageert het kobalt met silicium op plaatsen waar deze in contact zijn en niet waar kobalt in contact is met het SiO_2.

In hoofdstuk III worden modellen voor de stroom door deze devices gepresenteerd. Hier worden verschijnselen behandeld waarbij het golfkarakter van de elektronen verwaarloosd kan worden, dit is het geval bij hogere spanningen.

Voor het inzicht in het stroomtransport is het van belang onderscheid te maken tussen verschijnselen die samenhangen met het golfkarakter van de elektronen en verschijnselen waarbij het golfkarakter verwaarloosd kan worden. Verschijnselen die samenhangen met het golfkarakter van de elektronen treden over het algemeen op bij lage spanningen; onder andere superstroom en reflectieloos tunnelen.

Een belangrijk verschijnsel dat optreedt aan supergeleider - normaal contacten is Andreev reflectie: een electron komend uit het normale materiaal gaat in de supergeleider verder als een Cooper paar terwijl een gat terug het normale materiaal in gaat. In dit hoofdstuk worden bestaande modellen besproken en worden uitbreidingen met elastische en inelastische verstrooiing in het normale gebied gepresenteerd. Ook wordt gekeken naar de mogelijkheid de bestaande één-dimensionale modellen uit te breiden naar meer dimensies.

In hoofdstuk IV worden meetresulaten met interpretaties gepresenteerd van devices waarbij $CoSi_2$ is gebruikt als supergeleider. Deze devices hebben geen gate en vertonen superstroom. Deze superstroom kan alleen goed verklaard worden met bestaande modellen als aangenomen wordt dat het contactvlak slechts gedeeltelijk transparant is. Ook voor de niet supergeleidende toestand blijkt het noodzakelijk een gedeeltelijk transparant contactvlak te veronderstellen. De uitbreiding van de bestaande modellen zoals gepresenteerd in hoofdstuk III levert nauwelijks verbetering op.

In hoofdstuk V en VI worden meetresulaten met interpretaties gepresenteerd van devices waarbij amorf wolfram is gebruikt als supergeleider. Deze devices hebben wel een gate en

vertonen geen superstroom. In hoofdstuk V wordt het gedrag bij hogere spanning over het device besproken. Uit de meetresultaten blijkt dat het contactvlak een hoge weerstand heeft waardoor er geen superstroom optreedt en Andreev reflectie onderdrukt wordt.

In hoofdstuk VI wordt het gedrag besproken bij lage spanning over het device waarbij amorf wolfram is gebruikt als supergeleider. Bij lage spanning over het device wordt toegenomen geleiding waargenomen die afhankelijk is van de electronen dichtheid in het 2DEG. Dit effect wordt reflectieloos tunnelen genoemd, en wordt veroorzaakt door toegenomen Andreev reflectie door constructieve interferentie met gereflecteerde deeltjes. De metingen worden vergeleken met bestaande modellen die goede voorspellingen doen voor het karakteristieke magnetische veld waarbij het effect onderdrukt wordt.

In hoofdstuk VII worden magneto-weerstandsmetingen gepresenteerd aan polykristallijne WGe films met 16-18% Ge, die een hoge specifieke weerstand hebben ($\approx$200 $\mu\Omega$cm) en supergeleidend worden. Deze metingen geven de mogelijkheid voorspellingen te testen betreffende elektron-phonon verstrooiing in aanwezigheid van sterke elastische verstrooiing. Ook deze films zijn gedeponeerd met een LPCVD proces, hebben de ß-W structuur (A15) met een kritische temperatuur T_c van ongeveer 3K en een kritisch veld H_{c2} in de buurt van 8T. Bijdragen van de supergeleidende fluctuaties en zwakke lokalisatie tot de magneto-weerstand worden besproken. Geconstateerd wordt dat de inelastische verstrooiingsfrequentie bepaald wordt door elektron-phonon verstrooiing.

NAWOORD

Wanneer ik terugdenk aan mijn vijf jaar bij DIMES zie ik dat er velen hebben bijgedragen aan mijn onderzoek. Zonder al deze steun zou ik niet zover zijn gekomen.

In de eerste plaats bedank ik mijn promotoren Teun Klapwijk en Sieb Radelaar. Zij hebben dit onderzoek mogelijk gemaakt en mij wetenschappelijk en organisatorisch de weg gewezen. Verder waren de discussies met mijn directe begeleider Emile van der Drift zeer belangrijk en hebben zijn stimulans en kritiek mij veel geholpen. Aan de wetenschappelijke begeleiding hebben Heinrich Jäger en Ad Verbruggen ook in belangrijke mate bijgedragen. Gesprekken met de overige wetenschappers binnen DIMES/S zijn eveneens erg nuttig geweest. Van de studenten wil ik vooral Geert Hilbandie noemen wiens werk aan de CoSi2 samples onmisbaar was voor hoofdstuk vier. Veel technici bij de afdeling Technische Natuurkunde en bij DIMES hebben mij de onontbeerlijke technische ondersteuning gegeven. Als eerste bedank ik hiervoor Bernard Rousseeuw die vele weken voor mijn onderzoek bezig is geweest. De andere technici, Tony, Gilles, Jack, Bert, Alfred, Frans, Joop, Wim, Willem, Bram, Jan, Ben en vele anderen, allemaal bedankt! Mijn collega promovendi bedank ik voor de stimulerende discussies en andere ondersteuning. Dick, Wim, Peter, Kars-Michiel, Jianrong, Philip, Carolien, Albert, Hans, Gert, Kees, Ed, Rik, Marian, Arjan, Pieter, Rijko, Dov, Jan-Willem, Arnoud, Jeroen en wie ik nog vergeet, bedankt. Tevens bedank ik alle anderen, binnen en buiten de T.U. Delft, die ook op enigerlei wijze hebben bijgedragen aan de totstandkoming van dit proefschrift.

Nogmaals, iedereen van harte bedankt en tot ziens.

Delft, september 1994 Bas

CURRICULUM VITEA

Bas Bakker

4 September 1964	Born at Purmerend, The Netherlands
Sept. 1976 - June 1982	Atheneum at St. Ignatius College in Purmerend.
Sept. 1982 - Sept. 1987	Applied Physics - T.U. Delft. Graduation project done in the low temperature group from Prof. dr. H. Postma on the subject of specific heat measurements at very low temperatures.
Nov. 1987 - Apr. 1989	Detached by the Airforce to the TNO Physics and Electronics Laboratory in the Hague.
Apr. 1989 - Feb. 1994	Ph.D. research at Delft Institute of Microelectronics and Submicron Technology (DIMES), this thesis.
Feb. 1994.- Present	Sales Engineer at RAM Mobile Data, Maarssen.

Publications

R.W. Willekers, W.A. Bosch, H.C. Meijer, S.J.M. Bakker, H. Postma, and J. Flokstra: "The Specific Heat of $Er_xY_{1-x}Rh_{1.1}Sn_{3.6}$ for x=0.4, 0.8 and 1". Proc. 18th int. conf. on Low Temperature Physics, Kyoto, 1987. Jap. J. Appl. Phys. **26,** 1291 (1987) Suppl. 26-3.

A.N. de Jong and S.J.M. Bakker: "Fast and objective minimum resolvable temperature difference measurements". SPIE Vol. **916** (1988).

D.R. Heslinga, W.M. van Huffelen, T.M. Klapwijk, S.J.M. Bakker, and E.W.J.M. van der Drift: "Electronic transport across niobium-silicon interfaces". Cryogenics **30,** 1009 (1990).

S.J.M. Bakker, E. van der Drift, D.R. Heslinga, T.M. Klapwijk, and H.M. Jäger: "Electron Transport In $CoSi_2$-Si-$CoSi_2$ Structures". Single-Electron Tunneling and Mesoscopic Devices, Proc. 4th Int. Conf. SQUID '91 (Berlin). Spinger-Verlag Berlin Heidelberg (1992) p.303.

S.J.M. Bakker, B.A.C. Rousseeuw, E. van der Drift, T.M. Klapwijk, and S. Radelaar: "Fabrication of Si-coupled three terminal superconducting device using selective deposition of ß-W". Microelectronic Engineering **21,** 435 (1993).

S.J.M. Bakker, H.M. Jaeger, T.M. Klapwijk, E. van der Drift, and S. Radelaar: "Superconductivity and localization in thin polycrystalline tungsten-germanium films". Phys. Rev. **B48,** 4168 (1993).

T.G.M. Oosterlaken, G.J. Leusink, G.J. Kuiper, S.J.M. Bakker, A.H. Verbruggen, H.M. Jaeger, G.C.A.M. Janssen, S. Radelaar, "Resistivity and superconducting transition temperature of very thin amorphous tungsten-germanium films deposited by Chemical Vapour Deposition". Physica **C 214,** 359 (1993).

G.R. Hilbrandie, S.J.M. Bakker, E. van der Drift, B.A.C. Rousseeuw, T.M. Klapwijk, and S. Radelaar: "Mesoscopic silicon coupled superconducting junctions of $CoSi_2$ formed in a self-aligned process". Microelectronic Engineering **23,** 445 (1994).

S.J.M. Bakker, E. van der Drift, T.M. Klapwijk, H.M. Jaeger, and S. Radelaar: "Observation of carrier concentration dependent excess conductance in Superconductor - 2DEG - Superconductor structure". Phys. Rev. **B49,** 13275 (1994).